OPTICAL MULTISTABILITY IN HIGH-Q NONLINEAR PHOTONIC CRYSTAL NANORESONATORS

Karindra Liem Perrier

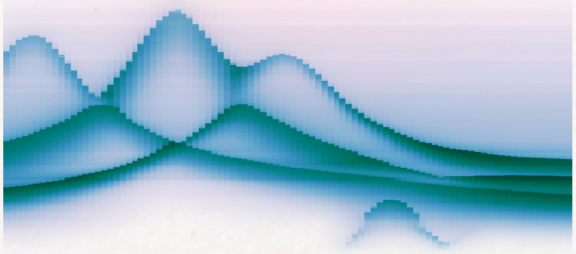

Optical Multistability in High-Q Nonlinear Photonic Crystal Nanoresonators

Karindra Liem Perrier

2023

Cover: The cover shows what we call a *mode map* of one of the photonic crystals we use for the research described in this thesis. The measurement technique is explained in Chapter 3, Section 3.2. In short, infrared laser light is sent through the photonic crystal while at the same time we spatially scan the surface of the photonic crystal with a second laser, a blue light beam that locally heats up the material. What you see in the picture is the optical response of the photonic crystal to this scan for a range of infrared wavelengths (scan position on the horizontal axis, input wavelength on the vertical axis). It reveals the shape of the optical modes that are present in the photonic crystal, in other words, the amplitude of the electromagnetic field anywhere along the scan. Looking at the resulting image we see three mountain-like peaks crossing each other and a fourth small peak at the bottom right. These are the shapes of four resonators, each with their own resonance wavelength, and their own interaction (coupling) with the others.
The back cover depicts another mode map. This one was taken from a waveguide that was not suitable for the experimental goals we had. Still, I believe it is a beautiful measurement to look at. We observe two resonators. One sharp resonance with a high quality factor. One broader resonance (the one with the soft haze), with more losses to its surroundings and thus larger linewidth. The two are coupled (from their behavior you can tell they clearly 'feel' each other), but the lossy mode would have needed too much input light for it to exhibit nonlinear behavior, a quality we wanted to study in this PhD project. The white speckles you see are the result of the logarithmic scale chosen for the colormap. Whenever the photodiode measures *zero* the log will return $-\infty$: a bright empty datapoint on the mode map.

Nanophotonics
Debye Institute for Nanomaterials Science
Departement Natuur- en Sterrenkunde
Faculteit Bètawetenschappen
Universiteit Utrecht

Printed by Gildeprint
DOI 10.33540/1751

Optical Multistability in High-Q Nonlinear Photonic Crystal Nanoresonators

Optische Multistabiliteit in Niet-Lineaire Fotonisch Kristal Resonators

(met een samenvatting in het Nederlands)

Proefschrift

ter verkrijging van de graad van doctor aan de
Universiteit Utrecht
op gezag van de
rector magnificus, prof. dr. H.R.B.M. Kummeling,
ingevolge het besluit van het college voor promoties
in het openbaar te verdedigen op

woensdag 10 mei 2023 des middags te 12.15 uur

door

Karindra Liem Perrier
geboren op 19 november 1986
te Amsterdam

Promotor:
Prof. dr. A.P. Mosk

Copromotor:
Dr. S. Faez

Beoordelingscomissie:
Prof. dr. R.A. Duine
Prof. dr. A. Meijerink
Prof. dr. C. de Morais Smith
Prof. dr. P. van der Straten
Prof. dr. W.L. Vos

Dit proefschrift werd (mede) mogelijk gemaakt met financiële steun van NWO (Nederlandse Organisatie voor Wetenschappelijk Onderzoek) (Vici 68047618).

Contents

1

Introduction

We as a species cannot help it, we want to understand and manipulate the world around us. For sheer survival, as a means to make life more comfortable, to communicate and celebrate, to give life meaning, to leave a mark. Understanding and manipulating go back and forth in a cycle of imagining, trying, practising and unraveling. The experiment is what it is all about.

One look at our historic timeline will give away that our relationship with our surroundings was often defined by our mastering of different materials. The Stone Age, Bronze Age and Iron Age. The capability to make tools for agriculture, build ships, write down and pass on ideas, the industrial revolution, several energy transitions, and eventually the Digital Age (very tellingly, also the Silicon Age). All of it relies on our collective grip on the resources of this world.

Light is one of the most fascinating phenomena that has had humanity's attention all along, but it has become more accessible for experimentation and manipulation not too long ago with the advent of modern physics and realization of laser light in the sixties [1]. With the proposal of photonic crystals, advanced control over the guiding and trapping of light came within reach [2–4]. Photonic crystals are periodic dielectrics, materials with a pattern of contrasting refractive indices on the order of the light wave. They are engineered to have a photonic band gap: propagation at certain ranges of wavelengths is forbidden [5,6]. For these wavelengths they are perfect mirrors. This property makes that they can be designed to confine and guide light in one-, two- or even three dimensions, with the first demonstration of a three-dimensional photonic crystal in 1991 with a band gap for microwaves [7].

The production of three-dimensional photonic bandgap crystals has proven to be very challenging. Various routes to obtain such crystals for visible and near-infrared wavelengths were explored, including templating [8], directed assembly [9], wafer stacking [10], directional etching [11,12] and additive manufacturing [13]. Honing the fabrication of nanostructures with electron-beam lithography and etching techniques [14–17] opened up the new field of photonic crystals around the start of this century. It led to the development of two-dimensional photonic crystals [18], two-dimensional waveguides [19–22], microresonators [23–28] and nanoresonators [29–33].

The concepts we use in photonics are analogous to principles of electronics of the Digital Age. In fact, the word photonics is a contraction of photon and electronics [34–36]. Our understanding of the electrical properties of semiconductor materials has led to the transistor, integrated circuits and the electronics revolution that changed our daily lives. Photonic crystals are used in photonic integrated circuits, the optical counterpart of integrated circuits [37–40]. They can be used for many optical communication devices like add-drop filters [41,42], all-optical switches [43–49] and logic gates [50–52], slow light [53] applications like buffering [54–57], optical computing [58,59], optical memory [60,61], optical neural

networks[62], and quantum photonics[63–66]. A much wider range of applications make use of the possibilities that photonic crystals offer, for instance in more fundamental research[67–71], but also fields like (bio)sensing[72–75], defense technology[76,77] and solar energy[78–85]

1.1 Photonic Crystals

Photonic crystals are periodic structures, mostly made from dielectrics, consisting of repeating patterns of different materials with contrasting refractive index n. Because the lattice constant is on the order of the wavelength of light it affects the ways in which these waves can 'fit' in the medium. As a consequence, the solutions to the Maxwell equations form bands of frequencies with which the light can propagate through the photonic crystal. These bands do not always fill the spectrum continuously. When the bands are disconnected it leaves a 'photonic band gap', *i.e.*, a range of frequencies for which light can not propagate. In general, modes in an N-dimensional photonic crystal are Bloch states

$$\mathbf{E}_{\mathbf{k}}(\mathbf{r}) = e^{i\mathbf{k}\cdot\mathbf{r}}\mathbf{u}_{\mathbf{k}}(\mathbf{r}), \tag{1.1}$$

where $\mathbf{E}$ is the electric field (related to the magnetic field by the Maxwell equations), $\mathbf{k}$ is the Bloch wave vector, $\mathbf{r}$ position, and a function $\mathbf{u}_{\mathbf{k}}(\mathbf{r})$ with lattice periodicity $\mathbf{u}_{\mathbf{k}}(\mathbf{r}) = \mathbf{u}_{\mathbf{k}}(\mathbf{r} + \mathbf{R})$ for all lattice vectors $\mathbf{R}$.

In Fig. 1.1 we look at a one-dimensional photonic crystal consisting of alternating slabs with contrasting n to understand why the band gap occurs. Incoming light with its frequency inside the band gap is fully reflected due to destructive interference. Electromagnetic waves at the band edge form standing waves with $k = \pi/a$ that fit the crystal in one of two ways, with the nodes inside the high-n material or inside the low-n material. This determines where the majority of the energy of the electromagnetic wave is stored: for the bottom 'dielectric' band most of the energy is stored in the high n slab, for the upper 'air' band most of the energy is stored in the low n slab. Often the low n material is air, hence the nomenclature. This picture does not generalize perfectly to two or more dimensions[86]. Close to the band gap the group velocity of propagating modes approaches zero due to dispersion. This low group velocity is commonly called slow light.

The occurrence of the band gaps extends to two or three dimensions, creating the situation of forbidden light propagation in the xy-plane of the crystal or even full extinction of certain photon energies in all directions for 3D crystals[48,88]. When a defect is placed inside this photonic crystal, the defect is surrounded by band-gap material, and light inside this defect is confined inside the defect structure. In this way, one can design waveguides by line defects, or cavities by point defects.

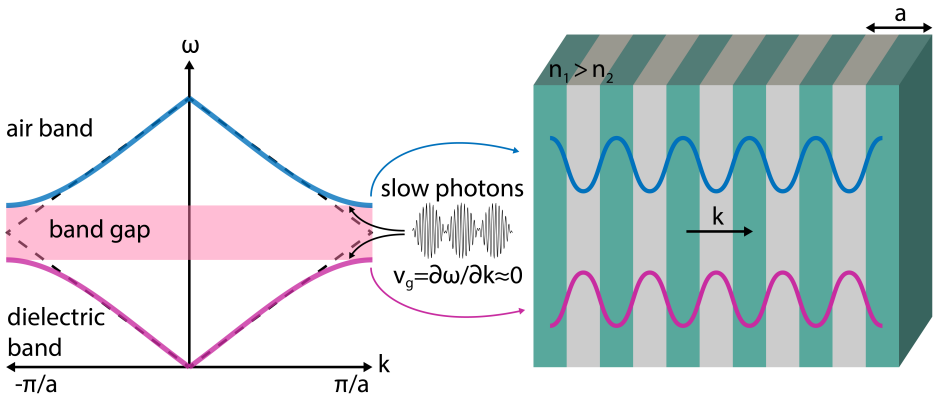

Figure 1.1: (left) Illustration of the band structure of a 1D photonic crystal with a photonic band gap. (center) Close to the band edge dispersion leads to very slow group velocity. (right) Schematic of the 1D photonic crystal consisting of alternating high and low refractive index slabs. At the band edge, electromagnetic waves can fit the crystal one of two way, each associated with a specific band. Figure inspired by Likodimos, p. 271 [87]

Two-dimensional photonic crystals can take many forms as long as the structure is periodic in two dimensions, like pillar grids, square grids of crossing beams, or grids of air holes [31,89–92]. Notably, even quasiperiodic materials and hyperuniform disordered materials have shown complete band gaps and high-quality (Q) cavities [93–96]. In this thesis we are interested in photonic crystal membranes, thin slabs of semiconductor material with a two-dimensional pattern of air holes. The photonic crystal slabs are therefore not strictly two-dimensional. They can be situated on top of a substrate or suspended in air connected to the substrate at the edges (in a geometry known as a bridge membrane).

In Fig. 1.2 we show the band structure of a photonic crystal membrane with a hexagonal air hole pattern. One row of air holes is removed, forming a waveguide. The band structure is polarization dependent and in this case designed for transverse electric (TE)-like light, it can be tuned with the lattice constant a and the air hole size. It is important that the light cannot escape to free space modes. The frequency of the light (proportional to the energy in electronic systems) is expressed as $\omega = c|\mathbf{k_0}| = c\sqrt{k_\parallel^2 + k_\perp^2}$, with $\mathbf{k_0}$ the wave vector in free space. Modes with a nonzero component $k_\perp$ perpendicular to the plane of the crystal can have any frequency since $k_\perp$ can take any value. They form a light cone with a continuum of unconfined modes above the light line $\omega = ck_\parallel$. On and below the

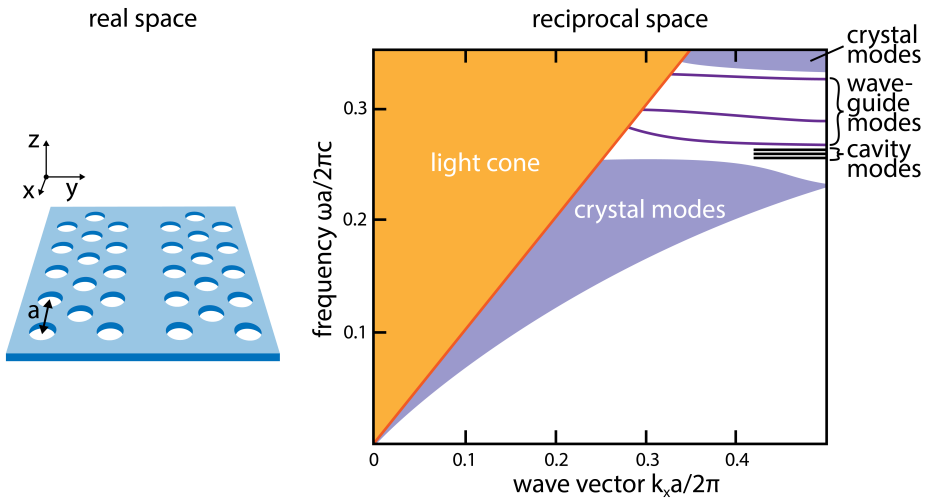

Figure 1.2: (left) Schematic of photonic crystal membrane with triangular air hole pattern with crystal lattice constant a and line defect to create a waveguide. (right) Illustrative band structure in reciprocal space along the k_x axis. Indicated are the light cone, the extended modes inside the crystal membrane, and the modes in the waveguide confined by the band gap. Just above the band edge the localized cavity resonances are indicated in black. Figure inspired by Joannopoulos, p. 143 [36]

light line all modes propagate in-plane with the crystal, where certain modes are forbidden or confined by the band gap. Inside the bulk of the photonic crystal a continuum of modes exist below and above the band gap. Inside the band gap we have the discrete bands of waveguide modes. We call them band gap-guided modes since the confinement is provided by the band gap. Other mode bands, confined by the refractive index contrast between membrane and surrounding medium (usually air), are called index-guided bands since they are confined by internal reflection at the surface of the crystal.

In addition to line defects creating waveguides, it is possible to create cavities with different types of point defects like removing air holes, varying air hole radius, or air hole displacement [31,88,97–103]. For this research we are interested in mode-gap resonators, width modulation of the waveguide as point defect cavities. Fig. 1.3 shows the principle of a mode-gap resonator, the shift of the air holes is exaggerated for clarity. The cavity gives rise to a localized resonance with a frequency just above the band edge and below the first waveguide mode.

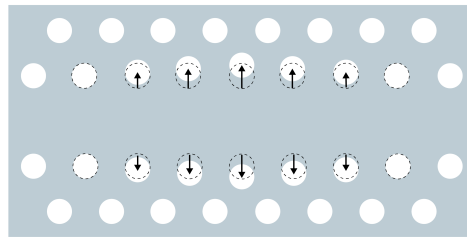

Figure 1.3: Schematic of a mode-gap cavity. Waveguide width modulation is created by shift of air holes away from their default position, acting as a point defect resonator.

1.2 Applications

The opportunity to manipulate the way light flows, localizes and interacts with the medium is used in many different ways, both in fundamental research as well as experiments towards applied science. Here, we look at some examples to illustrate what photonic crystals have to offer and give context to the research of the thesis.

The characteristic of photonic crystal resonators to strongly localize light in cavities with high quality factor Q and small mode volume [104,105] makes that nonlinear effects are relevant at micro Watts input power. The optical nonlinearity in the photonic crystal material provides bistability, or even multistability, with several stable states that have application in optical memory [43–49,106–112]. The optical history of the photonic crystal determines the current state, which can be used as an optical switch between an 'on' and 'off' output signal [43]. Since photonic crystal resonators are extremely sensitive to the refractive index pattern one can easily design cavities specifically tuned for certain wavelengths. This is illustrated in Fig 1.4(a) with the intracavity energy against wavelength plots below each cavity, depicting a bistable range that offers two stable states for different wavelength bands. The waveguide on the other hand provides a multi-band infrastructure. Thus photonic crystals can facilitate wavelength division multiplexing platforms, guiding several wavelengths of light, and having the capacity to do separate signal processing on the untangled bands [57,113].

As different modes can propagate or resonate in a photonic crystal, things become more and more interesting when we have full control over the optical state the system is in. Especially when these different states can be addressed, imaged, or even shaped, all-optically [114–116]. Photons with energies that supersede the electronic band gap can be absorbed by the photonic crystal and excite a carrier pair which, after a certain lifetime, dissipates heat and recombine. Both

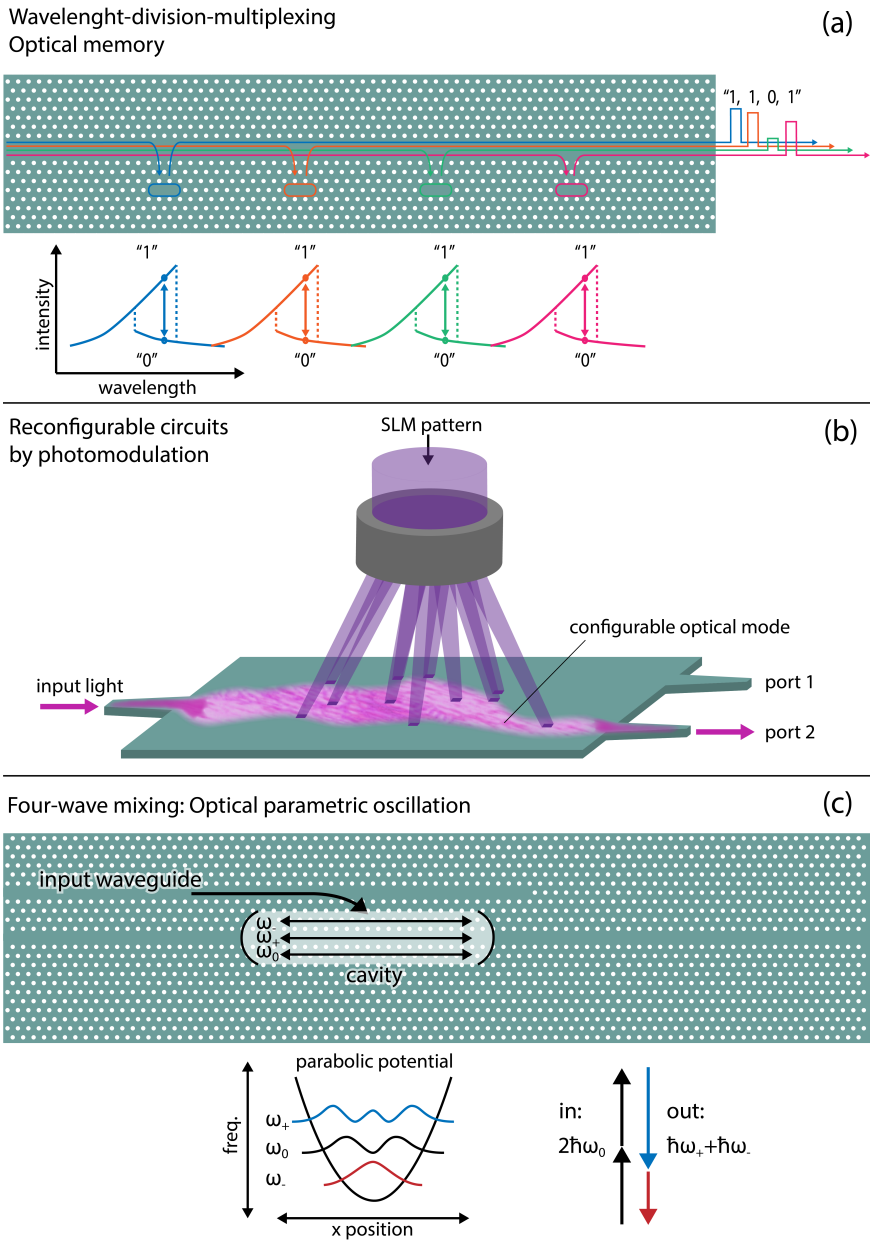

Figure 1.4: Illustrative examples of photonic crystal experiments and applications. ... caption continues on next page

Figure 1.4: continued from previous page
... (a) A photonic crystal with four cavities evanescently coupled to a waveguide. Each cavity is tuned to its own wavelength band. Optical bistability in each cavities facilitates the possibility to stabilize a cavity in one of two optical states: "0" (low intracavity energy) and "1" (high intracavity energy). Schematic intensity response curves below each cavity demonstrating bistable wavelength ranges. (b) Manipulating the optical mode in the membrane by out-of-plane photomodulation, *i.e.*, an optical pump that changes the local refractive index. A spatial light modulator (SLM) is used to program the pump pattern and shape the mode to select an output port. (c) A high quality photonic crystal waveguide cavity and the $\chi^{(3)}$ nonlinearity in the material are used to stimulate four-wave mixing and create an optical parametric oscillator, *i.e.*, an optical device that converts 2 pump photons with frequency ω_0 into two photons with frequency ω_+ and ω_-.

the carrier concentration and the temperature change lead to a change in the refractive index. This process is the basis for photomodulation: changing the local refractive index by use of an optical pump. Fig. 1.4(b) illustrates how photomodulation can be used to make reconfigurable optical devices by shaping the optical mode inside the membrane using a photomodulation pattern [117,118]. Several other examples in which one uses this principle is the thermal tuning of modes to compensate fabrication imperfections or achieve necklace states [119,120], and spatial light modulation [121].

Besides optical bistable switching experiments, the nonlinearity in a photonic crystal can be used for multiple purposes. For instance, in Fig. 1.4(c) we illustrate wavelength conversion in an optical parametric oscillator, achieved with four-wave mixing optics, where the two incoming photons are converted into two outgoing photons with different wavelength [122–124]. Here, the aptitude of photonic crystals to enhance nonlinear effects [125] combined with the possibility to thermo-optically tune the cavity resonance [119], is exploited to stimulate the four-wave mixing process. Specifically, the cavity has an effective parabolic potential for the photons that is triply resonant with the frequencies part-taking in the four-wave mixing.

A topic of specific interest is optical multistability achieved with nonlinearity in photonic crystals, observed in nonlinear coupled ring resonators [107–109] and microresonators [110]. Tristability has been demonstrated in optical fibers [111] and pillar microcavities [112]. Purposefully switching between three states has been shown for three-level atoms in a ring resonator [126,127].

In our experiment, we take a system of coupled nanoresonators and use the nonlinearity in the photonic crystal to achieve optical multistability. We manipulate the state of the system by out-of-plane photomodulation, moving through

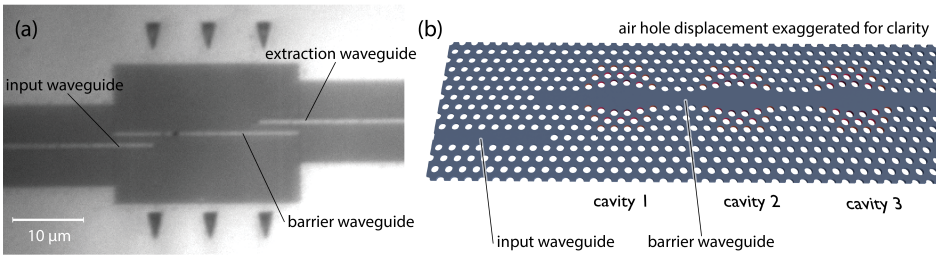

Figure 1.5: (a) Photograph of our photonic crystal. (b) Schematic rendering of our photonic crystal design with the injection waveguide and three mode-gap cavities on the barrier waveguide.

its phase space between stable states characterized by their intracavity energy.

1.3 Fabrication

We now look at the design and fabrication of the photonic crystal we use in this research. In Fig. 1.5 we show a photograph (a) and schematic rendering (b) of our photonic crystal membrane. Fabrication of photonic crystals is a very demanding process. It was done by our collaborators Alfredo de Rossi, Sylvain Combrié and co-workers at Thales Research and Technology, France [122,128,129]. Here, we described the fabrication in so far relevant for the scope of this thesis. It requires the etching of deep cylindrical air holes with straight side walls, smooth surfaces and sharp edges. Disorder in the shape, size or positioning of the air holes is very unforgiving, as variations on the order of 1 nm can lead to unwanted resonance shifts of more than a nanometer. Several fabrication steps are involved of letting crystal layers grow on a substrate and then undergo lithography, etching and chemical washing phases.

In Fig. 1.6 we illustrate the fabrication process. Firstly, a stack of two $Ga_{0.51}In_{0.41}P$ (InGaP) layers with a GaAs layer in between is epitaxially grown by metalorganic chemical vapor deposition, lattice matched to a GaAs substrate. A SiO_2 layer is added as a hard mask. On top, a layer of polymethyl-methacrylate (PMMA) is spin-coated to form a photoresist soft mask. With electron-beam lithography the photonic crystal pattern is printed to the PMMA, after which it is developed in a methyl isobutyl-ketone solution (MIBK). The e-beam lithography exposes the sample with fields of a certain size. Although the photonic crystal cavities fit well inside one field, the entirety of the waveguide will not. Therefore several fields are needed in consecutive exposure times, where it is crucial to match the edges of the fields as precise as possible. The meeting edges of

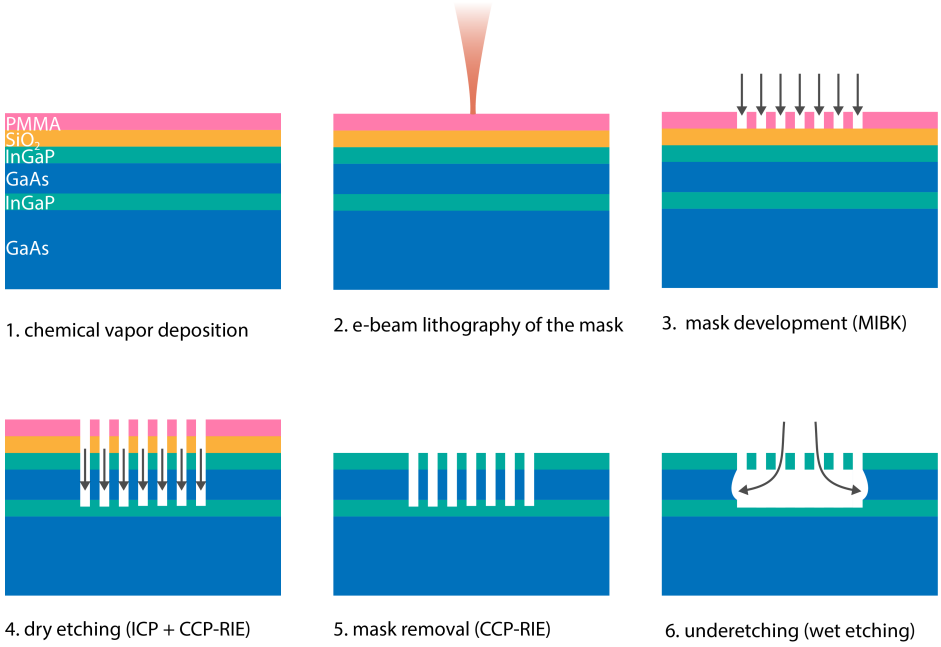

Figure 1.6: The photonic crystal fabrication steps using electron-beam lithography. Figure inspired by Marty, p.65 [123].

the fields we call stitches. Often, unintentional resonant defects can arise at the stitches.

The photonic crystal pattern is transferred to the underlying layers with two different dry etching techniques, first onto the SiN layer with capacitively coupled plasma reactive ion etching (CCP-RIE), and then deepened into the InGaP and GaAs layers with an inductive coupled plasma (ICP). CCP-RIE is then used again to remove the hard mask. And finally the top InGaP layer is made suspended by under-etching, using a wet etching technique such that it removes just enough of the sacrificial GaAs an InGaP sublayers.

1.4 Optical Nonlinearity

As a material property of the photonic crystal semiconductor we have several types of optical nonlinearity. Here we discuss the most important ones for our photonic crystal.

Our photonic crystal is designed for the telecom C band, *i.e.*, around 1550 nm near infrared (NIR) light. InGaP has a large electronic band gap of 1.9eV [130]

which prevents one- and two photon absorption inside the slab. However, due to surface states, or possibly $\chi^{(2)}$ nonlinearity in the bulk [123,131], there is a small fraction of second harmonic generation. This up-converted light can be observed via out-of-plane scattered light when a mode has a large enough intracavity energy. Yet, this second harmonic light is not suitable for the measurement of the spatial mode profile of a state because only the very intense states produce enough light for detection, and the out-of-plane scattered light interferes with itself. More importantly, we don't know the mechanism and whether the $\chi^{(2)}$ nonlinearity is maybe inhomogeneous, for example due to impurities or water layers at the surface.

We also have third-order nonlinear optics effects present in the medium, *i.e.*, $\chi^{(3)}$ nonlinearity [132]. One of these is the optical Kerr effect. We treat it in detail later on in this section. Additionally, four-wave mixing is a $\chi^{(3)}$ nonlinearity recently used in wavelength conversion experiments and applications in micro- and nanoresonators [122–124].

The dominating nonlinearity in the medium in our experiments is thermo-optical nonlinearity. So far we have discussed light in the photonic crystal that either scatters, propagates or forms standing waves. However, a photon with an energy exceeding the electronic band gap can be absorbed by the material. An electron in the valence band is then excited to the conduction band, after which it thermalizes, dissipating phonons into the lattice, and finally recombine. In this way, one can pump the medium with a visible light source and locally heat the crystal, inducing an expansion of the lattice and thereby changing the local refractive index. We use this principle during this thesis to probe the spatial information of the optical modes in the photonic crystal. We note here that free carriers also directly change the refractive index of the crystal, an effect that has been used for ultrafast switching of photonic crystals and resonators [117,118,133–136]. In our case, this effect is negligible compared to the thermal effects.

Despite the band gap, absorption at longer wavelengths is also significant. Impurities are inherent to the photonic crystal material, leading to electronic trapped states and defect states. Additionally, there are surface states that create states inside the electronic band gap, specifically, water on the surface and possibly hydrocarbons oxides or other materials. These states allow absorption of NIR light inside the electronic band gap, leading to a fraction of the probe light energy to dissipate into the lattice and heat up the photonic crystal. The effect becomes relevant when there is enough energy in the mode such that the fraction of absorbed light leads to a significant temperature increase, meaning it leads to a shift of resonance on the order of the linewidth. This is the nonlinear regime.

Crucially, the thermal source is the optical mode itself, and thus the thermal profile of NIR absorption will follow from it. This self-heating effect is the prin-

ciple behind nonlinear behavior in cavities probed with high NIR power. Asymmetric spectral lineshapes with bistable regimes of two stable energy branches for the same wavelength are the result. This is treated in detail in Chapter 3, Section 3.2.

Thermo-optical- and Kerr nonlinearity

Thermo-optical nonlinearity is often confused with $\chi^{(3)}$ nonlinearities like Kerr nonlinearity. For clarification we treat the differences between the two here.

The optical Kerr effect causes an instantaneous nonlinearity, where the electric component of an incoming electromagnetic wave changes the overall refractive index of a material, such that

$$n_{\text{Kerr}}(I) = n_0 + \frac{3}{2n_0\epsilon_0}\chi^{(3)}|\mathbf{E}|^2 \equiv n_0 + n_2 I, \tag{1.2}$$

where n_0 is the unperturbed (linear) refractive index of the medium, ϵ_0 is the vacuum permittivity, $\chi^{(3)}$ is the third order electric susceptibility, and n_2 is the second-order nonlinear refractive index. Thus the shift in refractive index is proportionate to I the intensity of the incoming light [6]. It is caused by the driven motion of the electrons in the lattice where the potential induced by the incoming electromagnetic wave isn't perfectly harmonic and thus raises a third order term that affects the refractive index of the material. The Kerr effect allows for ultrafast switching but requires high laser intensities that can only be provided by femtosecond pulses [137].

For thermo-optical nonlinearity we also have a refractive index shift that is proportional with I. This can be understood when we look at the bare frequency $\tilde{\omega}_0$, *i.e.*, the unperturbed frequency of the resonance at room temperature T_0, which can be thermo-optically detuned by a temperature change due to absorption of part of the light. The bare frequency is shifted with thermal detuning δ_{th} which for our experiment is linearly related to temperature change $\Delta T = T - T_0$, such that

$$\omega_0 = \tilde{\omega}_0 + \delta_{th} \equiv \tilde{\omega}_0 + \eta\Delta T. \tag{1.3}$$

Because the local temperature $T(x, y)$ on the photonic crystal is determined by the intracavity energy of the resonator we have that $\Delta T \propto |E|^2 \propto I$ and thus

(1.4)

However, the shift is caused by absorption of light by the resonator leading to thermal detuning of its resonance. The absorbed light can either be cavity probe light that has a wavelength close to cavity resonance, or absorption of pump

light that has a photon energy exceeding the band gap of the crystal such that it can excite a carrier. In both cases there are absorption and diffusion processes that are related to optical detuning effects which need time to reach equilibrium. It is therefore an indirect, non-instantaneous effect with a timescale determined by thermo-optical relaxation. The thermo-optical nonlinearity cannot be defined in a nonlinear susceptibility term, as it does not affect the polarization of the photonic crystal. In summary, it is a relatively slow effect that scales with I but cannot be classified as $\chi^{(3)}$ nonlinearity.

1.5 The Thermo-optical Model

The physics of the photonic crystal is based on the interplay between the optical resonance condition of the resonators and the temperature distribution in the resonators. We first look at the spectral information and derive the coupled-mode theory describing the optical fields in our photonic crystal. Secondly, we look at the thermal information and identify the different thermo-optical sources and thermal dissipation processes to derive the heat equation of our system. We then couple the discrete coupled-mode theory to the continuum heat equation and numerically solve the system of equations.

Coupled-mode Theory

We are interested in a system that can manipulate the optical state on a chip by (un)coupling an array of cavities. Therefore, we now discuss the coupled resonator system we use for this research. Earlier, we looked at the band structure of a waveguide and described how waveguide width modulation creates cavities on the waveguide. Fig. 1.7 shows a schematic of the resonator array with in panel (a) the input waveguide, the barrier waveguide and the array of three mode-gap cavities. The input waveguide has a width of $W_0 = 1.1\sqrt{3}a$ through which a wide spectral range of NIR probe light can be injected into the photonic crystal. The more narrow barrier waveguide adjacent to it has a width of $W_0 = 0.98\sqrt{3}a$. It blocks the injected light for states with insufficient energy, *i.e.*, for frequencies just above the band edge to mid band gap. The cavities on the barrier approach the width of the input waveguide, they have a width of $1.0048\sqrt{3}a$ at the center. They provide a local defect that allows modes that cannot propagate in the barrier waveguide. Due to the width of the injection waveguide these modes do propagate through the injection waveguide, facilitating evanescent incoupling. When the cavities are coupled by spatial and spectral proximity, the light couples to adjacent cavities and reaches the output waveguide.

In Fig. 1.7(b) we show a schematic of the photonic crystal waveguide with all of the coupling rates and loss rates. It is a visual representation of the coupled mode

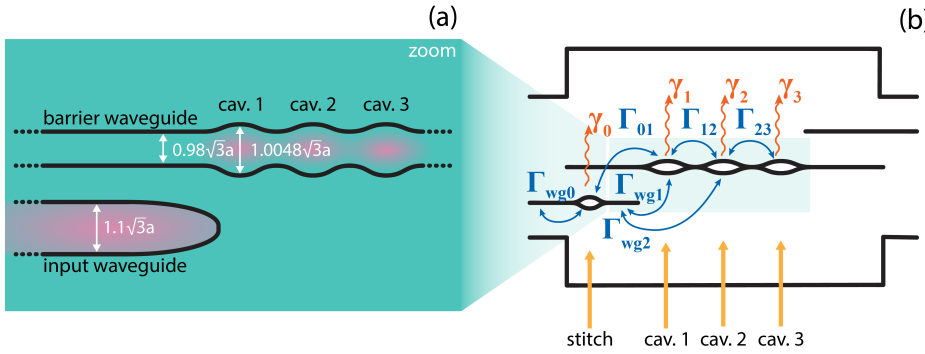

Figure 1.7: Schematic of our photonic crystal. (a) The input waveguide, barrier waveguide and mode-gap resonators, illustrating the width of each of them. Because the width of the mode-gap resonators approaches the width of the input waveguide, modes with energies that are prohibited by the barrier waveguide can evanescently couple to the first cavity and then couple through to the others. (b) Schematic of the coupled mode theory describing our photonic crystal with all the coupling rates and loss rates.

theory we use to describe the spectral component of our resonators. We have incoupling rates between each resonator and the input waveguide $\Gamma_{\mathrm{wg}i}$ except for the third cavity (its coupling to the input waveguide is negligible), and we assume next neighbour coupling between adjacent resonators Γ_{ij}. Beside the three mode-gap cavities, we identify an unintentional stitch mode, generated by the stitch between e-beam fields as described before.

We express the coupled resonators in a system of differential equations using coupled mode theory as follows. The time evolution of the amplitude $A_i(t)$ for each resonator i is expressed in the matrix equation as $d\mathbf{A}/dt = \mathbf{MA} + F\mathbf{S}$, where $\mathbf{M}$ is the coupling matrix, $\mathbf{A}$ is the amplitude vector, $\mathbf{S}$ is the input vector that represents the optical drive via the waveguide, and the prefactor F is the driving amplitude determined by the input power. All coupling rates, loss terms and driving forces depicted in Fig 1.7(b) are taken into account, such that

$$\mathbf{M} = -\begin{bmatrix} i\omega_0 + \gamma_0' & i\Gamma_{01} + \sqrt{\Gamma_{\mathrm{wg0}}\Gamma_{\mathrm{wg1}}} & \sqrt{\Gamma_{\mathrm{wg0}}\Gamma_{\mathrm{wg2}}} & 0 \\ i\Gamma_{01} + \sqrt{\Gamma_{\mathrm{wg0}}\Gamma_{\mathrm{wg1}}} & i\omega_1 + \gamma_1' & i\Gamma_{12} + \sqrt{\Gamma_{\mathrm{wg1}}\Gamma_{\mathrm{wg2}}} & 0 \\ \sqrt{\Gamma_{\mathrm{wg0}}\Gamma_{\mathrm{wg2}}} & i\Gamma_{12} + \sqrt{\Gamma_{\mathrm{wg1}}\Gamma_{\mathrm{wg2}}} & i\omega_2 + \gamma_2' & i\Gamma_{23} \\ 0 & 0 & i\Gamma_{23} & i\omega_3 + \gamma_3' \end{bmatrix}, \tag{1.5}$$

$$\mathbf{S} = \begin{bmatrix} \sqrt{2\Gamma_{\mathrm{wg0}}} \\ \sqrt{2\Gamma_{\mathrm{wg1}}} \\ \sqrt{2\Gamma_{\mathrm{wg2}}} \\ 0 \end{bmatrix}, \tag{1.6}$$

where ω_i is the frequency and γ_i' the total loss rate of cavity i. Γ_{ij} is the coupling rate between cavities i and j, and $\Gamma_{\mathrm{wg}i}$ the coupling rate between the input waveguide and cavity i. The intrinsic loss rate γ_i is included in the experimentally measured loss rate γ_i' such that $\gamma_i' = \gamma_i + \Gamma_{ij}$ for all adjacent resonators j. In these equations we use that $\Gamma \ll \omega$ and thus we applied the rotating wave approximation. Also, we treat all coupling rates Γ as constants independent from ω.

We then solve the matrix equation for $d\mathbf{A}/dt = -i\omega\mathbf{A}$ with ω the driving frequency. Note that for a single resonator the solution is a Lorentzian lineshape around ω_i. For coupled resonators you find a spectrum with several peaks and mode splitting when the distance between the resonances is smaller than their coupling.

The Heat Equation

The coupled-mode equations are related to the temperature profiles of the cavities by the thermo-optic effect because the temperature in the resonator determines its frequency $\omega_i(T) = \tilde{\omega}_i + \eta\Delta T$ (see Eq. 1.3). Therefore we find thermo-optical stable states for the system by relating the coupled-mode equations to the heat equations of the photonic crystal.

In Fig. 1.8 we show a schematic of the three thermo-optical sources in the crystal. In Fig. 1.8(a) we depict the processes leading to direct probe light absorption in the photonic crystal. Since the bulk band gap exceeds the probe photon energy by more than a factor two this takes place via surface states, impurities, free electrons in the semiconductor, or a combination of these processes. This probe absorption is the origin of the thermo-optical nonlinearity which causes the well-known hysteresis behavior shown in Fig. 1.8(b) [138,139]. Secondly, Fig. 1.8(c,d) shows how direct heating by the pump causes a redshift of the cold cavity resonance λ_0 when the thermal profile overlaps with the optical mode profile of the

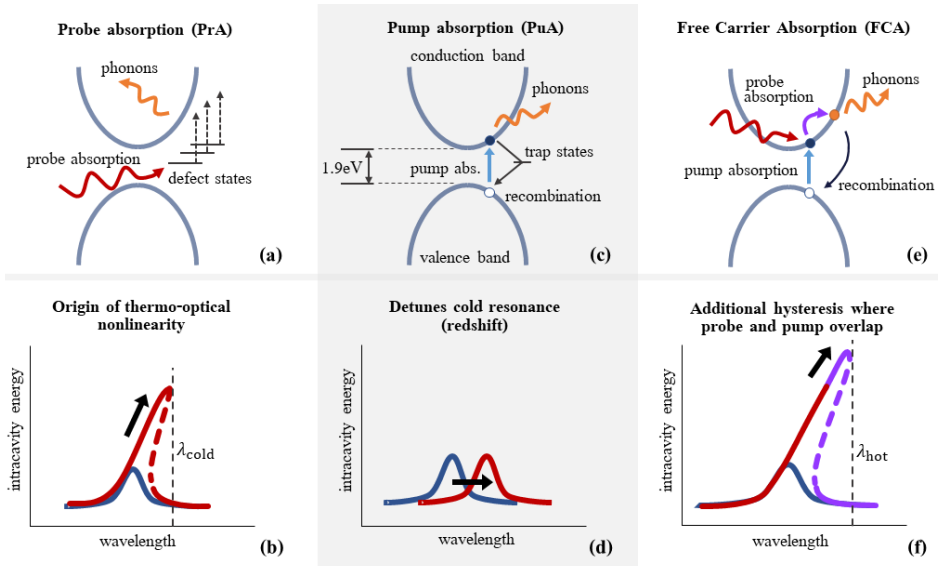

Figure 1.8: Schematic of the thermo-optical sources in the photonic crystal. (a) NIR probe absorption by defect states causes (b) hysteresis behavior at high probe power (red lineshape). The blue lineshape illustrates the low-power, linear response. Dashed lines are instable branches. (c) Interband pump absorption of the 405 nm excitation laser generates a (d) shift of the resonance, *i.e.*, a redshift of the complete lineshape, here depicted for the low-power lineshape. (e) Pump absorption creates free carriers that absorb NIR probe light, *i.e.*, FCA (purple arrow), this causes an (f) increase in the hysteresis in the nonlinear lineshape (red and purple). The right hysteresis edge of the pumped nonlineare lineshape (λ_{hot} in (f)) is redshifted with respect to the hysteresis edge of the unpumped nonlinear lineshape (λ_{cold} in (b)).

resonance[140]. In Fig. 1.8(e,f) a third source of heat presents itself when the free carriers generated by the pump absorb a probe photon, *i.e.*, FCA. Because carrier diffusion is negligible compared to pump spot size these hot carriers locally heat the lattice and increase the thermo-optical redshift, causing an increase in the hysteresis. The FCA process occurs only in the region where the pump spot and optical mode profile overlap, and is proportional to the product of pump and probe energy densities.

First we find an expression for the heat produced by free carrier absorption (FCA) as depicted in Fig. 1.8(e), *i.e.*, free carriers produced by the pump light absorb probe light. To find the thermal dissipation from the FCA source we multiply the optical absorption coefficient with the energy density of the probe field. This gives us the energy transfer from probe light to free carriers, *i.e.*, the FCA heating term,

$$S_{\mathrm{FCA}} = \alpha_{\mathrm{FCA}}(x,y,t) \times \left(\frac{c}{n} E_{\mathrm{pr}}(t) U_{\mathrm{pr}}(x,y) I_{\mathrm{pr}}(x,y,t)\right), \tag{1.7}$$

where $\alpha_{\mathrm{FCA}}(x,y)$ is the probe absorption coefficient, c is the speed of light, n the refractive index, $E_{\mathrm{pr}}(t)$ is the input probe light energy, $U_{\mathrm{pr}}(x,y)$ the optical mode profile of the probe field, and $I_{\mathrm{pr}}(x,y,t)$ is the spectral lineshape of the resonance.

The probe energy is determined by the input probe power P_{pr} and a coupling parameter τ_{pr} accounting for the incoupling efficiency of the probe light to the cavity, which means $E_{\mathrm{pr}}(t) = \tau_{\mathrm{pr}} P_{\mathrm{pr}}(t)$. The absorption coefficient is related to the effective FCA cross section σ_{FCA} and the carrier density $\rho_c(x,y)$ such that $\alpha_{\mathrm{FCA}}(x,y,t) = \sigma_{\mathrm{FCA}} \rho_c(x,y,t)$, where the effective absorption cross section is the summed cross sections of all carrier types and for each type $\sigma_i = e^3 \lambda_{\mathrm{pr}}^2 / 4\pi^2 c^3 (m_i^*)^2 \mu_i n \varepsilon_0$ is the absorption cross section of a single carrier[141]. Here e is the electron charge, λ_{pr} the probe wavelength, m^* the effective carrier mass, μ is the carrier mobility and ϵ_0 the vacuum permittivity.

The carriers are excited by the pump light. We assume the carriers stay localized on the optical timescale[142], which means the carrier density is directly proportional to the local production rate of carriers and their lifetime, such that

$$\rho_c(x,y,t) = \frac{\tau_c}{d\hbar\omega_{\mathrm{pu}}} P_{\mathrm{pu}}(t) U_{\mathrm{pu}}(x,y), \tag{1.8}$$

with τ_c the average lifetime of a carrier, d the thickness of the membrane, ω_{pu} the pump light frequency, $P_{\mathrm{pu}}(t)$ the pump power, and $U_{\mathrm{pu}}(x,y)$ the optical mode profile of the pump. This finally leads to the expression

$$S_{\mathrm{FCA}} = \sigma_{\mathrm{FCA}} \left(\frac{\tau_c}{d\hbar\omega_{\mathrm{pu}}} P_{\mathrm{pu}}(t) U_{\mathrm{pu}}(x,y) \right) \times \left(\frac{c\tau_{\mathrm{pr}}}{n} P_{\mathrm{pr}}(t) U_{\mathrm{pr}}(x,y) I_{\mathrm{pr}}(x,y,t) \right). \tag{1.9}$$

We formulate the heat equation, taking into account all thermo-optical sources (shown in Fig. 1.8). It is a partial differential equation which we solve using a stable spectral method on a high-resolution space-time grid. We combine the in-plane cooling through dissipation in the photonic crystal membrane, out-of-plane cooling via the surrounding gas layer and substrate, and all heating terms, including the FCA term of Eq. (1.9), into the heat equation

$$\begin{aligned} C_{\mathrm{2D}} \frac{\partial T(x,y,t)}{\partial t} = & \\ & -K_{\mathrm{2D}} \nabla^2 T(x,y,t) \\ & -K_{\mathrm{gas}} (T(x,y,t) - T_0) \\ & +\alpha_{\mathrm{prA}} P_{\mathrm{pr}}(t) U_{\mathrm{pr}}(x,y) \\ & +\beta_{\mathrm{puA}} P_{\mathrm{pu}}(t) U_{\mathrm{pu}}(x,y) \\ & +\sigma_{\mathrm{FCA}} \frac{\tau_{\mathrm{c}}}{d\hbar\omega_{\mathrm{pu}}} P_{\mathrm{pu}}(t) U_{\mathrm{pu}}(x,y) \\ & \qquad \times \frac{c\tau_{\mathrm{pr}}}{n} P_{\mathrm{pr}}(t) U_{\mathrm{pr}}(x,y) I_{\mathrm{pr}}(x,y,t), \end{aligned} \tag{1.10}$$

where C_{2D} is the 2D specific heat of the photonic crystal membrane, K_{2D} the thermal conductivity of the photonic crystal membrane, and K_{gas} the thermal conductance of the gas layer between the air-suspended membrane and substrate. At the boundary we have $T = T_0$ the temperature at the edge of the photonic crystal where it meets the substrate. Out-of-plane cooling via the other side of the photonic crystal membrane into free space is neglected, as this contributes less then one percent of the heat loss. For the heat produced via probe absorption we take into account the absorption fraction α_{PrA}, *i.e.*, the probability a cavity photon is absorbed rather than scattered or leaked out of the cavity. Direct pump heating is related to β_{PuA}, the absorption fraction of the pump light.

The 2D specific heat is given by

$$C_{\mathrm{2D}} = h\phi\rho C_{\mathrm{sp}}, \tag{1.11}$$

with h the slab thickness of the photonic crystal membrane, ϕ the filling fraction of the photonic crystal, ρ the density and C_{sp} the specific heat of the semiconductor material. The thermal conductivity K_{2D} is approximated as $h\phi\kappa$ where

κ is the thermal conductivity of the semiconductor. Out-of-plane conductance through the gas layer is modeled by $K_{\text{gas}} = \kappa_{\text{gas}}/d_{\text{gas}}$, where d_{gas} is the distance between the membrane and the substrate. The contribution of the gas to the in-plane thermal conductance is neglected, as it is much smaller than the membrane conductance.

Solving the System of Thermo-optical Equations

The thermal and optical equations of the model are coupled in the optical energy density of the probe field. On timescales longer than cavity photon lifetime, the optical energy density adheres to the resonances condition, *i.e.*, the Lorentzian lineshape, such that it can be expressed as

$$U_{\text{opt}}(x,y,t) = E_{\text{in}} U_{\text{mode}} \frac{\Gamma^2}{\Gamma^2 + (\Delta - \delta_{\text{th}}(x,y,t))^2}, \tag{1.12}$$

where E_{in} is the optical input energy of the probe, U_{mode} is the spatial distribution of the optical mode profile, Γ is the resonance linewidth, $\Delta \equiv \lambda_{\text{pr}} - \lambda_0$ is the detuning, and $\delta_{\text{th}}(t)$ is the thermal resonance shift that causes a dynamic detuning expressed by

$$\delta_{\text{th}}(x,y,t) = \eta \iint U_{\text{pr}}(x,y) T(x,y,t) dx dy. \tag{1.13}$$

Here, η is the thermo-optical coefficient of the semiconductor material. Eq. (1.12) reflects the fact that the resonance has a dynamic Lorentzian lineshape that detunes in accordance with the temperature. For our experimental conditions the resonance frequency detunes linearly with temperature [143].

We numerically solve the system of equations on a two-dimensional time grid, *i.e.*, for $T(x,y,t)$ the temperature distribution at time t. We initialize the photonic crystal at room temperature with the resonators at their bare resonance, and evaluate for consecutive steps in time dt. The temperature profiles are expressed in orthogonal modes using Sturm-Liouville theory [144] for computational speed. For every step in time we

1. calculate for each resonator i its thermal shift $\delta_{\text{th}}(x,y,t)$ by taking the dot product of the optical mode profile $U_{\text{pr}}(x,y)$ and the temperature profile $T(x,y,t)$ (see Eq. (1.13))

2. calculate $\omega_i = \tilde{\omega}_i + \delta_{\text{th}}(x,y,t)$

3. solve the CMT matrix equation $d\mathbf{A}/dt = \mathbf{M}\mathbf{A} + F\mathbf{S}$ and find the intracavity energy $|A_i|^2$ for each resonance (see Eq. (1.5)-(1.6))

4. calculate all thermo-optical sources by inserting the intracavity energy into the heat equation letting $\alpha P_{\mathrm{pr}} U_{\mathrm{pr}} = \alpha \omega_i |A_i|^2$, $P_{\mathrm{pr}} U_{\mathrm{pr}} I_{\mathrm{pr}} = |A_i|^2$ and inserting the optical mode profile of the pump U_{pu}.

5. converting the temperature profiles to modes in an orthogonal base using Sturm-Liouville theory, and propagating them for time-step dt, also including in the propagation the cooling terms of Eq. (1.11)

6. using the values for $|A_i|^2$ and $T(x, y, t)$ at the end of dt to initialize the next time-step.

The timesteps are repeated untill a stable state is reached. The final intracavity energy and temperature profile are used to plot the theoretical results in Chapters 3, 4 and 5.

We note that step 5 was solved with Euler's method [145] instead of in the Sturm-Liouville basis set for the theoretical results of Chapter 3. While not efficient, Euler integration is extremely robust as long as the step sizes fulfill the appropriate Courant-Friedrichs-Lewy condition [146].

1.6 Outline of this Thesis

The subject of this thesis is the study of coupled nanocavities on a photonic crystal waveguide, specifically in the optical nonlinear regime. We explore the multistability of the coupled resonators and find control over them by looking at their temporal, spectral, and spatial information.

In this Chapter 1, we introduce the topic of photonic crystals and discuss the fabrication procedure of our photonic crystal in Section 1.3. We then treat the different optical nonlinearities present in the material and expand on the thermo-optical effect and the Kerr effect in Section 1.4. Lastly, we treat the theoretical model we use to reproduce, and gain understanding of, our experimental results in Section 1.5.

In Chapter 2, we introduce the experimental setup and treat all technical aspects of the probing, pumping, and detection scheme. We also discuss the geometrical and material details of our photonic crystal membrane.

In Chapter 3, we determine the timescale of the thermo-optical response of the system by measuring the decay time of the thermal relaxation. As it turns out, the relaxation time is related to the size of the optical mode profile.

In Chapter 4, we present a nonlinear mode mapping method that enhances the resolution drastically. The spatial mapping of an optical mode profile has been demonstrated in our group before, however, its resolution is limited by thermal diffusion. Here, we leverage the high sensitivity of nonlinear high-Q cavities when they are detuned to significantly improve the mode map resolution. This

is achieved through free carrier absorption, where an optical pump generates a plasma with the size of the optical pump spot, and these carriers locally heat the crystal by absorbing photons from the probe light.

In Chapter 5, we present an on-demand writing method of optical states in a 'photonic molecule', a system of coupled nanoresonators that has a multitude of stable thermo-optical states. With the knowledge and techniques of the previous chapters we utilize the optical multistability of nonlinear coupled resonators. We demonstrate programmed all-optical switching between these multiple stable states by spatial photomodulation with local pulses of an external optical beam. We reproduce the results with our theoretical model and find excellent agreement.

We wrap up with a summary in Chapter 6.

1.7 References

[1] T. H. Maiman, "Stimulated optical radiation in ruby," Nature **187**, 493–494 (1960).

[2] E. Yablonovitch, "Inhibited spontaneous emission in solid-state physics and electronics," Physical Review Letters **58**, 2059 (1987).

[3] S. John, "Strong localization of photons in certain disordered dielectric superlattices," Physical Review Letters **58**, 2486 (1987).

[4] V. P. Bykov, "Spontaneous emission from a medium with a band spectrum," Soviet Journal of Quantum Electronics **4**, 861 (1975).

[5] J. D. Joannopoulos, P. R. Villeneuve, and S. Fan, "Photonic crystals: putting a new twist on light," Nature **386**, 143–149 (1997).

[6] B. E. Saleh and M. C. Teich, *Fundamentals of photonics* (john Wiley & sons, 2019).

[7] E. Yablonovitch, T. Gmitter, and K.-M. Leung, "Photonic band structure: The face-centered-cubic case employing nonspherical atoms," Physical Review Letters **67**, 2295 (1991).

[8] J. E. Wijnhoven and W. L. Vos, "Preparation of photonic crystals made of air spheres in titania," Science **281**, 802–804 (1998).

[9] Y. A. Vlasov, X.-Z. Bo, J. C. Sturm, and D. J. Norris, "On-chip natural assembly of silicon photonic bandgap crystals," Nature **414**, 289–293 (2001).

[10] K. Aoki, D. Guimard, M. Nishioka, M. Nomura, S. Iwamoto, and Y. Arakawa, "Coupling of quantum-dot light emission with a three-dimensional photonic-crystal nanocavity," Nature Photonics **2**, 688–692 (2008).

[11] S. Takahashi, M. Okano, M. Imada, and S. Noda, "Three-dimensional photonic crystals based on double-angled etching and wafer-fusion techniques," Applied Physics Letters **89**, 123106 (2006).

[12] J. Van den Broek, L. Woldering, R. Tjerkstra, F. Segerink, I. Setija, and W. Vos, "Inverse-woodpile photonic band gap crystals with a cubic diamond-like structure made from single-crystalline silicon," Advanced Functional Materials **22**, 25–31 (2012).

[13] M. Hermatschweiler, A. Ledermann, G. A. Ozin, M. Wegener, and G. von Freymann, "Fabrication of silicon inverse woodpile photonic crystals," Advanced Functional Materials **17**, 2273–2277 (2007).

[14] S. Noda and T. Baba, "Physical and experimental background of photonic crystals," in "Roadmap on Photonic Crystals," (Springer, 2003), pp. 1–11.

[15] L. Pang, W. Nakagawa, and Y. Fainman, "Fabrication of two-dimensional photonic crystals with controlled defects by use of multiple exposures and direct write," Applied Optics **42**, 5450–5456 (2003).

[16] K.-H. Lee, "Investigation and fabrication of 2D photonic crystals structures for light emission and optical modes control at 1.55 μm," Ph.D. thesis, Université Paris Sud-Paris XI (2008).

[17] R. W. Tjerkstra, L. A. Woldering, and W. L. Vos, "Photonic crystal fabrication," In "The Encyclopedia of Materials: science and technology", Eds. J. Buschow, R. W. Cahn, M. C. Flemings, B. Ilschner, E. J. Kramer, S. Mahajan, and P. Veyssière (Amsterdam, Elsevier, 2011), vol. 7: Ni-Poi (5 pp.) (2011).

[18] T. F. Krauss, R. M. D. L. Rue, and S. Brand, "Two-dimensional photonic-bandgap structures operating at near-infrared wavelengths," Nature **383**, 699–702 (1996).

[19] M. Notomi, K. Yamada, A. Shinya, J. Takahashi, C. Takahashi, and I. Yokohama, "Extremely large group-velocity dispersion of line-defect waveguides in photonic crystal slabs," Physical Review Letters **87**, 253902 (2001).

[20] T. Baba, N. Fukaya, and J. Yonekura, "Observation of light propagation in photonic crystal optical waveguides with bends," in "Integrated Photonics Research," (Optica Publishing Group, 1999), p. RTuE3.

[21] M. Lončar, D. Nedeljković, T. Doll, J. Vučković, A. Scherer, and T. P. Pearsall, "Waveguiding in planar photonic crystals," Applied Physics Letters **77**, 1937–1939 (2000).

[22] S. Olivier, C. Smith, M. Rattier, H. Benisty, C. Weisbuch, T. Krauss, R. Houdre, and U. Oesterle, "Miniband transmission in a photonic crystal coupled-resonator optical waveguide," Optics Letters **26**, 1019–1021 (2001).

[23] A. Scherer, J. Jewell, Y.-H. Lee, J. Harbison, and L. Florez, "Fabrication of microlasers and microresonator optical switches," Applied Physics Letters **55**, 2724–2726 (1989).

[24] O. Painter, R. Lee, A. Scherer, A. Yariv, J. O'brien, P. Dapkus, and I. Kim, "Two-dimensional photonic band-gap defect mode laser," Science **284**, 1819–1821 (1999).

[25] S. McCall, A. Levi, R. Slusher, S. Pearton, and R. Logan, "Whispering-gallery mode microdisk lasers," Applied Physics Letters **60**, 289–291 (1992).

[26] J. Foresi, P. R. Villeneuve, J. Ferrera, E. Thoen, G. Steinmeyer, S. Fan, J. Joannopoulos, L. Kimerling, H. I. Smith, and E. Ippen, "Photonic-bandgap microcavities in optical waveguides," Nature **390**, 143–145 (1997).

[27] M. Cai, O. Painter, and K. J. Vahala, "Observation of critical coupling in a fiber taper to a silica-microsphere whispering-gallery mode system," Physical Review Letters **85**, 74 (2000).

[28] D. Armani, T. Kippenberg, S. Spillane, and K. Vahala, "Ultra-high-Q toroid microcavity on a chip," Nature **421**, 925–928 (2003).

[29] O. Painter, A. Husain, A. Scherer, J. O'Brien, I. Kim, and P. Dapkus, "Room temperature photonic crystal defect lasers at near-infrared wavelengths in InGaAsP," Journal of Lightwave Technology **17**, 2082–2088 (1999).

[30] J.-K. Hwang, H.-Y. Ryu, D.-S. Song, I.-Y. Han, H.-W. Song, H.-K. Park, Y.-H. Lee, and D.-H. Jang, "Room-temperature triangular-lattice two-dimensional photonic band gap lasers operating at 1.54 μm," Applied Physics Letters **76**, 2982–2984 (2000).

[31] T. Yoshie, J. Vučković, A. Scherer, H. Chen, and D. Deppe, "High quality two-dimensional photonic crystal slab cavities," Applied Physics Letters **79**, 4289–4291 (2001).

[32] H.-Y. Ryu, S.-H. Kim, H.-G. Park, J.-K. Hwang, Y.-H. Lee, and J.-S. Kim, "Square-lattice photonic band-gap single-cell laser operating in the lowest-order whispering gallery mode," Applied Physics Letters **80**, 3883–3885 (2002).

[33] Y. Akahane, T. Asano, B.-S. Song, and S. Noda, "High-Q photonic nanocavity in a two-dimensional photonic crystal," Nature **425**, 944–947 (2003).

[34] M. Krasnodębski, "Throwing light on photonics: The genealogy of a technological paradigm," Centaurus **60**, 3–24 (2018).

[35] I. S. Amiri, S. R. B. Azzuhri, M. A. Jalil, H. M. Hairi, J. Ali, M. Bunruangses, and P. Yupapin, "Introduction to photonics: Principles and the most recent applications of microstructures," Micromachines **9**, 452 (2018).

[36] J. D. Joannopoulos, S. G. Johnson, J. N. Winn, and R. D. Meade, *Molding the flow of light* (2008).

[37] S. Noda and T. Baba, "Examples of various photonic crystal applications," in "Roadmap on Photonic Crystals," (Springer, 2003), pp. 165–241.

[38] L. A. Coldren, S. W. Corzine, and M. L. Mashanovitch, *Diode lasers and photonic integrated circuits* (John Wiley & Sons, 2012).

[39] B. Mukherjee, "WDM optical communication networks: progress and challenges," IEEE Journal on Selected Areas in Communications **18**, 1810–1824 (2000).

[40] C. Qiu, H. Xiao, L. Wang, and Y. Tian, "Recent advances in integrated optical directed logic operations for high performance optical computing: a review," Frontiers of Optoelectronics **15**, 1–17 (2022).

[41] S. Robinson and R. Nakkeeran, "Photonic crystal ring resonator-based add drop filters: a review," Optical Engineering **52**, 060901 (2013).

[42] K. Nozaki, A. Lacraz, A. Shinya, S. Matsuo, T. Sato, K. Takeda, E. Kuramochi, and M. Notomi, "All-optical switching for 10-Gb/s packet data by using an ultralow-power optical bistability of photonic-crystal nanocavities," Optics Express **23**, 30379–30392 (2015).

[43] A. M. Morsy, R. Biswas, and M. L. Povinelli, "High temperature, experimental thermal memory based on optical resonances in photonic crystal slabs," APL Photonics **4**, 010804 (2019).

[44] A. Shinya, S. Matsuo, T. Tanabe, E. Kuramochi, T. Sato, T. Kakitsuka, M. Notomi *et al.*, "All-optical on-chip bit memory based on ultra high Q InGaAsP photonic crystal," Optics Express **16**, 19382–19387 (2008).

[45] Y. Vlasov, W. M. Green, and F. Xia, "High-throughput silicon nanophotonic wavelength-insensitive switch for on-chip optical networks," Nature Photonics **2**, 242–246 (2008).

[46] Q. Saudan, D. A. Bekele, G. Dong, Y. Yu, K. Yvind, J. Mørk, and M. Galili, "Crosstalk-free all-optical switching enabled by Fano resonance in a multimode photonic crystal nanocavity," Optics Express **30**, 7457–7466 (2022).

[47] V. Rutckaia and J. Schilling, "Ultrafast low-energy all-optical switching," Nature Photonics **14**, 4–6 (2020).

[48] T. G. Euser, A. J. Molenaar, J. Fleming, B. Gralak, A. Polman, and W. L. Vos, "All-optical octave-broad ultrafast switching of Si woodpile photonic band gap crystals," Physical Review B **77**, 115214 (2008).

[49] V. Eckhouse, I. Cestier, G. Eisenstein, S. Combrié, G. Lehoucq, and A. De Rossi, "Kerr-induced all-optical switching in a GaInP photonic crystal fabry-perot resonator," Optics Express **20**, 8524–8534 (2012).

[50] H. Wang, S. Ouyang, Y. Shen, and X. Chen, "Ternary optical computer: An overview and recent developments," in "2021 12th International Symposium on Parallel Architectures, Algorithms and Programming (PAAP)," (IEEE, 2021), pp. 82–87.

[51] T. Chattopadhyay and J. N. Roy, "All-optical quaternary computing and information processing: a promising path," Journal of Optics **42**, 228–238 (2013).

[52] S. B. Jo, J. Kang, and J. H. Cho, "Recent advances on multivalued logic gates: a materials perspective," Advanced Science **8**, 2004216 (2021).

[53] M. Notomi, E. Kuramochi, and T. Tanabe, "Large-scale arrays of ultrahigh-Q coupled nanocavities," Nature Photonics **2**, 741 – 747 (2008).

[54] F. Xia, L. Sekaric, and Y. Vlasov, "Ultracompact optical buffers on a silicon chip," Nature Photonics **1**, 65–71 (2007).

[55] H. Takesue, N. Matsuda, E. Kuramochi, W. J. Munro, and M. Notomi, "An on-chip coupled resonator optical waveguide single-photon buffer," Nature Communications **4**, 1–7 (2013).

[56] J. K. Poon, J. Scheuer, Y. Xu, and A. Yariv, "Designing coupled-resonator optical waveguide delay lines," JOSA B **21**, 1665–1673 (2004).

[57] A. Melloni, A. Canciamilla, C. Ferrari, F. Morichetti, L. O'Faolain, T. Krauss, R. De La Rue, A. Samarelli, and M. Sorel, "Tunable delay lines in silicon photonics: coupled resonators and photonic crystals, a comparison," IEEE Photonics Journal **2**, 181–194 (2010).

[58] C. Li, X. Zhang, J. Li, T. Fang, and X. Dong, "The challenges of modern computing and new opportunities for optics," PhotoniX **2**, 1–31 (2021).

[59] A. Biberman and K. Bergman, "Optical interconnection networks for high-performance computing systems," Reports on Progress in Physics **75**, 046402 (2012).

[60] T. Alexoudi, G. T. Kanellos, and N. Pleros, "Optical ram and integrated optical memories: a survey," Light: Science & Applications **9**, 1–16 (2020).

[61] T. Tanabe, M. Notomi, S. Mitsugi, A. Shinya, and E. Kuramochi, "Fast bistable all-optical switch and memory on a silicon photonic crystal on-chip," Optics Letters **30**, 2575 – 2577 (2005).

[62] S. Xiang, Y. Han, Z. Song, X. Guo, Y. Zhang, Z. Ren, S. Wang, Y. Ma, W. Zou, B. Ma *et al.*, "A review: Photonics devices, architectures, and algorithms for optical neural computing," Journal of Semiconductors **42**, 023105 (2021).

[63] A. W. Elshaari, W. Pernice, K. Srinivasan, O. Benson, and V. Zwiller, "Hybrid integrated quantum photonic circuits," Nature Photonics **14**, 285–298 (2020).

[64] G. Moody, V. Sorger, P. Juodawlkis, W. Loh, C. Sorace-Agaskar, A. E. Jones, K. Balram, J. Matthews, A. Laing, M. Davanco *et al.*, "Roadmap on integrated quantum photonics," Journal of Physics Photonics (2021).

[65] A. S. Clark, C. Husko, M. J. Collins, G. Lehoucq, S. Xavier, A. De Rossi, S. Combrié, C. Xiong, and B. J. Eggleton, "Heralded single-photon source in a III–V photonic crystal," Optics Letters **38**, 649–651 (2013).

[66] J. Wang, F. Sciarrino, A. Laing, and M. G. Thompson, "Integrated photonic quantum technologies," Nature Photonics **14**, 273–284 (2020).

[67] P. Lodahl, S. Mahmoodian, and S. Stobbe, "Interfacing single photons and single quantum dots with photonic nanostructures," Reviews of Modern Physics **87**, 347 (2015).

[68] W. Hänsel, P. Hommelhoff, T. Hänsch, and J. Reichel, "Bose–einstein condensation on a microelectronic chip," Nature **413**, 498–501 (2001).

[69] J. Vučković, M. Lončar, H. Mabuchi, and A. Scherer, "Design of photonic crystal microcavities for cavity qed," Physical Review E **65**, 016608 (2001).

[70] D. Vernooy, A. Furusawa, N. P. Georgiades, V. Ilchenko, and H. Kimble, "Cavity qed with high-Q whispering gallery modes," Physical Review A **57**, R2293 (1998).

[71] M. Ghulinyan and L. Pavesi, *Light Localisation and Lasing: Random and Pseudo-random Photonic Structures* (Cambridge University Press, 2014).

[72] Y.-n. Zhang, Y. Zhao, and R.-q. Lv, "A review for optical sensors based on photonic crystal cavities," Sensors and Actuators A: Physical **233**, 374–389 (2015).

[73] B. Troia, A. Paolicelli, F. De Leonardis, and V. M. Passaro, "Photonic crystals for optical sensing: A review," Advances in Photonic Crystals pp. 241–295 (2013).

[74] A. Sinibaldi, "Cancer biomarker detection with photonic crystals-based biosensors: an overview," Journal of Lightwave Technology **39**, 3871–3881 (2021).

[75] S. M. Lo, S. Hu, G. Gaur, Y. Kostoulas, S. M. Weiss, and P. M. Fauchet, "Photonic crystal microring resonator for label-free biosensing," Optics Express **25**, 7046–7054 (2017).

[76] A. Albertoni, "Long wave infrared metamaterials and nano-materials design, simulation, and laboratory test for target camouflage in the defence application," in "Electro-Optical and Infrared Systems: Technology and Applications VIII," , vol. 8185 (SPIE, 2011), vol. 8185, pp. 66–85.

[77] Y. Li, X. Zhou, Q. Yang, Y. Li, W. Li, H. Li, S. Chen, M. Li, and Y. Song, "Patterned photonic crystals for hiding information," Journal of Materials Chemistry C **5**, 4621–4628 (2017).

[78] S. Zhang, Z. Gu, and J.-N. Ding, "Photonic crystals for photon management in solar cells," Printable Solar Cells pp. 513–548 (2017).

[79] D. Zhou and R. Biswas, "Photonic crystal enhanced light-trapping in thin film solar cells," Journal of Applied Physics **103**, 093102 (2008).

[80] D.-H. Ko, J. R. Tumbleston, L. Zhang, S. Williams, J. M. DeSimone, R. Lopez, and E. T. Samulski, "Photonic crystal geometry for organic solar cells," Nano Letters **9**, 2742–2746 (2009).

[81] P. Bermel, C. Luo, L. Zeng, L. C. Kimerling, and J. D. Joannopoulos, "Improving thin-film crystalline silicon solar cell efficiencies with photonic crystals," Optics Express **15**, 16986–17000 (2007).

[82] A. Chutinan, N. P. Kherani, and S. Zukotynski, "High-efficiency photonic crystal solar cell architecture," Optics Express **17**, 8871–8878 (2009).

[83] W. Liu, H. Ma, and A. Walsh, "Advance in photonic crystal solar cells," Renewable and Sustainable Energy Reviews **116**, 109436 (2019).

[84] H. C. Bauser, C. R. Bukowsky, M. Phelan, W. Weigand, D. R. Needell, Z. C. Holman, and H. A. Atwater, "Photonic crystal waveguides for $> 90\%$ light trapping efficiency in luminescent solar concentrators," ACS Photonics **7**, 2122–2131 (2020).

[85] L. Zhu, A. P. Raman, and S. Fan, "Radiative cooling of solar absorbers using a visibly transparent photonic crystal thermal blackbody," Proceedings of the National Academy of Sciences **112**, 12282–12287 (2015).

[86] R. Meade, A. Rappe, K. Brommer, and J. Joannopoulos, "Nature of the photonic band gap: some insights from a field analysis," JOSA B **10**, 328–332 (1993).

[87] V. Likodimos, "Photonic crystal-assisted visible light activated tio2 photocatalysis," Applied Catalysis B: Environmental **230**, 269–303 (2018).

[88] L. A. Woldering, A. P. Mosk, and W. L. Vos, "Design of a three-dimensional photonic band gap cavity in a diamondlike inverse woodpile photonic crystal," Physical Review B **90**, 115140 (2014).

[89] T. Baba, K. Inoshita, H. Tanaka, J. Yonekura, M. Ariga, A. Matsutani, T. Miyamoto, F. Koyama, and K. Iga, "Strong enhancement of light extraction efficiency in GaInAsP 2-D-arranged microcolumns," Journal of Lightwave Technology **17**, 2113 (1999).

[90] M. V. Rybin, K. B. Samusev, S. Y. Lukashenko, Y. S. Kivshar, and M. F. Limonov, "Transition from two-dimensional photonic crystals to dielectric metasurfaces in the optical diffraction with a fine structure," Scientific Reports **6**, 30773 (2016).

[91] T. A. Birks, J. C. Knight, and P. S. J. Russell, "Endlessly single-mode photonic crystal fiber," Optics Letters **22**, 961–963 (1997).

[92] M. Yoshida, M. De Zoysa, K. Ishizaki, Y. Tanaka, M. Kawasaki, R. Hatsuda, B. Song, J. Gelleta, and S. Noda, "Double-lattice photonic-crystal resonators enabling high-brightness semiconductor lasers with symmetric narrow-divergence beams," Nature Materials **18**, 121–128 (2019).

[93] Y. Chan, C. T. Chan, and Z. Liu, "Photonic band gaps in two dimensional photonic quasicrystals," Physical Review Letters **80**, 956 (1998).

[94] M. Florescu, S. Torquato, and P. J. Steinhardt, "Complete band gaps in two-dimensional photonic quasicrystals," Physical Review B **80**, 155112 (2009).

[95] T. Amoah and M. Florescu, "High-Q optical cavities in hyperuniform disordered materials," Physical Review B **91**, 020201 (2015).

[96] F. Riboli, N. Caselli, S. Vignolini, F. Intonti, K. Vynck, P. Barthelemy, A. Gerardino, L. Balet, L. H. Li, A. Fiore, M. Gurioli, and D. S. Wiersma, "Engineering of light confinement in strongly scattering disordered media," .

[97] E. Kuramochi, M. Notomi, S. Mitsugi, A. Shinya, T. Tanabe, and T. Watanabe, "Ultrahigh-Q photonic crystal nanocavities realized by the local width modulation of a line defect," Applied Physics Letters **88**, 041112 (2006).

[98] V. Kuzmiak and A. A. Maradudin, "Localized defect modes in a two-dimensional triangular photonic crystal," Physical Review B **57**, 15242 (1998).

[99] M. Minkov and V. Savona, "Automated optimization of photonic crystal slab cavities," Scientific Reports **4**, 1–8 (2014).

[100] U. P. Dharanipathy, M. Minkov, M. Tonin, V. Savona, and R. Houdré, "High-Q silicon photonic crystal cavity for enhanced optical nonlinearities," Applied Physics Letters **105**, 101101 (2014).

[101] R. Abe, T. Takeda, R. Shiratori, S. Shirakawa, S. Saito, and T. Baba, "Optimization of an H0 photonic crystal nanocavity using machine learning," Optics Letters **45**, 319–322 (2020).

[102] S. Hu and S. M. Weiss, "Design of photonic crystal cavities for extreme light concentration," ACS Photonics **3**, 1647–1653 (2016).

[103] G.-J. Tang, X.-T. He, F.-L. Shi, J.-W. Liu, X.-D. Chen, and J.-W. Dong, "Topological photonic crystals: Physics, designs, and applications," Laser & Photonics Reviews **16**, 2100300 (2022).

[104] T. Wu, M. Gurioli, and P. Lalanne, "Nanoscale light confinement: the Q's and V's," ACS Photonics **8**, 1522–1538 (2021).

[105] T. Asano and S. Noda, "Photonic crystal devices in silicon photonics," Pro. IEEE **106**, 2183–2195 (2018).

[106] "Chapter 5," (this thesis).

[107] L. Jin, L. Di Lauro, A. Pasquazi, M. Peccianti, D. J. Moss, R. Morandotti, B. E. Little, and S. T. Chu, "Optical multi-stability in a nonlinear high-order microring resonator filter," APL Photonics **5**, 056106 (2020).

[108] Y. Dumeige and P. Féron, "Stability and time-domain analysis of the dispersive tristability in microresonators under modal coupling," Physical Review A **84**, 043847 (2011).

[109] N. Jebali, L. Bodiou, J. Charrier, A. Armaroli, and Y. Dumeige, "Combining FDTD and coupled-mode theory for self-pulsing modeling in coupled nonlinear microring resonators," JOSA B **37**, 2557–2563 (2020).

[110] D. Gray, R. Hamerly, M. Namdari, M.-T. Cătuneanu, K. Jamshidi, N. Bogdanowicz, and H. Mabuchi, "Thermo-optic multistability and relaxation in silicon microring resonators with lateral diodes," Physical Review Applied **14**, 024073 (2020).

[111] I. A. Temnykh, N. F. Baril, Z. Liu, J. V. Badding, and V. Gopalan, "Optical multistability in a silicon-core silica-cladding fiber," Optics Express **18**, 5305–5313 (2010).

[112] S. Rodriguez, A. Amo, I. Sagnes, L. Le Gratiet, E. Galopin, A. Lemaître, and J. Bloch, "Interaction-induced hopping phase in driven-dissipative coupled photonic microcavities," Nature Communications **7**, 1–6 (2016).

[113] E. Kuramochi, K. Nozaki, A. Shinya, K. Takeda, T. Sato, S. Matsuo, H. Taniyama, H. Sumikura, and M. Notomi, "Large-scale integration of wavelength-addressable all-optical memories on a photonic crystal chip," Nature Photonics **8**, 474 – 481 (2014).

[114] W. R. McGehee, T. Michels, V. Aksyuk, and J. J. McClelland, "Two-dimensional imaging and modification of nanophotonic resonator modes using a focused ion beam," Optica **4**, 1444–1450 (2017).

[115] A. Yacomotti, F. Raineri, G. Vecchi, P. Monnier, R. Raj, A. Levenson, B. Ben Bakir, C. Seassal, X. Letartre, P. Viktorovitch *et al.*, "All-optical bistable band-edge Bloch modes in a two-dimensional photonic crystal," Applied Physics Letters **88**, 231107 (2006).

[116] A. M. Yacomotti, P. Monnier, F. Raineri, B. B. Bakir, C. Seassal, R. Raj, and J. A. Levenson, "Fast thermo-optical excitability in a two-dimensional photonic crystal," Physical Review Letters **97**, 143904 (2006).

[117] B. Chen, R. Bruck, D. Traviss, A. Z. Khokhar, S. Reynolds, D. J. Thomson, G. Z. Mashanovich, G. T. Reed, and O. L. Muskens, "Hybrid photon–plasmon coupling and ultrafast control of nanoantennas on a silicon photonic chip," Nano Letters **18**, 610–617 (2018).

[118] K. Vynck, N. J. Dinsdale, B. Chen, R. Bruck, A. Z. Khokhar, S. A. Reynolds, L. Crudgington, D. J. Thomson, G. T. Reed, P. Lalanne *et al.*, "Ultrafast perturbation maps as a quantitative tool for testing of multi-port photonic devices," Nature Communications **9**, 1–10 (2018).

[119] S. Sokolov, J. Lian, E. Yüce, S. Combrié, A. D. Rossi, and A. P. Mosk, "Tuning out disorder-induced localization in nanophotonic cavity arrays," Optics Express **25**, 4598–4606 (2017).

[120] E. Yüce, J. Lian, S. Sokolov, J. Bertolotti, S. Combrié, G. Lehoucq, A. De Rossi, and A. P. Mosk, "Adaptive control of necklace states in a photonic crystal waveguide," ACS Photonics **5**, 3984–3988 (2018).

[121] C. L. Panuski, I. Christen, M. Minkov, C. J. Brabec, S. Trajtenberg-Mills, A. D. Griffiths, J. J. McKendry, G. L. Leake, D. J. Coleman, C. Tran, J. St Louis, J. Mucci, C. Horvath, J. N. Westwood-Bachman, S. F. Preble, M. D. Dawson, M. J. Strain, M. L. Fanto, and D. R. Englund, "A full degree-of-freedom spatiotemporal light modulator," Nature Photonics **16**, 834–842 (2022).

[122] G. Marty, S. Combrié, F. Raineri, and A. De Rossi, "Photonic crystal optical parametric oscillator," Nature Photonics **15**, 53–58 (2021).

[123] G. Marty, "Four wave mixing in III–V semiconductor photonic crystal cavities," Ph.D. thesis, Université Paris-Saclay (2021).

[124] G. Marty, S. Combrié, A. De Rossi, and F. Raineri, "Hybrid InGaP nanobeam on silicon photonics for efficient four wave mixing," APL Photonics **4**, 120801 (2019).

[125] M. Soljačić and J. D. Joannopoulos, "Enhancement of nonlinear effects using photonic crystals," Nature Materials **3**, 211–219 (2004).

[126] J. Sheng, U. Khadka, and M. Xiao, "Realization of all-optical multistate switching in an atomic coherent medium," Physical Review Letters **109**, 223906 (2012).

[127] Y.-N. Li, Y.-Y. Chen, R.-G. Wan, and H.-W. Yan, "Dynamical switching and memory via incoherent pump assisted optical bistability," Physics Letters A **383**, 2248–2254 (2019).

[128] S. Combrié, S. Bansropun, M. Lecomte, O. Parillaud, S. Cassette, H. Benisty, and J. Nagle, "Optimization of an inductively coupled plasma etching process of GaInP/GaAs based material for photonic band gap applications," Journal of Vacuum Science and Technology B **23**, 1521 (2005).

[129] S. Combrié, Q. V. Tran, A. De Rossi, C. Husko, and P. Colman, "High quality GaInP nonlinear photonic crystals with minimized nonlinear absorption," Applied Physics Letters **95**, 221108 (2009).

[130] E. F. Schubert, *Light-emitting diodes* (E. Fred Schubert, 2018).

[131] Y. Ueno, V. Ricci, and G. I. Stegeman, "Second-order susceptibility of ga 0.5 in 0.5 p crystals at 1.5 μm and their feasibility for waveguide quasi-phase matching," JOSA B **14**, 1428–1436 (1997).

[132] I. Cestier, V. Eckhouse, G. Eisenstein, S. Combrié, P. Colman, and A. De Rossi, "Resonance enhanced large third order nonlinear optical response in slow light GaInP photonic-crystal waveguides," Optics Express **18**, 5746–5753 (2010).

[133] P. J. Harding, T. G. Euser, and W. L. Vos, "Identification of competing ultrafast all-optical switching mechanisms in Si woodpile photonic crystals," JOSA B **26**, 610–619 (2009).

[134] E. Yüce, G. Ctistis, J. Claudon, E. Dupuy, K. J. Boller, J.-M. Gérard, and W. L. Vos, "Competition between electronic kerr and free-carrier effects in an ultimate-fast optically switched semiconductor microcavity," JOSA B **29**, 2630–2642 (2012).

[135] R. Bruck, K. Vynck, P. Lalanne, B. Mills, D. J. Thomson, G. Z. Mashanovich, G. T. Reed, and O. L. Muskens, "All-optical spatial light modulator for reconfigurable silicon photonic circuits," Optica **3**, 396–402 (2016).

[136] R. Bruck, B. Mills, B. Troia, D. J. Thomson, F. Y. Gardes, Y. Hu, G. Z. Mashanovich, V. M. Passaro, G. T. Reed, and O. L. Muskens, "Device-level characterization of the flow of light in integrated photonic circuits using ultrafast photomodulation spectroscopy," Nature Photonics **9**, 54 (2015).

[137] G. Ctistis, E. Yuce, A. Hartsuiker, J. Claudon, M. Bazin, J.-M. Gérard, and W. L. Vos, "Ultimate fast optical switching of a planar microcavity in the telecom wavelength range," Applied Physics Letters **98**, 161114 (2011).

[138] "Chapter 3," (this thesis).

[139] S. Iadanza, M. Clementi, C. Hu, S. A. Schulz, D. Gerace, M. Galli, and L. O'Faolain, "Model of thermo-optic nonlinear dynamics of photonic crystal cavities," Physical Review B **102**, 245404 (2020).

[140] J. Lian, S. Sokolov, E. Yüce, S. Combrié, A. De Rossi, and A. P. Mosk, "Measurement of the profiles of disorder-induced localized resonances in photonic crystal waveguides by local tuning," Optics Express **24**, 21939–21947 (2016).

[141] S. S. Li, "Excess carrier phenomenon in semiconductors," in "Semiconductor physical electronics," (Springer, 2006), pp. 246–283.

[142] K. W. Park, C. Y. Park, S. Ravindran, S. J. Kang, H. Y. Hwang, Y. D. Jho, Y. R. Jo, B. J. Kim, and Y. T. Lee, "Enhancement of minority carrier lifetime of GaInP with lateral composition modulation structure grown by molecular beam epitaxy," Journal of Applied Physics **116**, 043516 (2014).

[143] S. Sokolov, J. Lian, S. Combrié, A. D. Rossi, and A. P. Mosk, "Measurement of the linear thermo-optical coefficient of $Ga_{0.51}In_{0.49}P$ using photonic crystal nanocavities," Applied Optics **56**, 3219–3222 (2017).

[144] D. W. Hahn and M. N. Özisik, *Heat Conduction* (John Wiley & Sons, Incorporated, Somerset, United States, 2012).

[145] H. R. Schwarz and J. Waldvogel, *Numerical analysis: a comprehensive introduction* (John Wiley & Sons Incorporated, 1989).

[146] R. Courant, K. Friedrichs, and H. Lewy, "Über die partiellen differenzengleichungen der mathematischen physik," Mathematische Annalen **100**, 32–74 (1928).

2

Experimental Apparatus

In this chapter we discuss the experimental apparatus. The high-Q nanoresonators on our PhC waveguide are known to have an optical nonlinear response that can be used to reach multiple stable and meta-stable states. Our apparatus is built to firstly probe the optical response of the PhC in the nonlinear regime, but also to have control over the optical state this multistable system is in.

To excite and probe stable and meta-stable states of the system, it is important to have full control over the input light wavelength and power, including wavelengths sweeps and intensity modulation, whilst keeping the PhC at constant temperature and protecting it against damage or degradation. The optical response of the PhC should be detected with low noise and sufficient bandwidth. Three ways of detection are possible: via the transmission signal, via the reflected signal or via the out-of-plane scattered leak light. Because we are interested in the nonlinear regime of the PhC we need sufficient input light power and incoupling efficiency. Positioning of the PhC should allow for excellent incoupling of light, as well as (selective) detection and focus alignment of an out-of-plane optical pump.

Many resonances are present in the spectrum of the PhC, thus in addition to spectral probing we need a means to spatially probe the PhC. We do this by locally heating the PhC with a low-power optical excitation beam. To that end, an out-of-plane pump beam that scans the PhC surface, making a mode map of the profiles to identify the modes. For the purpose of manipulating the optical state in the PhC we use the same optical excitation beam in a pulsed high-power experiment.

2.1 General Description

In Fig. 2.1 we show a schematic overview of our experimental apparatus, with at the center our PhC sample inside a nitrogen gas filled chamber. We discuss the PhC sample, its placement, alignment and preservation in the chamber in Section 2.2. The sample stage is the meeting point of three optical arms: the probing arm, the detection arm, and the optical pump arm. The probing arm starts at the near-infrared (NIR) laser and ends at the lensed fiber for light injection. It provides narrowband, precisely tunable NIR input light at a sufficient power to excite nonlinear phenomena in the photonic crystal resonators. The details are described in Section 2.3 below. At the detection arm out-of-plane scattered light (leakage from cavities) is collected with an microscope objective and detected on either a camera or photodiode. We treat the details of the detection scheme in Section 2.4. Pump light is provided by the blue laser. The optical pumping scheme, including the power modulation and spatial steering

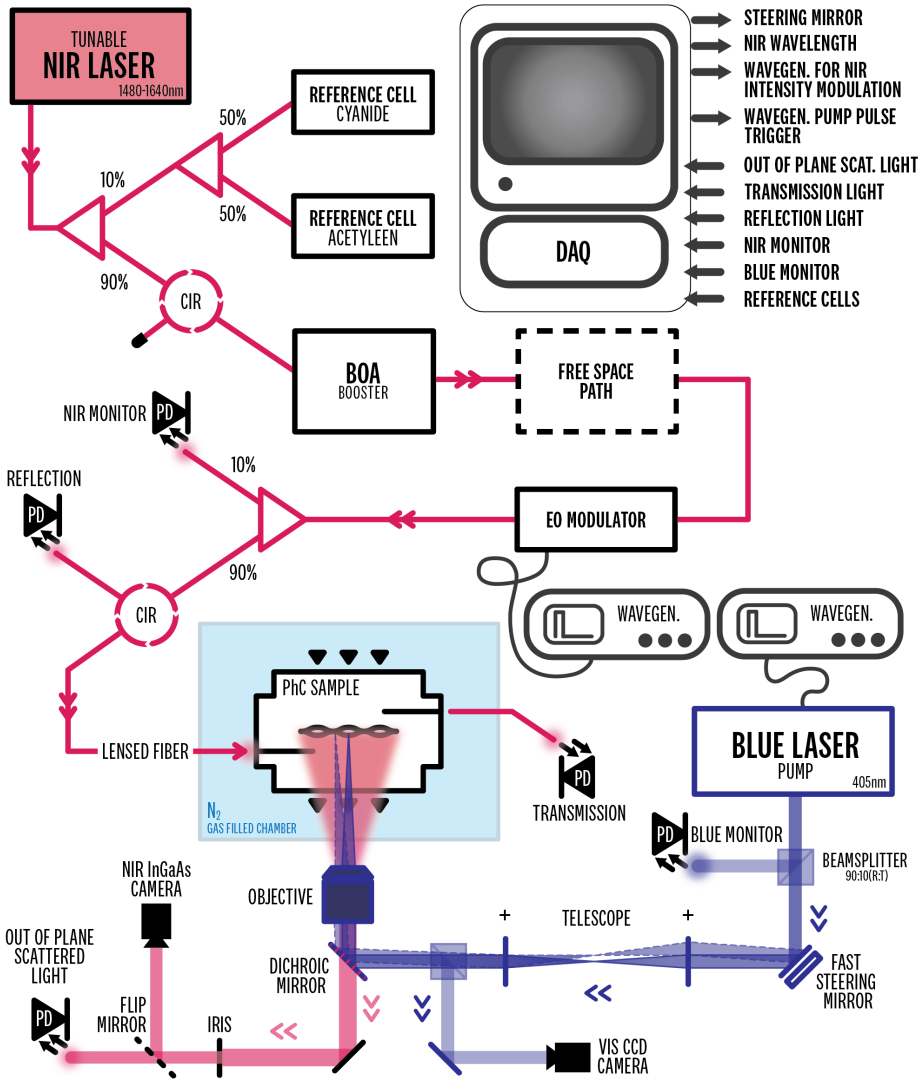

Figure 2.1: caption on next page

Figure 2.1: figure on previous page
Schematic overview of the experimental apparatus. The input light is provided by the NIR tunable laser and passes several 50/50 and 90/10 beamsplitters, circulators (CIR), a power booster (BOA), a free space optical path, an electro-optical modulator, photodiodes for monitoring and detection, and eventually a lensed fiber for the incoupling of light into the PhC. The PhC is placed inside a N_2-gas filled chamber. The pump light path involves a fast steering mirror, a 2-f telescope, an microscope objective and a VIS light camera. The out-of-plane detected light is collected with the objective, passing a dichroic mirror and is directed with a flip mirror to either an NIR InGaAs camera or cooled photodiode. Wavegenerators control the electro-optical modulator and blue laser power. Central control over the listed devices and acquisition of the PD signals happens at the lab PC connected to a digital acquisition system (DAQ).

possibilities, is described in Section 2.5. The data acquisition, central device control and measurement automation possibilities are explained in Section 2.6.

Our apparatus is based on that used for studies on PhCs in the linear regime[1–4]. We treat the most important differences at the start of Section 2.7, after which we put this experimental apparatus in context with similar research.

2.2 Sample Chamber

We have the PhC sample placed inside a sample chamber to keep it protected against oxidation and at constant temperature. Constant over-pressure of nitrogen gas in the chamber protects the PhC from oxidation and dust. A temperature controller (MercuryiTC) keeps the temperature of the PhC slightly elevated above room temperature at $T = 300$K for the experiment in Chapter 3 and $T = 305$K for the experiments in Chapter 4 and 5 with a precision of 1 mK. The sample is mounted on a nanometer-precision motorized stage (SmarAct MCS-3C), such that we have control over the PhC sample position for alignment of injection and extraction of light.

The PhC sample holds 27 waveguides, each of them with arrays of three mode-gap cavities, with between them small variation in inter-cavity distance and injection/extraction waveguide coupling. We select the waveguide we want to experiment on by translating the PhC with the precision stage. Input light (or probe light) is injected from the left with a lensed fiber. Transmission light is extracted from the right, also with a lensed fiber, and both outer ends of the waveguide have extended waveguides in the shape of a needle to improve injection/extraction[5] (see Fig. 2.2). Like the PhC sample, the lensed fibers are posi-

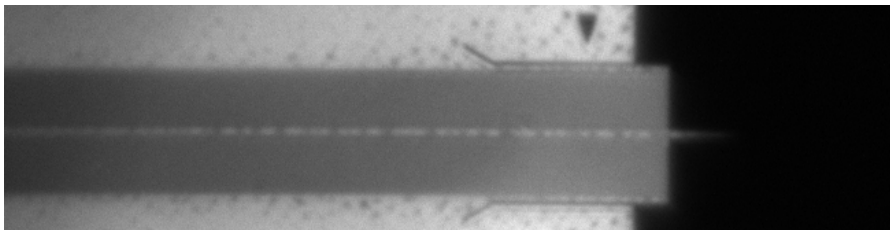

Figure 2.2: CCD photograph of the PhC waveguide and injection needle.

tioned on motorized stage holders (Thorlabs 3-axis NanoMax stage MAX302/M with Thorlabs stepper motor controller KST101). All stages have a positioning precision close to tens of nanometers, which allows for the alignment between fiber tip and injection needle with high precision and sufficient coupling efficiency.

The lensed fibers are polarization maintaining. They are aligned such that TE-like light is oriented parallel with the PhC membrane. For the extracted light an inline polarizing beamsplitter selects the TE light for the detection of transmission light.

2.3 Input Light Beam and Probing Details

Here we describe the input beam that we use to optically probe the PhC resonators. We want to perform experiments at constant wavelength as well as wavelength sweeps with predetermined sweep speed, resolution, and wavelength range. In addition, we need sufficient input light power, with a power range that covers both the linear and nonlinear optical regime, and also modulation capabilities.

A Santec tunable C-band laser provides the input light source with which we probe or drive the PhC (Santec TSL-710 in Chapter 3 and Chapter 4, Santec TSL-570 in Chapter 5). Polarization maintaining fibers guide the NIR light through a series of optical elements before reaching the injection lensed fiber, all fiber connections were made with narrow-key mating sleeves and where possible index-matching gel was used to suppress reflections. After exiting the NIR laser, a series of two inline beamsplitters take 10% of the power and divide the light over two reference gas cells filled with cyanide and acetylene. These gases have characteristic spectra with sharp fringes, which is used as a secondary external calibration method of the NIR wavelength. We should note that the internal wavelength calibration of the Santec laser is excellent with absolute precision of 1 pm for the TSL-710 and 3 pm for the TSL-570.

The main branch of the beamsplitter, with 90% of the power, is directed to a booster to enhance the power (Thorlabs S9FC1004 BOA) after passing a

circulator to prevent reflections reaching the NIR laser. We then pass a free space path, where fiber couplers lead the light through a combination of two half wave plates with a polarizing beamsplitter cube in between. This setup is used to shave off the maximum NIR power coming out of the booster (max. 32 mW) and prevent damage to the optics downstream. Additionally, an neutral-density (ND) filter wheel is used for manual switching between low NIR power and high NIR power.

An electro-optic intensity modulator is used to modulate the NIR power (10GHz EOSpace Lithium Niobate Modulator in Chapter 3, 15GHz Thorlabs LN82S in Chapters 4 and 5). A wave generator controls the modulator (30MHz Agilent 33521A, rise and fall time 10ns). It is used as stand-alone device to calibrate the modulator at fixed output power or continuously modulate with a certain waveform, or alternatively it is connected to the PC for triggered pulses. After the modulator 10% is sent to a photodiode to monitor the input modulation. The other 90% is going through a circulator that is connected to the injection fiber. We estimate a typical power range of 0.01-3.5 mW coming out of the lensed fiber. This circulator also takes reflected light from the PhC back to a photodiode for detection of the reflection signal.

2.4 Detection Scheme

Previously, it was shown that the out-of-plane scattered light has clean Lorentzian line shaped resonances, as opposed to in-plane signals detected via the lensed fibers that have Fano line shapes due to interference [3,6]. Thus, for the results presented in this thesis, we have based our data analysis on the out-of-plane scattering light intensity. Out-of-plane scattered light is less powerful than in-line light (guided through the waveguide into the fiber), thus we take special care to optimize the signal-to-noise ratio, such that the optical linear behavior at low probe powers is well within our detection capabilities.

We collect the out-of-plane scattered leak light with a 0.4 NA microscope objective that is mounted on a stage with two motorized actuators for alignment of the focus and translation (Thorlabs stepper motor actuator ZFS25B). After the objective, the light is passing through a dichroic mirror that reflects the blue 405 nm pump light, but transmits longer wavelengths. An iris in the conjugate plane removes background scattering before the light is detected on a cooled photodiode to suppress thermal noise (Hamamatsu G8605-21) that is kept at -20°C with a low dark current of 0.03 nA. The photodiode current is amplified with switchable bandwidth up to 500kHz and a low noise gain up to 10^9 V/A (Femto dlpca-200). A flip mirror switches the detection path to a NIR InGaAs camera for imaging of the PhC for visual aid with alignment of the lensed fiber or iris. Detection of the transmission and reflection signal is still implemented

in the apparatus and can be recorded when desirable. Both paths are provided with in-line amplifiers (Femto oe-200). For the transmission signal, an in-line polarizing beamsplitter selects the TE light for detection.

2.5 Pumping Scheme

We implement an all-optical spatial probe with which we scan the PhC surface and address specific positions for thermo-optical excitation. Power control enables low-power surface scans and high-power pump pulses. For these functionalities we have a visible light out-of-plane beam with its focus on the surface.

A 405 nm laser (OBIS 405LX) provides the pump light with a power range of 1-100 mW. For non cw measurements the power can be modulated with a wave generator (15 MHz Hewlett Packard 33120A). The power is generally kept well below 100 μW to prevent PhC damage. The pump light passes through a beamsplitter such that we can monitor the pump light on a photodiode. It then reaches a fast steering mirror (FSM, Newport FSM-300) controlled by the PC, a telescope, and then the microscope objective. This setup provides full control over the 2D positioning of a $\simeq$ 550nm pump focus on the PhC surface within the field of view of the objective. With a visible light (VIS) CCD camera (Allied Vision Guppy Pro F125B) we image the surface of the PhC for pump focus alignment and waveguide selection.

2.6 Data Acquisition, Device Control and Measurement Automation

Central control over the devices and lasers as well as measurement programming is needed to set up automated experiments that direct one, or a combination of, the following measurement types: wavelength sweeps, wavelength step scans, low-power cw pump grid scans, positional excitation pulse scans, input/pump power scans, or input light modulation measurements. At the same time, the effective bandwidth of the data acquisition (Photodetectors, Femto amplifier, DAQ) must be larger than bandwidth needed to measure time-resolved dynamics of the thermo-optical PhC system (timescales on the order of microseconds). Here we describe how the central control over the apparatus is set up, as well as the specifications of the data acquisition system.

Data acquisition by the lab-PC happens through a Data Acquisition System (DAQ, NI USB-6365), with a bandwidth of 1.25 MSamples/s divided over the number of channels used. We use two modes of data acquisition: TTL triggered acquisition by the NIR laser or continuous acquisition for a fixed amount of data

points and fixed bandwidth. In the case of triggered acquisition the NIR laser sends out a TTL trigger for a specified wavelength interval. This method is used to measure wavelength sweeps and is limited by the trigger bandwidth of the laser of 10 nm/s at 1 pm precision for the TSL-710 and 20 nm/s at 1 pm precision for the TSL-570. In the case of continuous acquisition the NIR laser is parked at a certain wavelength and a single internal or external trigger starts the measurement.

For the NIR power modulation measurements of Chapter 3 we require a high bandwidth, so we use a third data acquisition method. The NIR detected signal from the Femto amplifier is recorded on the the oscilloscope. The bandwidth is limited by the Femto amplifier at 400kHz.

The FSM position is controlled by the PC via an xy-voltage source, calibrated by the VIS camera imaging of the pump focus position for a 2D voltage scan and solving a position-voltage matrix.

The lab PC has an IEEE connection with the NIR laser and can write and read settings like wavelength, power, sweep speed, trigger resolution and more. The PC can adjust the power of the blue laser through the combined setup of a polarizing beamsplitter and half wave plate rotator. However, wave plate rotation is slow (on the order of a second), so for fast power modulation like microsecond pulses the PC is connected to the wave generator that controls the analogue power modulation of the blue laser.

A Python code provides automated measurements like steering mirror grid scans, pump pulse measurements at a range of parked NIR wavelengths, NIR wavelength sweeps, or a combination thereof. The software was custom made for the setup by Aquiles Carattino at University Utrecht, The Netherlands. It is best described as a program that sets up communication with the DAQ, NIR laser and cameras that then provides a modular software environment with a function library to script automated measurements. One can call functions from the library, including but not limited to functions that adjust laser power, laser wavelength, set sweep speed, send a voltage to the FSM controller, send a voltage pulse to trigger a wave generator, etc. We should note that switching acquisition settings between triggered acquisition and continuous acquisition is not possible. Data acquired by the DAQ together with the meta data are collected and saved in a hdf5 file. Metadata contains information like the date and time of the measurement, a copy of the script that runs the measurement, a copy of the current state of the software, a copy of the FSM calibration parameters, yml files containing information on the NIR laser settings like wavelength and power, data acquisition settings like acquisition rate and or number of datapoints collected.

2.7 Research Context

Here we discuss the unique experimental possibilities of the apparatus in the context of related research. In this thesis we make use of both the thermo-optical (TO) nonlinearity coming from self-absorption of high-power probe light, as well as the TO effect coming from absorption of low-power pump light providing a non-damaging programmable local heat source with a stable, tight pump focus. Additionally, pump light absorption in the presence of high-power probe light facilitates free carrier absorption (FCA) in the PhC material (explained in detail in Chapter 4 and 5). Deploying the combination of these three processes using the thermo-optic effect in 2D PhC resonators is what makes this apparatus unique.

In previous work in this group, this apparatus was optimized for the optical linear behavior at low probe powers. [1–4]. Therefore, out-of-plane injection with detection via the waveguide and lensed fiber was employed to improve signal to noise ratio. Resonances in the transmission and reflection signals have Fano lineshapes [3] and background fringes that make detection via the injection/extraction waveguide elaborate to interpret. In this research we inject light in-plane via the lensed fiber and waveguide, and detect the out-of-plane scattered light. The out-of-plane scattered light has clean Lorentzian lineshape resonances that are convenient for data analysis.

Additionally, earlier research focused on high-power pumping of several resonators at the same time [2], using a spatial light modulator (SLM) to shape the pump beam. Since high pump powers can damage the PhC, high-speed wavelength sweeps were needed. Also, considerable noise was added by the SLM in the pump beam. To reduce this noise we replaced the SLM with an FSM addressing resonators with a single pump focus and reducing the noise of the optical pump. We use a low-power pump combined with a relatively slow sweep speed or parked wavelength for the probe light, avoiding damage to the sample.

Marty and co-workers investigate a PhC membrane of the same semiconductor material as ours. They access the optical Kerr nonlinearity present in InGaP to create a PhC optical parametric oscillator (OPO) in a four wave mixing (FWM) experiment [7]. They use the TO effect to thermally tune the three frequencies involved using a projected incoherent optical pump source.

Clementi, Iadanza and co-workers [8,9] apply the TO effect in a silicon PhC membrane to invoke electromagnetically induced transparency. A single NIR laser source is split into a strong pump signal and weak probe signal with a cascade of acousto-optic modulators, creating two input wavelenghts detuned by a beating frequency. The transmitted light by the PhC is either amplified or suppressed depending on the beating frequency.

Bruck, Vynck and co-workers [10–12] use pulsed pump-probe methods to induce index shifts in a silicon layer device by FCA and shape the optical mode. Similar to our pumping techniques, they use out an out-of-plane visible light beam to manipulate the optical state, however, they deploy an SLM to shape the optical pump beam profile. Carrier densities of $\sim 10^{18-20}$ are needed for significant FCA, imposing the picosecond pulsed excitation to prevent damage to the sample, as opposed to our cw low probe power experiments (densities $\sim 10^{16}$).

Similarly, Panuski and co-workers [13] use a μLED arrays for all-optical switching by FCA in a silicon 2D PhC cavity array functioning as a spatial light modulator device.

Kuramochi, Notomi, Chen and co-workers have investigated many different PhC membrane designs, for instance deploying cavity arrays for wavelength-division multiplexing (WDM) using several NIR probing laser sources [14], very large-scale coupled cavity arrays [15], and injection locking-optical bistability based on input modulated switching between optical states [16]. Recently, Nakadai *et al.* demonstrated optical buffering experiments where they employ voltage pulses to control the optical state in the cavity [17], and Takata *et al.* demonstrated spontaneous emission at exceptional points by electrically pumped PhC coupled cavities [18].

2.8 Conclusion

In conclusion, we have presented the intended purpose of this experimental apparatus, how we optically probe the optical states in the PhC resonators, and treated the technical details to attain the desired capabilities. We discussed the probing, pumping and detection scheme, as well as the data acquisition system, the central device control, software and measurement automation. We related the apparatus to previous work in this group, and closed by placing the apparatus in context of related research to illustrate the unique aspects of our experiment.

2.9 References

[1] S. Sokolov, J. Lian, E. Yüce, S. Combrié, G. Lehoucq, A. De Rossi, and A. P. Mosk, "Local thermal resonance control of GaInP photonic crystal membrane cavities using ambient gas cooling," Applied Physics Letters **106**, 171113 (2015).

[2] S. Sokolov, J. Lian, E. Yüce, S. Combrié, A. D. Rossi, and A. P. Mosk, "Tuning out disorder-induced localization in nanophotonic cavity arrays," Optics Express **25**, 4598–4606 (2017).

[3] J. Lian, S. Sokolov, E. Yüce, S. Combrié, A. De Rossi, and A. P. Mosk, "Fano lines in the reflection spectrum of directly coupled systems of waveguides and cavities: Measurements, modeling, and manipulation of the fano asymmetry," Physical Review A **96**, 033812 (2017).

[4] J. Lian, S. Sokolov, E. Yüce, S. Combrié, A. De Rossi, and A. P. Mosk, "Measurement of the profiles of disorder-induced localized resonances in photonic crystal waveguides by local tuning," Optics Express **24**, 21939–21947 (2016).

[5] Q. V. Tran, S. Combrié, P. Colman, and A. De Rossi, "Photonic crystal membrane waveguides with low insertion losses," Applied Physics Letters **95**, 061105 (2009).

[6] S. Sokolov, "Dynamic tuning of photonic crystal nanocavities," Ph.D. thesis, University of Twente (2017).

[7] G. Marty, S. Combrié, F. Raineri, and A. De Rossi, "Photonic crystal optical parametric oscillator," Nature Photonics **15**, 53–58 (2021).

[8] M. Clementi, S. Iadanza, S. A. Schulz, G. Urbinati, D. Gerace, L. O'Faloain, and M. Galli, "Thermo-optically induced transparency on a photonic chip," Light: Science & Applications **10**, 1–10 (2021).

[9] S. Iadanza, M. Clementi, C. Hu, S. A. Schulz, D. Gerace, M. Galli, and L. O'Faolain, "Model of thermo-optic nonlinear dynamics of photonic crystal cavities," Physical Review B **102**, 245404 (2020).

[10] R. Bruck, K. Vynck, P. Lalanne, B. Mills, D. J. Thomson, G. Z. Mashanovich, G. T. Reed, and O. L. Muskens, "All-optical spatial light modulator for reconfigurable silicon photonic circuits," Optica **3**, 396–402 (2016).

[11] R. Bruck, B. Mills, B. Troia, D. J. Thomson, F. Y. Gardes, Y. Hu, G. Z. Mashanovich, V. M. Passaro, G. T. Reed, and O. L. Muskens, "Device-level characterization of the flow of light in integrated photonic circuits using ultrafast photomodulation spectroscopy," Nature Photonics **9**, 54 (2015).

[12] K. Vynck, N. J. Dinsdale, B. Chen, R. Bruck, A. Z. Khokhar, S. A. Reynolds, L. Crudgington, D. J. Thomson, G. T. Reed, P. Lalanne *et al.*, "Ultrafast perturbation maps as a quantitative tool for testing of multi-port photonic devices," Nature Communications **9**, 1–10 (2018).

[13] C. L. Panuski, I. Christen, M. Minkov, C. J. Brabec, S. Trajtenberg-Mills, A. D. Griffiths, J. J. McKendry, G. L. Leake, D. J. Coleman, C. Tran, J. St Louis, J. Mucci, C. Horvath, J. N. Westwood-Bachman, S. F. Preble,

M. D. Dawson, M. J. Strain, M. L. Fanto, and D. R. Englund, "A full degree-of-freedom spatiotemporal light modulator," Nature Photonics **16**, 834–842 (2022).

[14] E. Kuramochi, K. Nozaki, A. Shinya, K. Takeda, T. Sato, S. Matsuo, H. Taniyama, H. Sumikura, and M. Notomi, "Large-scale integration of wavelength-addressable all-optical memories on a photonic crystal chip," Nature Photonics **8**, 474 – 481 (2014).

[15] M. Notomi, E. Kuramochi, and T. Tanabe, "Large-scale arrays of ultrahigh-Q coupled nanocavities," Nature Photonics **2**, 741 – 747 (2008).

[16] C.-H. Chen, S. Matsuo, K. Nozaki, A. Shinya, T. Sato, Y. Kawaguchi, H. Sumikura, and M. Notomi, "All-optical memory based on injection-locking bistability in photonic crystal lasers," Optics Express **19**, 3387–3395 (2011).

[17] M. Nakadai, T. Asano, and S. Noda, "Electrically controlled on-demand photon transfer between high-Q photonic crystal nanocavities on a silicon chip," Nature Photonics **16**, 113–118 (2022).

[18] K. Takata, K. Nozaki, E. Kuramochi, S. Matsuo, K. Takeda, T. Fujii, S. Kita, A. Shinya, and M. Notomi, "Observing exceptional point degeneracy of radiation with electrically pumped photonic crystal coupled-nanocavity lasers," Optica **8**, 184–192 (2021).

3

Thermo-optical dynamics of a nonlinear GaInP photonic crystal nanocavity depend on the optical mode profile

Abstract

By step-modulating the optical input power we push the nonlinear resonance to jump between stable branches of its response curve, causing bistable switching. An overshoot of the intensity followed by a relaxation tail is observed upon bistable switching. In this way, the thermal relaxation of both the localized resonance and the delocalized resonance is measured. Significant difference in decay time is observed and related to the optical mode profile of the resonance. We reproduce the observed transient behavior with our thermo-optical model, implementing a non-instantaneous nonlinearity, and taking into account the optical mode profile of the resonance, as experimentally measured.

This chapter has been published as: Perrier, K., Greveling, S., Wouters, H., Rodriguez, S. R., Lehoucq, G., Combrié, S., de Rossi, A., Faez, S. and Mosk, A. P. OSA Continuum 3.7, 1879-1890 (2020)

3.1 Introduction

Resonators on photonic crystal (PhC) membranes are promising candidates for switchable and programmable optical communication devices as well as for fundamental physics exploration, as they combine high field enhancement with strong optical nonlinearity. Intentional waveguide defects on these membranes form nanocavities with a high-quality factor (high-Q) and small mode volume [1] that can be connected into coupled-resonator optical waveguides [2,3]. The optical nonlinearities in these PhCs are fundamental in the development of all-optical high-bandwidth functionalities like optical switches [4–9], optical memory [10], slow light [11–14] and quantum networks [15,16]. It is known that these nonlinearities can give rise to bistable behavior at powers of only a few μW [17,18], and the timescale of the dominating nonlinearity will ultimately limit the bandwidth of possible devices. The strong optical nonlinearity of PhC cavities can also be used to investigate the physics of dissipative phase transitions [19–22], and to probe the interplay of disorder and nonlinearity which is expected to strongly impact transport properties of cavity arrays [23,24].

Specifically in PhC membranes, the interplay between resonances and their 2D optical mode profiles can produce a strong thermo-optical nonlinearity that enables bistable switching. Measurements of the transient behavior brought about by bistable switching is usually controlled with an optical pump, either by pumping a second optical mode [25], or by using an out-of-plane optical pump pulse [26–28]. However, when there is absorption of the probe the optical mode itself becomes a source of heat, eliminating the need for an optical pump and enabling bistable switching with a single source of drive light.

In this chapter, we study the effect of the spatial mode profile on the thermo-optical response time of PhC resonances. Thermo-optical bistability induced by resonances have been observed before [29–31]. Yet, to our best knowledge, an investigation of different resonances involving their optical mode profiles and profile-specific dynamics has not been reported before. We measure two modes in a $Ga_{0.51}In_{0.49}P$ (GaInP) PhC slab by experimentally investigating the temporal behavior in the bistable regime of both a mode-gap cavity resonance and a delocalized waveguide resonance, demonstrating significantly different decay times. Additionally, we present a thermo-optical model that takes into account the obtained optical mode profile of the resonance. Although many models, formulating the resonator as a single temperature thermal object, have been shown throughout the literature [9,26,27,29,32,33], a model employing the measured mode profile of the resonance has not been demonstrated before to the best of our knowledge.

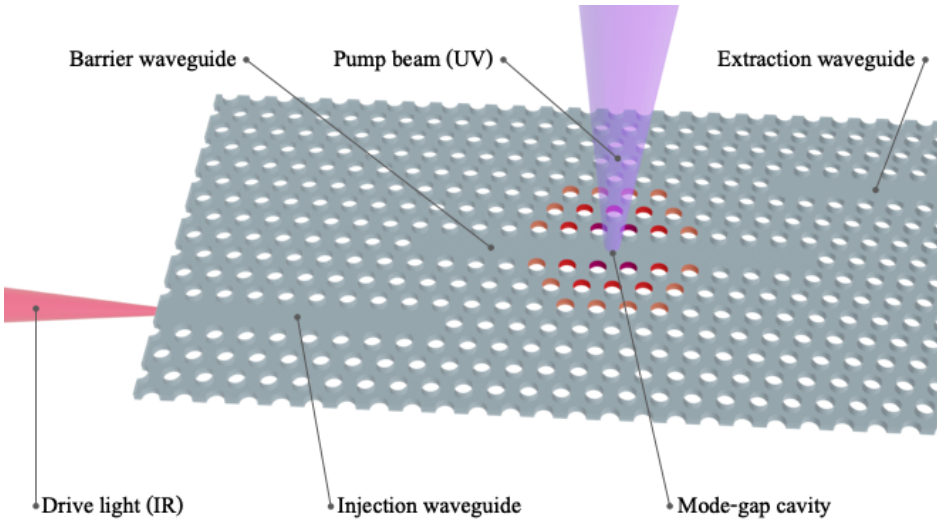

Figure 3.1: Schematic overview of the photonic crystal membrane. The mode-gap cavity consists of a broadened waveguide; the air holes lining the waveguide are shifted outwards from their lattice position with $0.0124\sqrt{3}a$, $\frac{2}{3} \times 0.0124\sqrt{3}a$ and $\frac{1}{3} \times 0.0124\sqrt{3}a$ for the first (purple), second (red) and last (orange) row respectively. The cavity is positioned on the barrier waveguide of width $W_0 = 0.98\sqrt{3}a$. Injection and extraction waveguides, both of width $W_1 = 1.1\sqrt{3}a$, are used to evanescently couple the infrared light in and out.

3.2 Characterization of the PhC

The air-suspended GaInP membrane, schematically depicted in Fig. 3.1, is 180 nm thick with air holes on a hexagonal lattice with a lattice constant of $a = 485$ nm. An injection waveguide is used to evanescently couple infrared light into the barrier waveguide on which the mode-gap cavity is positioned. The mode-gap cavity consists of a local width modulation of the barrier waveguide. In addition to the mode-gap cavity, high-Q delocalized modes spanning the barrier waveguide occur. The fabrication method is described in detail in Ref. [34]. The PhC is mounted in a nitrogen filled dust-free box to prevent oxidation.

The sample is driven with infrared light from a tunable CW laser, injected with a polarization maintaining lensed fiber. A 10 GHz bandwidth Mach-Zehnder electro-optic modulator (EOM) controls the input power. We measure the cavity response using the out-of-plane scattering light collected through a 0.4 NA

microscope objective and detect with an InGaAs photodiode (PD) (Hamamatsu G8605-21). An aperture in the conjugate plane removes background scattering. The signal is amplified (Femto dlpca-200) at a bandwidth of 7 kHz for the mode profiles (Fig. 3.2) and 1 kHz, 7 kHz, and 400 kHz for the spectral scans at low input power (Fig. 3.3a), high input power (Fig. 3.3b), and input power modulation measurements (Fig. 3.4, Fig. 3.5 and Fig. 3.6), respectively. An analog-to-digital converter board (NI USB-6356) acquires the spectral scans with a resolution of 1 pm. For the high-bandwidth power modulation measurements we use an oscilloscope at a sample rate of 2 MHz.

In addition to the infrared driving light, a second 405 nm diode laser (OBIS 405LX) provides out-of-plane pump light, focused on the sample by the objective. Due to absorption by the PhC membrane [35], the pump applies a local heat source. Using a fast scanning mirror we can spatially scan the PhC membrane with the pump and probe the thermo-optical profile of any PhC resonance [36]. With this method we identify the modes and measure their profile [37].

Thermo-optically Measured Mode Profile

In Figs. 3.2(a-b) we show the thermo-optically measured mode profiles of the two resonances of interest, detected via the out-of-plane scattered light. The corresponding images of the PhC membranes are shown beneath the mode profiles in Figs. 3.2(c-d). The mode profile is measured by scanning the barrier waveguide with the pump, positioning the pump spot in consecutive steps along the x-axis of the waveguide. For each pump position a wavelength scan is taken with the drive light. Due to the thermo-optical effect of the semiconductor material, local heating induces a redshift of the resonance wavelength when the thermal profile of the pump overlaps with the optical mode. In this way, plotting the wavelength redshift versus pump position reveals the mode profile.

In Fig. 3.2(a) a range of 12 μm is scanned in steps of 0.13 μm with a pump power of 7 μW. This shows a localized mode positioned at the center of the barrier waveguide with a FWHM of 3 μm. We thus identify this resonance as a a mode-gap resonance. Fig. 3.2(b) is measured over a wider pump range of 33 μm, taken with pump position steps of 0.26 μm and a pump power of 6 μW. This shows a profile that spans the barrier waveguide between the ends of the injection and extraction waveguide, with a maximum redshift over a 14-μm range. We therefore identify this resonance as a delocalized mode.

Spectral Scan

In Fig. 3.3 we show the spectral response of the mode-gap nanocavity measured via the out-of-plane scattered intensity. Spectral scans of the delocalized mode show a similar response and are therefore not depicted. Fig. 3.3(a) shows the

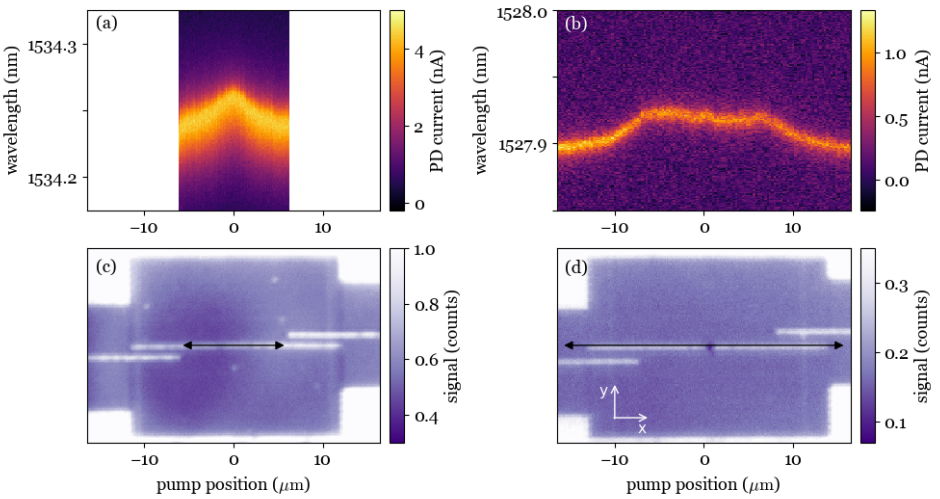

Figure 3.2: Optical mode profile of (a) the localized mode-gap resonance and (b) the delocalized waveguide resonance, obtained with wavelength scans while pumping with a weak pump spot over a range of pump positions on the waveguide. Pump positions are indicated by the black arrows on the image of (c) the PhC membrane holding the mode-gap resonance and (d) the PhC membrane holding the delocalized resonance. The membrane holding the mode-gap resonance has a barrier waveguide length of 24.7 μm, an overlap between barrier and injection/extraction waveguide of 6.1 μm in the x-direction and a distance between the waveguides of 1.7 μm in the y-direction. For the membrane holding the delocalized mode these dimensions are 28.1 μm, 6.3 μm and 1.3 μm respectively.

spectral response at low input power demonstrating the lineshape in the linear response regime. A Lorentzian lineshape fit yields the bare resonance $\lambda_0 = 1534.144$ nm and cold cavity linewidth $\Gamma = 30$ pm. For the delocalized mode we find a bare resonance of $\lambda_0 = 1527.736$ nm and linewidth of $\Gamma = 11$ pm in the same way.

In Fig. 3.3(b) we show the spectrum in the nonlinear regime with a bidirectional scan at high input power. The nonlinear behavior is characterized by a resonance peak that is skewed towards longer wavelengths, exhibiting a bistable response that depends on the direction of the scan. The forward scan follows the upper steady-state branch until, at large detuning, the system reaches the end of the branch and jumps down discontinuously, demarcating the edge of the bistable regime. For the backward scan the system follows the lower steady-state branch,

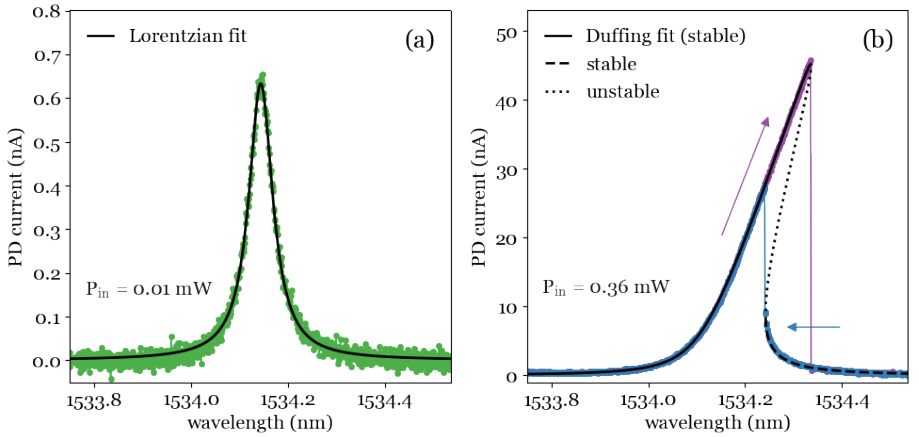

Figure 3.3: Spectral response of the mode-gap resonance in the (a) linear regime and (b) nonlinear regime as measured via the out-of-plane scattered light. In the nonlinear regime, the response depends on the wavelength scan direction, as indicated by the arrows for the forward (purple) and backward (blue) scans. For the nonlinear response we fit the Duffing equation to the upper steady-state branch (solid black curve) to find nonlinear parameter β and then plot the corresponding solutions for the lower steady-state branch (dashed) and the unstable branch (dotted). Scan rates were selected to obtain a good signal to noise ratio, with 0.5 nm/s for the low intensity linear regime and 1 nm/s for the high intensity nonlinear regime.

undercutting the upper branch, until it reaches the other edge of bistability and jumps back up. In this way a hysteresis loop that easily spans 100 pm is formed, demonstrating strong nonlinearity in the cavity.

To fit the spectral response in the nonlinear regime we solve the Duffing equation[38], describing a resonator with an instantaneous third-order nonlinearity, using the λ_0 found in Fig. 3.3(a). The equation will return both stable and unstable solutions that form a tilted peak with an upper and lower branch that are connected by the unstable branch. We fit the upper steady-state branch and use the result to plot the solutions for both the lower branch and the unstable branch. The fit yields the linewidth of the hot cavity, heated by absorption near resonance, $\Gamma_{\text{hot}} = 24$ pm, and a negative nonlinear parameter, which is in accordance with a redshift of the resonance in the bistable regime. We keep the hot cavity linewidth a free fit parameter because the temperature affects the resonance frequency, and indirectly through that, the mode profile and the losses to the injection and extraction waveguides[39,40]. For the delocalized mode we find

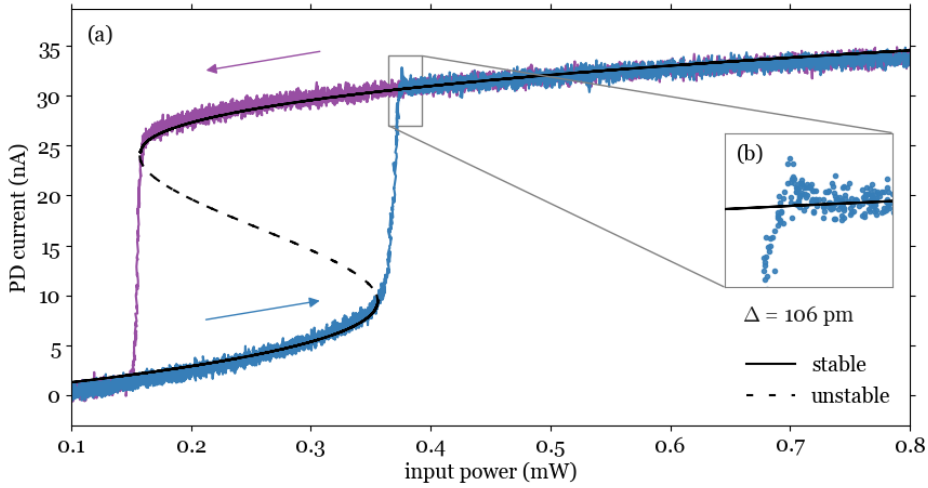

Figure 3.4: (a) Hysteresis loop in the nonlinear regime of the mode-gap resonance for fixed detuning $\Delta = 106$ pm and a 100 Hz triangle wave input power modulation. Arrows indicate the power scan direction. The out-of-plane scattered light is averaged over 100 modulation periods. Solutions for the Duffing equation are plotted for the both stable and unstable solutions as a guide to the eye. The inset (b) shows the details of an overshoot of the upper steady-state branch.

qualitatively the same nonlinear behavior with a negative nonlinear parameter, except here we have a slightly broader heated linewidth of $\Gamma_{\text{hot}} = 14$ pm.

Input Power Scan

To characterize the hysteresis behavior we measure out-of-plane scattering light versus input power. In Fig. 3.4(a) we scan the input power for the mode-gap resonance with a 100 Hz triangular wave while keeping the wavelength fixed at a positive detuning of $\Delta \equiv \lambda - \lambda_0 = 106$ pm. The measured out-of-plane scattering light is averaged over 100 modulation periods. The resulting cavity response shows the hysteresis loop: a region of bistability with discontinuous jumps at the ends of the upper and lower steady-state branch.

As a guide to the eye we plot the steady-state solutions of the Duffing equation versus input power, using the parameters found by the spectral fits of Section 3.2, using Γ for both the lower branch and unstable branch and Γ_{hot} for the upper branch. As the bare cavity resonance slightly drifts, we adjust λ_0 found

in Section 3.2 to correct for drift between and during scans, with a maximum correction of 42 pm. We attribute this slow shift to a thin water layer on the membrane, as explained elsewhere [41–44], and corresponds to the evaporation of a < 1 nm thick water layer. The S-shaped steady-state solutions of the Duffing equation are qualitatively consistent with the data – predicting both stable steady-state branches and the loop edges at the unstable turning points – except for the observation of an intensity overshoot.

Fig. 3.4(b) shows this intensity overshoot in detail. It is induced at the moment the system reaches the end of the lower steady-state branch and is forced into the upper steady-state branch. We perform a control measurement to rule out the overshoot being an artifact of the apparatus. With a step response measurement of the EOM-amplifier-oscilloscope chain a clean $10\% - 90\%$ rise time of $1.5\,\mu$s is observed, showing no overshoot. Since the Duffing equation describes an oscillator with instantaneous nonlinearity, it cannot describe the dynamics of the thermo-optical nonlinearity causing the overshoot. An adequate model is presented in Section 3.3.

We note that the parameters we chose for our experiments are such that our hysteresis measurements can be compared with a stationary solution [21]. Two considerations are made, the relevant timescale of the spectral and power scans are longer than the thermo-optical relaxation time. Furthermore, the scan timescale is short compared to the characteristic time at which fluctuations induce stochastic switching between bistable states. The input power scans of the delocalized mode result in similar hysteresis loops, with an even more pronounced overshoot of the upper steady-state branch.

Time-resolved Measurement of Thermo-optical Dynamics

In Fig. 3.5(a) we show the time-resolved relaxation of the intensity overshoot of the mode-gap resonance measured via the out-of-plane scattered power, averaged over 100 cycles. The overshoot is obtained by step-modulating the input power with a lead edge of 1.5 μs, as depicted in Fig. 3.5(b). In this way we drive the system across the hysteresis loop beyond the end of the lower steady-state branch and thus force a jump to the upper steady-state branch. We do this for six different detunings where each measurement is aligned at the peak intensity, showing the relaxation behavior right after the peak of the overshoot is independent of detuning. The emerging plateau preceding the overshoot for large detunings is the only part of the behavior that is affected by varying the detuning. The increasing duration of the plateau for larger detunings is behavior we have seen in computations with our model described in Section 3.3. However, a detailed discussion of the physics preceding the overshoot lies beyond the scope of this paper. Note that the timescale of the overshoot is too fast to be detected in the

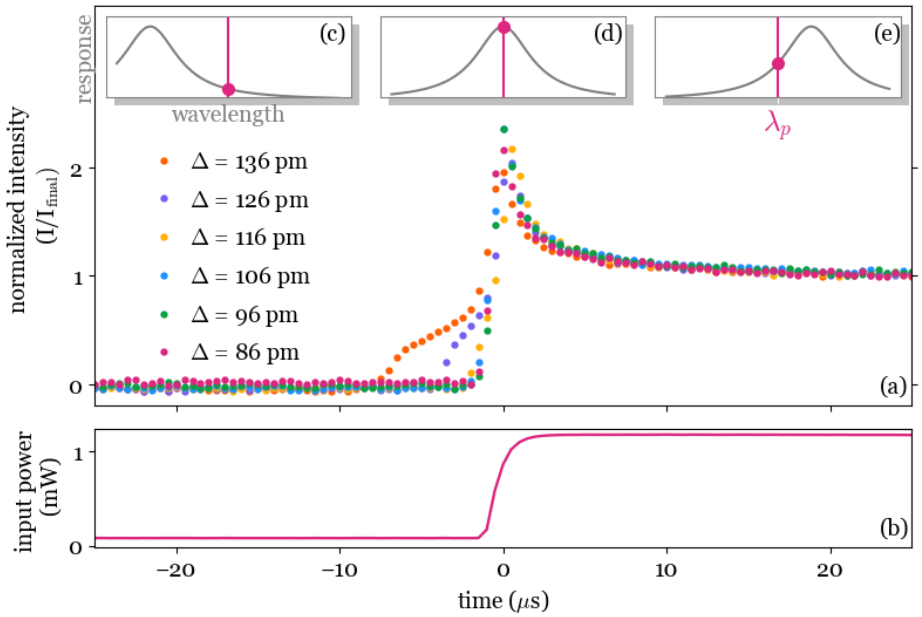

Figure 3.5: (a) Relaxation of the thermal overshoot at six different detunings measured in the out-of-plane scattered intensity. (b) Input power used to obtain the overshoot at $\Delta = 86$ pm. All other relaxation curves have time offsets between 0 and -8 μs such that the peak intensities are aligned. (c-e) Illustration of a typical instantaneous cavity response at the three different stages of the power step: (c) at the initial steady-state before the overshoot when we have low input power, (d) at the moment of jumping states when the input power steps up, (e) at the final steady-state when we have high input power.

spectral scans, and therefore could only be observed in the high-bandwidth power sweep measurements.

In Figs. 3.5(c-e) we illustrate the instantaneous cavity resonance corresponding to different moments in the power step to explain the physical mechanism of the intensity overshoot, as it helps to separate the resonant behavior of the cavity from its thermo-optical shift. At the start of the scan the cold cavity resonance lies on the blue side of the driving wavelength (Fig. 3.5(c)). When the driving power is increased, the resonance wavelength will shift towards the red due to absorption of the drive light. This *pulls* the system through resonance (Fig. 3.5(d)), momentarily maximizing the intensity inside the cavity. This is manifested in the sharp intensity peak. The resonance shifts further to the red

due to more absorption until the cavity reaches its steady state temperature. The hot cavity resonance is now on the red side of the driving wavelength, stabilized in the upper steady-state branch (Fig. 3.5(e)). A similar non-instantaneous response is expected when the system falls from the upper steady-state branch onto the lower one while sweeping in the opposite direction.

3.3 Thermo-optical Model

In this section we will focus on the dynamics of the transient. We consider the relaxation of the overshoot including the peak, meaning the stages of the power step depicted in Figs. 3.5(d,e). To describe the resonance shifts and the thermal diffusion in the PhC membrane, we solve a set of coupled equations relating the optical resonance to a modified heat equation. The electromagnetic response of the cavity is assumed to be on the timescale of the cavity photon lifetime of order 100 ps. Therefore, the electromagnetic response is effectively decoupled from the thermal diffusion in the PhC, which happens on a timescale of order 100 ns. Neglecting the z-dependence in the thin semiconductor slab, the optical energy density inside the cavity is

$$U_{\mathrm{opt}}(x,y,t) = \tau_{\mathrm{in}} P_{\mathrm{in}}(t) U_{\mathrm{mode}}(x,y) \frac{\Gamma^2}{\Gamma^2 + (\Delta - \delta_{\mathrm{th}}(t))^2}, \tag{3.1}$$

where τ_{in} is the input coupling efficiency, P_{in} is the input power of the drive light, U_{mode} is the energy density of the optical mode profile, and $\delta_{\mathrm{th}}(t)$ is the thermal resonance shift that causes a dynamic detuning.

The energy density of the optical mode is normalized over the xy-plane of the membrane

$$\int U_{\mathrm{mode}}(x,y)dxdy = 1. \tag{3.2}$$

For our experimental conditions the resonance frequency shifts linearly with temperature[45]. The thermal resonance shift is then given by

$$\delta_{\mathrm{th}}(t) = \int \eta U_{\mathrm{mode}}(x,y) T(x,y,t) dxdy, \tag{3.3}$$

where η is the thermo-optical coefficient of the semiconductor material and T the temperature profile. We consider the two cooling processes that dissipate heat into the substrate: in-plane heat dissipation that eventually reaches the bridge connecting the PhC with the substrate, and dissipation via the thin gas layer separating the membrane and the substrate beneath the PhC. Conductance through the gas on the top side of the membrane is neglected as it is likely to represent only a small fraction of the dissipation. Then, the dynamics of the temperature profile are described by the heat equation,

$$C_{2D}\frac{\partial T(x,y,t)}{\partial t} = -K_{2D}\nabla^2 T(x,y,t) - K_{gas}(T(x,y,t)-T_0) + \alpha\Gamma U_{opt}(x,y,t), \tag{3.4}$$

with the boundary condition that $T = T_0$ at the edges of the PhC membrane where there is a high thermal conductivity link with the substrate. Here, C_{2D} is the 2D specific heat of the PhC membrane, K_{2D} is the 2D thermal conductivity of the PhC membrane, K_{gas} is the thermal conductance of the gas layer between the PhC membrane and the substrate, and α the absorption fraction, *i.e.*, the probability a cavity photon is absorbed rather than scattered or leaked out of the cavity.

The 2D specific heat is given by

$$C_{2D} = h\phi\rho C_{sp}, \tag{3.5}$$

with h the slab thickness of the PhC membrane, ϕ the filling fraction of the PhC, ρ the density and C_{sp} the specific heat of the semiconductor material. The thermal conductivity K_{2D} is approximated as $h\phi\kappa$ where κ is the thermal conductivity of the semiconductor. Out-of-plane conductance through the gas layer is modeled by $K_{gas} = \kappa_{gas}/d_{gas}$, where d_{gas} is the distance between the membrane and the substrate. The contribution of the gas to the in-plane thermal conductance is neglected, as it is much smaller than the membrane conductance.

The system of equations, composed of Eq. (3.4), the heat equation which is a partial differential equation, and Eq. (3.1), the resonance condition, is solved using Euler's method [46] on an (x, y, t) grid. While not efficient, Euler integration is extremely robust as long as the step sizes fulfill the appropriate Courant-Friedrichs-Lewy condition [47].

3.4 Dynamics of Different Mode Profiles

In Fig. 3.6 we show the response of the two different modes shown in Fig. 3.2. Fig. 3.6(a) shows the measured relaxation behavior of the intensity overshoot of both modes in response to the step-modulated input power shown in Fig. 3.6(b). The delocalized mode has a longer 90%−10% decay time of $\tau_{90-10} = 10.1\pm1.8\,\mu$s compared to the mode-gap cavity with $\tau_{90-10} = 7.7\pm2.2\,\mu$s, where the 3σ error limits have been estimated by considering the spread of the decay times observed in different subsets of our data. In high-thermal conductivity platforms, like Si [25,48] or GaAs [49], the thermo-optics are typically much faster.

We compare the experimental data to our thermo-optical model and do a fit on both modes, using the appropriate measured mode profile U_{mode} in each case. The fitted model is shown in Fig. 3.6(a), using the specific heat of GaInP

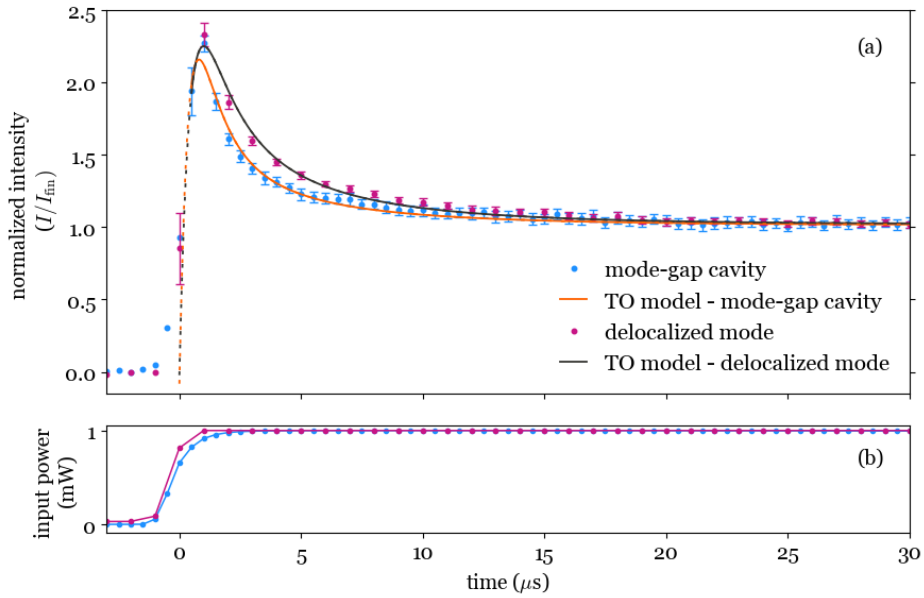

Figure 3.6: (a) The transient behavior upon bistable switching showing thermal relaxation of both the mode-gap resonance and the delocalized resonance, at small but positive detunings of 3.5Γ and 1Γ respectively. The response was measured via the out-of-plane scattered intensity, obtained by step-modulating the input power as shown in (b). Theoretical fits are plotted in solid lines with dashed curves in the extrapolation regions. Error bars are indicated for both data sets.

$C_{sp} = 310$ J/kgK [50], GaInP density $\rho = 4.81 \times 10^3$ kg/m^3 [51], a fill fraction of 0.714 for the membrane to account for the air holes, and an estimated value of $\alpha = 0.1$ for the absorption fraction. This absorption fraction is the highest value that is compatible with the sharpest observed resonances in these samples. We stress that the model is only sensitive to the product of the three parameters $\alpha\tau_{in}P_{in}$. Hence the fit does not depend on our estimate for α.

Since we focus on the dynamics starting around the peak of the overshoot, we start the fit one data point before the peak intensity. The detuning we fix at $\Delta = 0$ to assure we start modeling from the moment the drive light is at resonance with the mode (see Fig. 3.5(d)). We fit three parameters: the input energy $\tau_{in}P_{in}$ which is the electromagnetic energy inside the cavity on resonance, a scaling factor relating the intracavity power to the normalized detected out-of-plane scattering light, and an offset parameter accounting for the bias current of the photodiode. For the input energy we find 0.5 fJ for the mode-gap resonance and 1.5 fJ for the

delocalized mode. These values lie within reasonably expected input powers and incoupling rates. We conclude that the delocalized mode, existing in a thermally identical environment as the localized mode, shows significantly slower dynamics. Our model, using the measured mode profiles as input, reproduce the behavior accurately.

3.5 Discussion

To understand the difference in decay time we look at which cooling processes dominate. Both mode profiles have negligible overlap with the edges of the PhC, therefore we assume we are in the regime where virtually all of the cooling happens via the gas. This is confirmed by our model, as for both fitted curves more than 99.9% of the heat is dissipated via the gas layer. Hence the dimensions of the membrane and the distances to heat sinks such as the bridge to the substrate play no role here, unlike in the case of more highly thermally conductive materials like Si and GaAs crystals [17,26–28]. We note that the larger delocalized resonance has approximately two times the effective volume to surface ratio, and therefore a larger ratio of heat capacity to heat loss rate. This explains its longer relaxation time and slower dynamics.

3.6 Conclusion

In conclusion, we measured the response of two different modes in a PhC membrane by measuring the transient behavior upon bistable switching. We found that for the localized mode the thermal relaxation is 1.3 times faster than for a delocalized, elongated mode. The experimentally obtained thermo-optical dynamics are modeled using a heat equation that takes into account the optical mode profile of the resonance. This showed that, in the regime where heat dissipation predominantly happens through gas cooling via the PhC surface, the aspect ratio of the mode profile determines the resonance's thermo-optical relaxation time.

The influence of the mode profile on the temporal behavior is relevant also in other semiconductor materials, as the mode profile can be used to optimize optical switches for speed or stability. Targeted heat sinks customized to serve specific modes, designing resonances with different decay times, can serve a number of applications. Different time scales available in one PhC combined with nonlinearities of other origins, like charge-carrier density or the Kerr effect, open the doors to excitability [52] and constitutes to tunable all-optical delay lines.

3.7 References

[1] Y. Akahane, T. Asano, B.-S. Song, and S. Noda, "High-Q photonic nanocavity in a two-dimensional photonic crystal," Nature **425**, 944 (2003).

[2] M. Notomi, E. Kuramochi, and T. Tanabe, "Large-scale arrays of ultrahigh-Q coupled nanocavities," Nature Photonics **2**, 741 – 747 (2008).

[3] S. Sokolov, J. Lian, E. Yüce, S. Combrié, A. D. Rossi, and A. P. Mosk, "Tuning out disorder-induced localization in nanophotonic cavity arrays," Optics Express **25**, 4598–4606 (2017).

[4] V. R. Almeida, C. A. Barrios, R. R. Panepucci, and M. Lipson, "All-optical control of light on a silicon chip," Nature **431**, 1081 (2004).

[5] T. Tanabe, M. Notomi, S. Mitsugi, A. Shinya, and E. Kuramochi, "Fast bistable all-optical switch and memory on a silicon photonic crystal on-chip," Optics Letters **30**, 2575 – 2577 (2005).

[6] S. F. Preble, Q. Xu, B. S. Schmidt, and M. Lipson, "Ultrafast all-optical modulation on a silicon chip," Optics Letters **30**, 2891–2893 (2005).

[7] R. Bruck, B. Mills, B. Troia, D. J. Thomson, F. Y. Gardes, Y. Hu, G. Z. Mashanovich, V. M. Passaro, G. T. Reed, and O. L. Muskens, "Device-level characterization of the flow of light in integrated photonic circuits using ultrafast photomodulation spectroscopy," Nature Photonics **9**, 54 (2015).

[8] G. Ctistis, E. Yuce, A. Hartsuiker, J. Claudon, M. Bazin, J.-M. Gérard, and W. L. Vos, "Ultimate fast optical switching of a planar microcavity in the telecom wavelength range," Applied Physics Letters **98**, 161114 (2011).

[9] C. Qiu, Y. Yang, C. Li, Y. Wang, K. Wu, and J. Chen, "All-optical control of light on a graphene-on-silicon nitride chip using thermo-optic effect," Scientific Reports **7**, 1–7 (2017).

[10] E. Kuramochi, K. Nozaki, A. Shinya, K. Takeda, T. Sato, S. Matsuo, H. Taniyama, H. Sumikura, and M. Notomi, "Large-scale integration of wavelength-addressable all-optical memories on a photonic crystal chip," Nature Photonics **8**, 474 – 481 (2014).

[11] A. Melloni, A. Canciamilla, C. Ferrari, F. Morichetti, L. O'Faolain, T. Krauss, R. De La Rue, A. Samarelli, and M. Sorel, "Tunable delay lines in silicon photonics: coupled resonators and photonic crystals, a comparison," IEEE Photonics Journal **2**, 181–194 (2010).

[12] F. Morichetti, C. Ferrari, A. Canciamilla, and A. Melloni, "The first decade of coupled resonator optical waveguides: bringing slow light to applications," Laser Photonics Review **6**, 74–96 (2012).

[13] H. Gersen, T. J. Karle, R. J. P. Engelen, W. Bogaerts, J. P. Korterik, N. F. van Hulst, T. F. Krauss, and L. Kuipers, "Real-space observation of ultraslow light in photonic crystal waveguides," Physical Review Letters **94**, 073903 (2005).

[14] T. Baba, "Slow light in photonic crystals," Nature Photonics **2**, 465 (2008).

[15] P. Lodahl, "Quantum-dot based photonic quantum networks," Quantum Science and Technology **3**, 013001 (2017).

[16] M. Atatüre, D. Englund, N. Vamivakas, S.-Y. Lee, and J. Wrachtrup, "Material platforms for spin-based photonic quantum technologies," Nature Reviews Materials **3**, 38 (2018).

[17] E. Weidner, S. Combrié, A. de Rossi, N.-V.-Q. Tran, and S. Cassette, "Nonlinear and bistable behavior of an ultrahigh-Q GaAs photonic crystal nanocavity," Applied Physics Letters **90**, 101118 (2007).

[18] H. Altug and J. Vučković, "Two-dimensional coupled photonic crystal resonator arrays," Applied Physics Letters **84**, 161–163 (2004).

[19] M. Fitzpatrick, N. M. Sundaresan, A. C. Li, J. Koch, and A. A. Houck, "Observation of a dissipative phase transition in a one-dimensional circuit QED lattice," Physical Review X **7**, 011016 (2017).

[20] T. Fink, A. Schade, S. Höfling, C. Schneider, and A. Imamoglu, "Signatures of a dissipative phase transition in photon correlation measurements," Nature Phys. **14**, 365 (2018).

[21] S. R. K. Rodriguez, W. Casteels, F. Storme, N. Carlon Zambon, I. Sagnes, L. Le Gratiet, E. Galopin, A. Lemaître, A. Amo, C. Ciuti, and J. Bloch, "Probing a dissipative phase transition via dynamical optical hysteresis," Physical Review Letters **118**, 247402 (2017).

[22] A. Angerer, S. Putz, D. O. Krimer, T. Astner, M. Zens, R. Glattauer, K. Streltsov, W. J. Munro, K. Nemoto, S. Rotter, J. Schmiedmayer, and J. Majer, "Ultralong relaxation times in bistable hybrid quantum systems," Science Advances **3** (2017).

[23] K. Debnath, E. Mascarenhas, and V. Savona, "Nonequilibrium photonic transport and phase transition in an array of optical cavities," New Journal of Physics **19**, 115006 (2017).

[24] M. J. Hartmann, "Polariton crystallization in driven arrays of lossy nonlinear resonators," Physical Review Letters **104**, 113601 (2010).

[25] M. Notomi, A. Shinya, S. Mitsugi, G. Kira, E. Kuramochi, and T. Tanabe, "Optical bistable switching action of Si high-Q photonic-crystal nanocavities," Optics Express **13**, 2678–2687 (2005).

[26] A. M. Morsy, R. Biswas, and M. L. Povinelli, "High temperature, experimental thermal memory based on optical resonances in photonic crystal slabs," APL Photonics **4**, 010804 (2019).

[27] M. Brunstein, R. Braive, R. Hostein, A. Beveratos, I. Robert-Philip, I. Sagnes, T. J. Karle, A. M. Yacomotti, J. A. Levenson, V. Moreau, G. Tessier, and Y. D. Wilde, "Thermo-optical dynamics in an optically pumped photonic crystal nano-cavity," Optics Express **17**, 17118–17129 (2009).

[28] A. Arbabi and L. L. Goddard, "Dynamics of self-heating in microring resonators," IEEE Photonics Journal **4**, 1702–1711 (2012).

[29] T. Carmon, L. Yang, and K. J. Vahala, "Dynamical thermal behavior and thermal self-stability of microcavities," Optics Express **12**, 4742–4750 (2004).

[30] R. Biswas and M. L. Povinelli, "Photonic surfaces for designable nonlinear power shaping," Applied Physics Letters **106**, 061110 (2015).

[31] Y. Gao, W. Zhou, X. Sun, H. K. Tsang, and C. Shu, "Cavity-enhanced thermo-optic bistability and hysteresis in a graphene-on-Si_3N_4 ring resonator," Optics Letters **42**, 1950–1953 (2017).

[32] M.-K. Kim, I.-K. Hwang, S.-H. Kim, H.-J. Chang, and Y.-H. Lee, "All-optical bistable switching in curved microfiber-coupled photonic crystal resonators," Applied Physics Letters **90**, 161118 (2007).

[33] K. Ikeda, R. E. Saperstein, N. Alic, and Y. Fainman, "Thermal and Kerr nonlinear properties of plasma-deposited silicon nitride/silicon dioxide waveguides," Optics Express **16**, 12987–12994 (2008).

[34] S. Combrié, S. Bansropun, M. Lecomte, O. Parillaud, S. Cassette, H. Benisty, and J. Nagle, "Optimization of an inductively coupled plasma etching process of GaInP/GaAs based material for photonic band gap applications," Journal of Vacuum Science and Technology B **23**, 1521 (2005).

[35] S. Sokolov, J. Lian, E. Yüce, S. Combrié, G. Lehoucq, A. De Rossi, and A. P. Mosk, "Local thermal resonance control of GaInP photonic crystal membrane cavities using ambient gas cooling," Applied Physics Letters **106**, 171113 (2015).

[36] J. Lian, S. Sokolov, E. Yüce, S. Combrié, A. D. Rossi, and A. P. Mosk, "Measurement of the profiles of disorder-induced localized resonances in photonic crystal waveguides by local tuning," Optics Express **24**, 21939–21947 (2016).

[37] S. G. Johnson and J. D. Joannopoulos, *Photonic Crystals: The Road from Theory to Practice* (Springer Science & Business Media, 2001).

[38] Y. Ueda, "Random phenomena resulting from non-linearity in the system described by duffing's equation," International Journal of Non-Linear Mechanics **20**, 481 – 491 (1985).

[39] J. Lian, S. Sokolov, E. Yüce, S. Combrié, A. De Rossi, and A. P. Mosk, "Dispersion of coupled mode-gap cavities," Optics Letters **40**, 4488–4491 (2015).

[40] R. Faggiani, A. Baron, X. Zang, L. Lalouat, S. A. Schulz, B. O'regan, K. Vynck, B. Cluzel, F. De Fornel, T. F. Krauss, and P. Lalanne, "Lower bound for the spatial extent of localized modes in photonic-crystal waveguides with small random imperfections," Scientific Reports **6**, 27037 (2016).

[41] D. B. Asay and S. H. Kim, "Evolution of the adsorbed water layer structure on silicon oxide at room temperature," The Journal of Physical Chemistry B **109**, 16760–16763 (2005).

[42] C. J. Chen, J. Zheng, T. Gu, J. F. McMillan, M. Yu, G.-Q. Lo, D.-L. Kwong, and C. W. Wong, "Selective tuning of high-Q silicon photonic crystal nanocavities via laser-assisted local oxidation," Optics Express **19**, 12480–12489 (2011).

[43] S. Sokolov, "Dynamic tuning of photonic crystal nanocavities," Ph.D. thesis, University of Twente (2017).

[44] X. Zhang and S. Ptasinska, "Dissociative adsorption of water on an H2O/GaAs (100) interface: in situ near-ambient pressure XPS studies," The Journal of Physical Chemistry C **118**, 4259–4266 (2014).

[45] S. Sokolov, J. Lian, S. Combrié, A. D. Rossi, and A. P. Mosk, "Measurement of the linear thermo-optical coefficient of $Ga_{0.51}In_{0.49}P$ using photonic crystal nanocavities," Applied Optics **56**, 3219–3222 (2017).

[46] H. R. Schwarz and J. Waldvogel, *Numerical analysis: a comprehensive introduction* (John Wiley & Sons Incorporated, 1989).

[47] R. Courant, K. Friedrichs, and H. Lewy, "Über die partiellen differenzengleichungen der mathematischen physik," Mathematische Annalen **100**, 32–74 (1928).

[48] H. Yu, H. Wang, Q. Xiong, J. Mei, Y. Zhang, Y. Wang, J. Lai, and C. Chen, "Photothermal switch of sub-microsecond response: a monolithic-integrated ring resonator and a metasurface absorber in silicon photonic crystals," Optics Letters **45**, 1806–1809 (2020).

[49] A. de Rossi, M. Lauritano, S. Combrié, Q. V. Tran, and C. Husko, "Interplay of plasma-induced and fast thermal nonlinearities in a GaAs-based photonic crystal nanocavity," Physical Review A **79**, 043818 (2009).

[50] U. Piesbergen, "The mean atomic heats of the III-V semiconductors, AlSb, GaAs, InP, GaSb, InAs, InSb and the atomic heats of the element Germanium between 12 and 273 K," Zeitschrift für Naturforschung **18a**, 141–147 (1963).

[51] M. Levinshtein, S. Rumyantsev, and M. Shur, *Handbook Series on Semiconductor Parameters* (World Scientific, 1996).

[52] A. M. Yacomotti, P. Monnier, F. Raineri, B. B. Bakir, C. Seassal, R. Raj, and J. A. Levenson, "Fast thermo-optical excitability in a two-dimensional photonic crystal," Physical Review Letters **97**, 143904 (2006).

4

Mode mapping photonic crystal nanocavities with $Q > 5 \times 10^5$ using free-carrier absorption

Abstract

We demonstrate a nonlinear photomodulation spectroscopy method to image the mode profile of a high-Q photonic crystal resonator (PhCR). This far-field imaging method is suitable for ultrahigh-Q cavities which we demonstrate on a Q = 619000 PhCR. We scan the PhCR surface with a 405 nm pump beam that modulates the refractive index by local thermal tuning, while probing the response of the resonance. We enhance resolution by probing at high power, using the thermo-optical nonlinearity of the PhCR. Spatial resolution of the thermo-optical effect is typically constrained by the broad thermal profile of the optical pump. Here we go beyond the thermal limit and show that we can approach the diffraction limit of the pump light. This is due to free carrier absorption that heats up the PhCR only when there is overlap between the optical pump spot and the optical mode profile. This is supported with a thermo-optical model that reproduces the high-resolution mode mapping. Results reveal that the observed enhanced resolution is reached for surprisingly low carrier density.

This chapter has been published as: K. Perrier, J. Baas, S. Greveling, G. Lehoucq, S. Combrié, A. De Rossi, S. Faez, A.P. Mosk, Phys. Rev. Appl. **18**, 034044, (2022)

4.1 Introduction

Photonic crystals (PhC) have raised interest from fundamental research [1,2], due to their enhanced light-matter interaction, but maybe even more so from the field of optical signal processing and computing [3,4].

They are prime candidates for optical integrated-circuit applications [5–7]. One reason for this is the possibility to design a defect on the PhC platform, creating a PhC resonator (PhCR) that typically has small mode volume and high quality factor (Q) [8] which maximizes the optical nonlinearity crucial to active photonic devices. Two-dimensional PhCs have been shown to be suitable for numerous applications such as fast optical switching [9,10], reconfigurable circuits [11], optical memories [12] and optical parametric oscillation [13].

Investigating the optical mode profile of the PhCR is vital in all of these functionalities. Calculations to predict resonator modes, like FDTD simulation, do not provide complete information as PhCR modes are very sensitive to nanometer-scale imperfections arising from the fabrication process [14]. Therefore, high resolution imaging of PhCR modes is a necessary step in research and application development [15].

A benchmark method to characterize optical mode profiles is near-field scanning optical microscopy (NSOM), where a probe tip scans the surface of the PhC. High spectral and deep subwavelength spatial resolution imaging have been demonstrated [15–17], as well as phase contrast imaging [18] and imaging of the electric and magnetic field [19,20]. However, the requirement of nanometer-distances between the tip and the sample can be demanding, and makes this method unsuitable for devices that are covered by a top cladding. Additionally, perturbation by an NSOM probe tip will affect the Q-factor of the cavity [21] making it challenging to image ultrahigh-Q cavities of order $10^4 - 10^6$ without destroying the confinement [22,23]. Mujumdar et al. successfully show NSOM mode mappings of a Q=55000 cavity while noting that the imaging profoundly influences the spectral characteristics of the mode [16]. They measure a Q-factor degradation close to a factor of 2, which is in line with the experiment of Lalouat et al. [23]. A perturbation of this order in the field of a $Q \sim 10^5$ cavity would mean the probe tip becomes the vastly dominating loss mechanism of the cavity, defeating the first-order perturbation principle.

Far-field imaging with photomodulation spectroscopy (PMS) techniques introduce an excitation beam normal to the PhC surface that scans the PhC surface and perturbs the optical field by modulating the refractive index. The highest spatial resolution is achieved with electron or ion beam PMS scans, either with pulsed [24–26] or continuous wave (cw) [27] sources probing the resonance. It should be noted that exposure to ion and electron beams lowers the Q of the resonator, and in fact this technique is also being purposefully used to irreversibly alter or

tune PhCs. Ultrafast PMS experiments were demonstrated by Bruck et al. [11,28], where the mode profile is imaged (and tuned) with an ultraviolet beam. Their method is rooted in a shift of the refractive index due to the Drude-like dispersion of a dense free-carrier plasma. This type of direct index perturbation needs a high concentration of carriers, and thus high-power optical excitation that can only be maintained on the picosecond scale due to risk of damage by photo-oxidation. The advantage then is the information in the time domain. However, picosecond-pulse excitation is not suitable for high-Q resonators, where the photon lifetime exceeds the lifetime of the carriers.

Thermal PMS is a method that is attractive due to its universality and ease of use. A pump beam is used to locally heat the PhC, and the resulting thermal change in refractive index leads to a shift in resonance frequency. Previously, our group has shown that with local thermal tuning the mode profile of a high-Q cavity can be recovered with a resolution that is limited by thermal diffusion [29,30] and Chapter 3. The effective spot size depends on the surrounding medium and it is generally much larger than the optical pump spot, so that even after deconvolution a moderate resolution remains [31].

In this chapter we demonstrate enhanced spatial resolution for nonlinear PMS (NPMS), *i.e.*, thermal photomodulation spectroscopy in the thermo-optical nonlinear regime. This is due to free-carrier absorption (FCA) that only occurs when the pump and probe fields spatially overlap. Using NPMS we measure the mode profile of ultrahigh-Q resonators without affecting the Q-factor.

Our method reaches excellent sensitivity even with continuous wave excitation, because the high-Q resonator enhances both the probe field that heats the free carriers and the sensitivity with which the resulting thermal index shift is detected. In this way, the nonlocal thermo-optical effect amplifies a very small and local absorption term. This intrinsic amplification mechanism, leveraging the high Q of the resonator, makes it possible to operate at a very low pump power, thus avoiding Q-factor degradation or other damage to the sample.

We reproduce our results using a thermo-optical (TO) model that takes into account all TO sources, showing that a significant effect already occurs when only a few hundred free carriers are present in the resonator.

4.2 Experiment and Theory

In Fig. 4.1 we show a schematic of the PhC, consisting of a 180 nm-thick $Ga_{0.51}In_{0.49}P$ slab with air holes in a triangular lattice and a lattice constant of $a = 485$ nm. The $Ga_{0.51}In_{0.49}P$ slab was grown epitaxially on GaAs and has a bandgap of 1.9eV [32] for TE polarized light. A nanocavity with a high Q and small mode volume was fabricated by waveguide width modulation, *i.e.*, a mode-gap cavity [33,34]. TE polarized NIR probe light from a C-band tunable laser

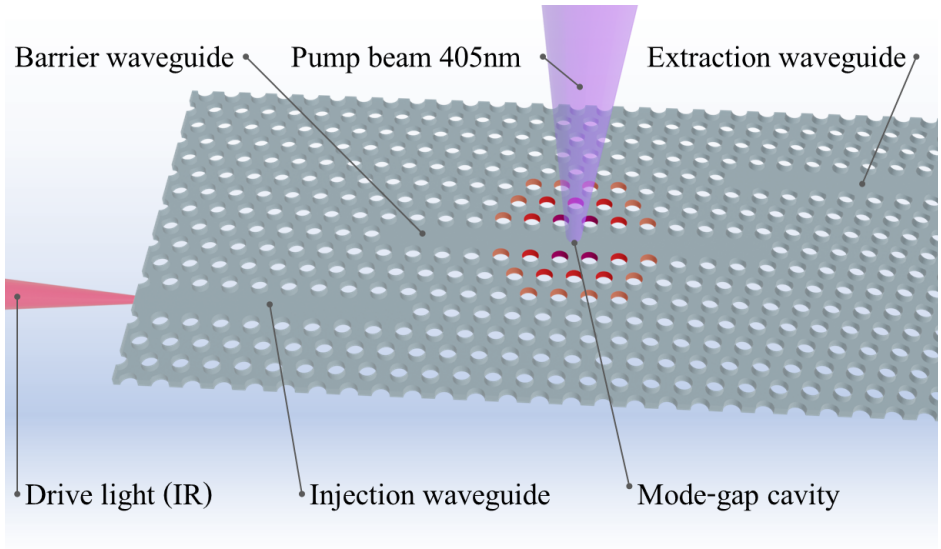

Figure 4.1: Schematic of the GaInP PhC membrane, with lattice constant a = 485 nm, air hole radius of 136 nm, and membrane thickness of 180 nm. The mode-gap cavity consists of a broadened waveguide: the air holes lining the waveguide are shifted outwards from their lattice position (see colored air holes). We coupled NIR light in from the side into the injection waveguide, after which it evanescently couples to the barrier waveguide.

with a linewidth of 40MHz and accuracy of ± 1 pm is coupled into the injection waveguide with a polarization maintaining lensed fiber, and it then evanescently couples through to the barrier waveguide. A small fraction of light inside the cavity is scattered out of plane and collected with a 0.4 NA objective onto a cooled photodiode, this signal of out of plane scattered light is proportionate to the intracavity energy. The same objective focuses out-of-plane pump light onto the sample. The 405 nm pump light is steered by a fast scanning mirror, providing a localized heat source with which we scan the surface of the membrane. With the scanning pump beam we spatially probe the response of the cavity by measuring the intracavity energy via the out of plane scattered NIR light.

In Fig. 4.2 we show a schematic of the three TO sources in the crystal. In Fig. 4.2(a) we depict the processes leading to direct probe light absorption in the PhC. Since the bulk bandgap exceeds the probe photon energy by more than a factor two this takes place via surface states, impurities, free electrons in the semiconductor, or a combination of these processes. This probe absorption is the origin of the TO nonlinearity which causes the well-known hysteresis behavior

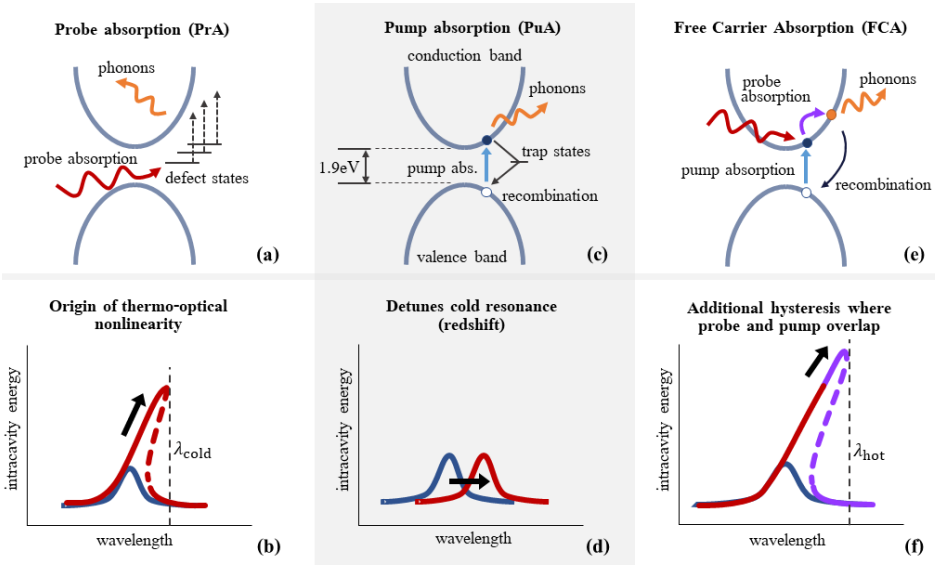

Figure 4.2: Schematic of the TO sources in the PhC. (a) NIR probe absorption by defect states causes (b) hysteresis behavior at high probe power (red lineshape). The blue lineshape illustrates the low-power, linear response. Dashed lines are instable branches. (c) Interband pump absorption of the 405 nm excitation laser generates a (d) shift of the resonance, *i.e.*, a redshift of the complete lineshape, here depicted for the low-power lineshape. (e) Pump absorption creates free carriers that absorb NIR probe light, *i.e.*, FCA (purple arrow), this causes an (f) increase in the hysteresis in the nonlinear lineshape (red and purple). The right hysteresis edge of the pumped nonlineare lineshape (λ_{hot} in (f)) is redshifted with respect to the hysteresis edge of the unpumped nonlinear lineshape (λ_{cold} in (b)).

shown in Fig. 4.2(b) [35] and Chapter 3. Secondly, Fig. 4.2(c,d) shows how direct heating by the pump causes a redshift of the cold cavity resonance λ_0 when the thermal profile overlaps with the optical mode profile of the resonance [29]. In Fig. 4.2(e,f) a third source of heat presents itself when the free carriers generated by the pump absorb a probe photon, *i.e.*, FCA. These hot carriers heat the lattice and increase the TO redshift, causing an increase in the hysteresis. The FCA process occurs only in the region where the pump spot and optical mode profile overlap, and is proportional to the product of pump and probe energy densities.

We model the system by solving the coupled optical resonance condition and the partial differential equation for thermal diffusion for all three TO sources. We solve the differential equation numerically using the Sturm-Liouville theory,

propagating the modes in an orthogonal base[36]. See Appendix 4.6 for a full treatment of the theoretical model.

A qualitatively similar model by Iadanza et al.[35] differs from ours as it approximates the temperature distribution with elliptical regions. However, to interpret mode profile scans we need to specifically take into account the spatial degrees of freedom of the PhCR mode and use it to evaluate the temperature distribution in time and space on a high resolution grid.

4.3 Results

We perform NPMS measurements on a high-Q mode-gap cavity and image the optical mode profile. The procedure consists of a pump line scan: probing at consecutive pump positions in a horizontal or vertical line. At each pump position we take a probe wavelength sweep (in the direction of increasing λ) to obtain a cross section of the mode profile. First we obtain both the theoretical and experimental response of the known mode profile of the fundamental mode-gap resonance with Q = 619000 and validate the TO model. Secondly, we demonstrate that the increased pump sensitivity due to FCA resolves the first higher-order mode of the mode-gap resonance with Q = 340000 in the nonlinear regime.

Fundamental mode-gap resonance: vertical cross section

Fig. 4.3(a) shows a two-dimensional NPMS measurement of the fundamental mode-gap cavity yielding an image of the mode profile. The NPMS measurement is performed with a 0.5-μm pump spot, the signal plotted is the pump induced redshift of the sharp right hysteresis edge of the cavity lineshape, see Fig. 4.2(b,f). The inset of the pump spot shows that the resolution of our measurement is close to the beam size of our spatial probe.

Fig. 4.3(b) shows the optical mode profile of the 3D FDTD-simulated mode-gap resonance that we use to generate the theoretical NPMS obtained profile. The vertical line scan goes through the center of the mode-gap resonator as depicted in Fig. 4.3(c). While with our current pump spot size we do not experimentally resolve the standing wave fringes of the FDTD calculated mode, we do observe an elliptical mode profile.

In Fig. 4.4 we show the experimental and theoretical NPMS vertical line scan of the mode-gap resonance profile, performed with a 0.5 μm FWHM pump spot. This was done for three increasing probe energies to investigate the response of the mode in both the linear and nonlinear regime, effectively increasing FCA. We observe a nearly perfect agreement between the experimentally measured and numerically calculated profiles. A full list of the fit parameters and constants used in the model can be found in Appendix 4.7. All fits are found by manually

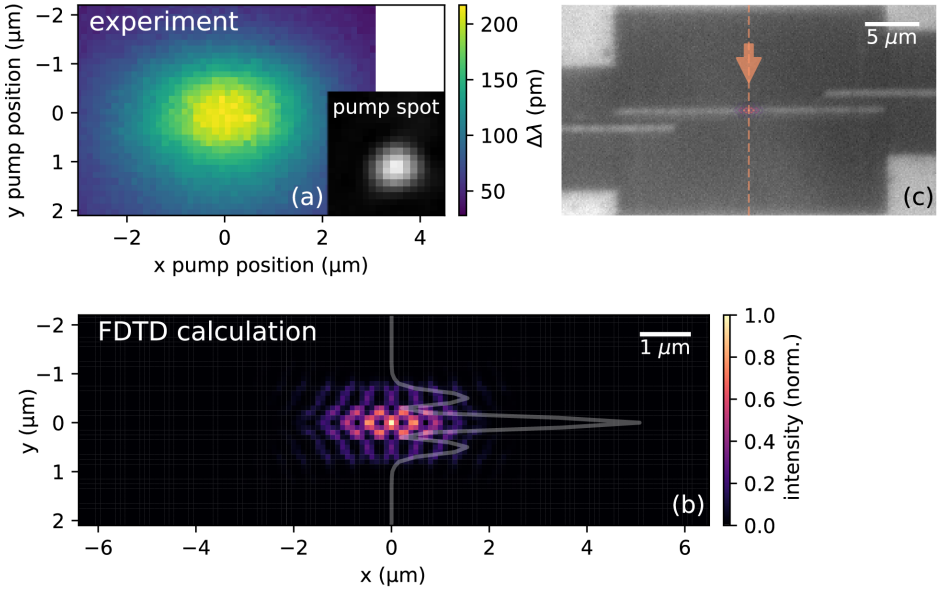

Figure 4.3: Experimental and theoretical fundamental cavity mode. (a) Experimental 2D NPMS measurement of the mode, we plot $\Delta\lambda = \lambda_{\text{hot}} - \lambda_{\text{cold}}$ the pump induced redshift of the right hysteresis edge, see Figs. 4.2(b,f). The inset shows a CCD image of the pump spot that took the 2D grid scan. (b) FDTD calculated mode profile of the fundamental mode, with a vertical cross section through the center of the mode plotted in gray. This mode is used as input mode for the TO model. (c) Overlay of the input mode on top of a CCD image of the PhC waveguide. Orange dashed line and arrow indicate line scan and scan direction for the NPMS vertical cross section measurement shown in Fig. 4.4.

adjusting four fit parameters, as an automated fit procedure failed to converge in a reasonable number of iterations, especially as each iteration requires a time-intensive calculation.

In Figs. 4.4(a,d), at low probe power, pump absorption is the only significant TO effect. The resonance is redshifted by the pump where the mode profile and pump thermal profile overlap, i.e, when the pump is close to the cavity. A dip in the redshift when the pump hits the center of the waveguide is explained by considering the thermal conductance of the PhC. On the waveguide there are no air holes, causing a higher thermal conductance. Additionally, in the model we account for the observation that the pump is partially reflected by the waveguide (it shows up bright at the pump wavelength) diminishing the absorbed-pump power by 20% when the pump beam is on the waveguide.

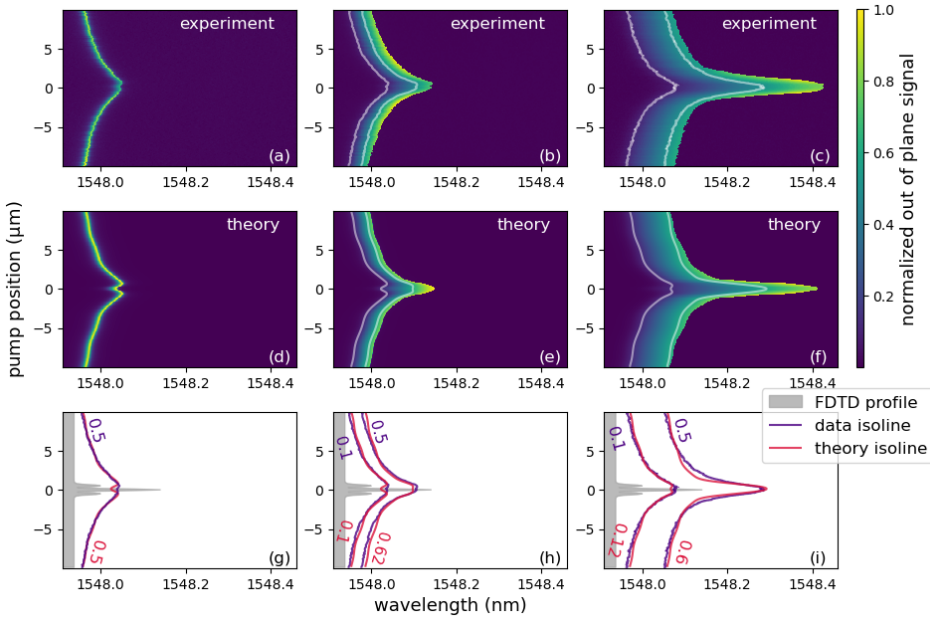

Figure 4.4: NPMS vertical cross section of the mode profile of a mode-gap cavity, experimentally measured via the out of plane scattered light at (a) the linear response regime at low input power, at (b) increasing input power and (c) high input power deep into the nonlinear response regime. The simulated NPMS mode profile in (d), (e) and (f) for increasing input power left to right, generated with the input mode of Fig. 4.3, matching the corresponding experimental results. See Appendix 4.7 for fit details. (g,h,i) The isolines of the profiles, corresponding to the white isolines in (b,c,e,f). A cross section of the FDTD profile (corresponding to Fig. 4.3(c)) is indicated with a shaded area (gray).

In Figs. 4.4(b,e), at increasing probe power, the TO effect causes an asymmetric lineshape (see Figs. 4.2(b,f)) that maximally detunes the resonance when pump and probe heat up the mode cumulatively.

In Figs. 4.4(c,f) we probe deep into the non-linear regime. The high-energy-density areas of the mode profile become even more pronounced, as the TO detuning reaches further into the long wavelengths due to FCA. It is by these shapes that we scale the FCA effect to match the experiment and find an agreement with a carrier lifetime of $\tau_c \approx 0.4$ ns for all simulations throughout this article. The strength of the FCA source is related to the product of the carrier lifetime and the effective cross section, see Appendix 4.6 for details.

The carrier lifetime is the parameter with the largest a priori uncertainty since no measurements in these type of GaInP slabs exist to the best of our knowledge. Therefore we use it as a fit parameter. Our fit results should not be regarded as a measurement of the carrier lifetime, though it falls within the expected range for a GaInP PhC considering small volume to surface ratio [37,37–40].

The lifetime translates to a carrier density of $\rho_c \approx 1 \times 10^{16}$ cm^{-3} or equivalently not more than ~ 500 carriers in the cavity at any time.

In Figs 4.4(g-i) low- and mid-level isolines of the experimental and theoretical profiles are shown. Since the high intensity edge of the high-power profiles marks the transition to an unstable state (see lineshapes of Fig. 4.2(b,f)) the edge is very sensitive to any effect that might disturb the balance at the edge of the stable energy branch, such as a nearby dark mode, variation in the incoupling efficiency, or disorder in the PhC. Therefore, comparison of isolines that are situated in the stable region of the profile is more reliable. In Appendix 4.8 we present another mode-gap resonance that has a suppressed high energy density peak of the mode profile, but nonetheless shows excellent agreement with the model in the stable regimes of the mode profile.

Fig. 4.4 demonstrates that imaging of the PhCR mode improves at high probe power since the highly broadened FDTD profile in Fig. 4.4(g) gains resolution in Fig. 4.4(i).

Higher order resonance: horizontal cross section

Fig. 4.5(a) depicts the first higher-order mode of a Hermite-Gaussian function by which we approximate the first higher-order mode of the mode-gap resonance. We use this higher-order mode to generate the theoretical NPMS profile by performing a horizontal scan over the center of the waveguide as shown in Fig. 4.5(b).

Fig. 4.6 shows the experimentally and theoretically obtained mode profile of the higher-order mode-gap resonance in both the low and high probe power regime. The low-probe power, experimental profile in Fig. 4.6(a) shows no details that would point to the measurement of a higher-order mode or any other mode

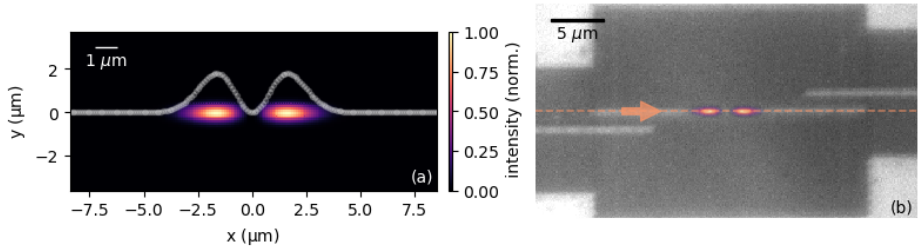

Figure 4.5: Input mode for the theoretical NPMS horizontal line scan. (a) Render of the first higher-order Hermite-Gaussian function that is used as the input mode of the theoretical NPMS profile. A horizontal cross section of the input mode is plotted in gray. (b) Overlay of the input function on top of a CCD image of the PhC waveguide. The orange dashed line and arrow indicate the horizontal line scan and scan direction.

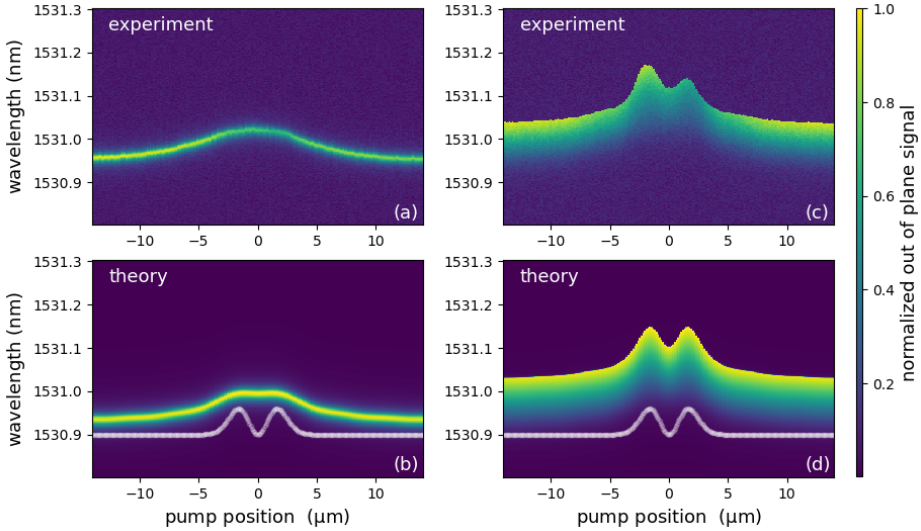

Figure 4.6: NPMS horizontal line scan of the first higher-order mode-gap resonance, yielding a cross section of the optical mode profile. (a) The profile is experimentally measured via out-of-plane scattered light at low probe power and (b) the theoretical profile is generated with the input mode from Fig. 4.5 at low probe power. Additionally, (c) the experimentally measured profile at high probe power and (d) the theoretical profile at high probe power. For the theoretical profiles, a horizontal cross section of the input mode is plotted in white.

that would have multiple peaks. In correspondence, the low-power theoretical profile in Fig. 4.6(b) shows the same single broad-peaked shape.

However, at higher probe power the NPMS experimental mode profile in Fig. 4.6(c) reveals a centered double peak that highly resembles the double peak of the higher-order mode-gap profile modeled in Fig. 4.6(d). We see a very good agreement between experiment and theory is obtained by assuming this resonance is the first higher-order mode of the mode-gap resonance. We note that the characteristics of this higher-order mode can only be observed in the nonlinear regime at high probe power, where FCA is significant, proving again that our method enables high-resolution mode mapping of the resonance.

The distance between the peaks in Fig. 4.6(d) is fitted to match Fig. 4.6(c) by setting the waist of the higher-order Hermite-Gaussian mode to $w = 2.3\mu m$. We remark that the waist of the higher-order mode is of the same order as the fundamental mode, see Fig. 4.3.

We use the same fit method and parameters in the model as before in Fig. 4.4, including the same carrier lifetime that scales the FCA source strength. See Appendix 4.7 for a full list of constants and parameters.

4.4 Discussion

In our current experimental setup we do not reach the resolution limit of the imaging method. The most important limiting factor for the resolution is the pump focus, as illustrated in Fig. 4.3. Therefore we simulate with the realistically smallest pump spot of 213 nm (obtainable with an objective of NA = 0.95) and find a resolution limit of 240 nm using Sparrow's criterion, indeed approaching the diffraction limit of the 405 nm pump light itself. The resolution limit of 240 nm opens up prospects of measuring the fringes of the standing waves of the optical mode in Fig. 4.3(b). See Appendix 4.9 for details on the resolution limit simulation.

We note that, other than in NSOM measurements, we probe the field inside the PhC membrane as opposed to just above the PhC surface. With the absorption coefficient estimated at 9×10^4 [41] the 180 nm thick slab will absorb 80% of the pump light with a slight bias towards the surface. Therefore our probing is determined by the cylindrical volume integral where absorbed pump light and mode profile overlap in the slab.

4.5 Conclusion

We provide a simple, non-invasive approach to image optical mode profiles in the far-field, with its own unique trade-off between spatial and spectral resolution, reproducibility, and applicability. We demonstrated that NPMS can be used to

obtain a high-resolution mode mapping of ultrahigh-Q PhC resonances by driving the optical mode into the TO nonlinear regime. We push the boundaries of far-field imaging [42] and resolve the fringes in the profile of a higher-order mode.

The TO model we present shows that FCA, invoked by high-power probing of the mode, is the origin of the augmented resolution, as pump and probe light have an accumulative effect on the detuning of the resonance. In this way, we beat the convolution effects of the broad thermal profile of the pump spot. This is surprising at the low carrier density of $\approx 1 \times 10^{16}$ cm^{-3}, as typical carrier index modulation experiments require densities on the order of 10^{18-20} cm^{-3} [28,43] and thus pulsed light.

NPMS offers a convenient cw low pump-power method for for instance silicon photonic circuits and devices designed to combine high-Q dielectric resonators with plasmonic systems [44]. Additionally, it can provide insight into the field inside the dielectric material, measuring the mode profile within the PhC slab. Our method can easily be expanded to time-resolved measurements. Moreover, opportunities to dynamically tune and configure modes — possibly using opposite-sign index modulation of the different nonlinear effects in the material — are worthy of exploring.

4.6 Appendix A: Theory

In this section we formulate a thermo-optical (TO) model by solving the optical resonance condition coupled to the thermal diffusion equations for all three TO sources. This means we will find an expression for the TO sources and work towards the full heat equation of the system, taking into account the optical mode in the waveguide, the thermal properties of the PhC and the optical pump.

Carrier absorption

First we will find an expression for the heat produced by free carrier absorption (FCA) as depicted in Fig. 4.2(e), *i.e.*, free carriers produced by the pump light absorb probe light. To find the thermal dissipation from the FCA source we multiply the optical absorption coefficient with the energy density of the probe field. This gives us the energy transfer from probe light to free carriers, *i.e.*, the FCA heating term,

$$S_{\mathrm{FCA}} = \alpha_{\mathrm{FCA}}(x,y,t) \times \left(\frac{c}{n} E_{\mathrm{pr}}(t) U_{\mathrm{pr}}(x,y) I_{\mathrm{pr}}(x,y,t)\right), \tag{4.1}$$

where $\alpha_{\mathrm{FCA}}(x,y)$ is the probe absorption coefficient, c is the speed of light, n the refractive index, $E_{\mathrm{pr}}(t)$ is the input probe light energy, $U_{\mathrm{pr}}(x,y)$ the optical

mode profile of the probe field, and $I_{\mathrm{pr}}(x, y, t)$ is the spectral lineshape of the resonance.

The probe energy is determined by the input probe power P_{pr} and a coupling parameter τ_{pr} accounting for the incoupling efficiency of the probe light to the cavity, which means $E_{\mathrm{pr}}(t) = \tau_{\mathrm{pr}} P_{\mathrm{pr}}(t)$. The absorption coefficient is related to the effective FCA cross section σ_{FCA} and the carrier density $\rho_c(x, y)$ by $\alpha_{\mathrm{FCA}}(x, y, t) = \sigma_{\mathrm{FCA}} \rho_c(x, y, t)$. Where the effective absorption cross section is the summed cross sections of all carrier types, where for each type $\sigma_i = e^3 \lambda_{\mathrm{pr}}^2 / 4\pi^2 c^3 (m_i^*)^2 \mu_i n \varepsilon_0$ is the absorption cross section of a single carrier [45]. Here e is the electron charge, λ_{pr} the probe wavelength, m^* the effective carrier mass, μ is the carrier mobility and ϵ_0 the vacuum permittivity.

The carriers are created by the pump light. We assume the carriers stay localized on the optical timescale [37], which means the carrier density is directly proportional to the local production rate of carriers and their lifetime, such that

$$\rho_c(x, y, t) = \frac{\tau_c}{d\hbar\omega_{\mathrm{pu}}} P_{\mathrm{pu}}(t) U_{\mathrm{pu}}(x, y), \tag{4.2}$$

with τ_c the average lifetime of a carrier, d the thickness of the membrane, ω_{pu} the pump light frequency, $P_{\mathrm{pu}}(t)$ the pump power, and $U_{\mathrm{pu}}(x, y)$ the optical mode profile of the pump. This finally leads to the expression

$$\begin{aligned} S_{\mathrm{FCA}} = \sigma_{\mathrm{FCA}} &\left(\frac{\tau_c}{d\hbar\omega_{\mathrm{pu}}} P_{\mathrm{pu}}(t) U_{\mathrm{pu}}(x, y) \right) \\ &\times \left(\frac{c\tau_{\mathrm{pr}}}{n} P_{\mathrm{pr}}(t) U_{\mathrm{pr}}(x, y) I_{\mathrm{pr}}(x, y, t) \right). \end{aligned} \tag{4.3}$$

Heat Equation

The heat equation, taking into account all TO sources (shown in Fig. 4.2), is a partial differential equation which we solve using a stable spectral method on a high-resolution space-time grid. We combine the in-plane cooling through dissipation in the PhC membrane, out-of-plane cooling via the surrounding gas layer and substrate, and all heating terms, including the FCA term of Eq. (4.3), into the heat equation

$$\begin{aligned} C_{\mathrm{2D}}\frac{\partial T(x,y,t)}{\partial t} = & -K_{\mathrm{2D}}\nabla^2 T(x,y,t) \\ & -K_{\mathrm{gas}}(T(x,y,t)-T_0) \\ & +\alpha_{\mathrm{PrA}}P_{\mathrm{pr}}(t)U_{\mathrm{pr}}(x,y) \\ & +\beta_{\mathrm{PuA}}P_{\mathrm{pu}}(t)U_{\mathrm{pu}}(x,y) \\ & +\sigma_{\mathrm{FCA}}\frac{\tau_{\mathrm{c}}}{d\hbar\omega_{\mathrm{pu}}}P_{\mathrm{pu}}(t)U_{\mathrm{pu}}(x,y) \\ & \qquad \times\frac{c\tau_{\mathrm{pr}}}{n}P_{\mathrm{pr}}(t)U_{\mathrm{pr}}(x,y)I_{\mathrm{pr}}(x,y,t), \end{aligned} \tag{4.4}$$

where C_{2D} is the 2D specific heat of the PhC membrane, K_{2D} the thermal conductivity of the PhC membrane, and K_{gas} the thermal conductance of the gas layer between the air-suspended membrane and substrate. At the boundary we have $T = T_0$ the temperature at the edge of the photonic crystal where it meets the substrate. Out-of-plane cooling via the other side of the PhC membrane into free space is neglected, as this contributes less then one percent of the heat loss. For the heat produced via probe absorption we take into account the absorption fraction α_{PrA}, *i.e.*, the probability a cavity photon is absorbed rather than scattered or leaked out of the cavity. Direct pump heating is related to β_{PuA}, the absorption fraction of the pump light.

The resonance condition is hidden in the optical energy density of the probe field that is related to the spectral lineshape of the resonance

$$I_{\mathrm{pr}}(x,y,t) = \frac{\Gamma^2}{\Gamma^2 + (\Delta - \delta_{\mathrm{th}}(x,y,t))^2}, \tag{4.5}$$

where Γ is the resonance linewidth, $\Delta \equiv \lambda_{\mathrm{pr}} - \lambda_0$ is the detuning, and $\delta_{\mathrm{th}}(t)$ is the thermal resonance shift that causes a dynamic detuning expressed by

$$\delta_{\mathrm{th}}(x,y,t) = \eta \int U_{\mathrm{pr}}(x,y)T(x,y,t)dxdy. \tag{4.6}$$

Here, η is the thermo-optical coefficient of the semiconductor material. Eq. (4.5) reflects the fact that the resonance has a dynamic Lorentzian lineshape that detunes in accordance with the temperature. For our experimental conditions the resonance frequency detunes linearly with temperature [46]. The optical mode profile of the resonance, as depicted in Fig. 4.3(b) and Fig. 4.5(a), is inserted into $U_{\mathrm{pr}}(x,y)$. We then solve Eq. (4.5) numerically using Sturm-Liouville theory, propagating the modes in an orthogonal base [36].

4.7 Appendix B: Simulation Parameters

Tables 4.1 and 4.2 shows the parameters and constants used in the model to generate Figs. 4.4(d,e,f), 4.6(b,d), and 4.7(d,e,f).

The on-chip pump power cannot be directly measured. We measure the upper limit of the on-chip pump power, scale to fit the redshift of the cold resonance observed in the experiment, and then fixed for all simulations. The shift of the cold resonance (in the linear response regime of the cavity) is directly related to the pump power and has no crosstalk with the other fit parameters.

The probe energy $E_{\rm pr}$ determines the detuning at which the resonance drops out of stability, *i.e.*, the high intensity edge. Therefore, the probe energy is a fit parameter to match the experimental hysteresis edge at pump position $\pm 10\mu m$ where the pump has negligible effect on the optical mode. The spectrum of the input probe energy is not entirely flat, therefore we normalize it using the back reflected light measured through the injection waveguide.

The diminished pump absorption on the waveguide (caused by partial reflection on the waveguide) is determined in the vertical scan by fitting the fringe on top of the waveguide, see Fig. 4.4(a,d).

The fourth and last fit parameter is related to the strength of the FCA term, *i.e.*, the amount of heat produced by FCA. Looking at Eq. (4.3) the FCA source is proportionate to the product $\sigma_{\rm FCA}\tau_c$, the effective FCA cross section and the carrier lifetime. We use the effective carrier mass and mobility to calculate the effective cross section and use the carrier lifetime as fit parameter to match the resolution of the experimental mode profile. A small carrier lifetime leads to a broadened profile with less sharp peaks and vice versa.

Using the values from Tables 4.1 and 4.2 the fit yields a carrier lifetime of $\tau_c \approx 0.4$ ns. This is an approximated value, as the effective cross section has large uncertainty due to the fact that the population of heavy and light carrier holes is unknown and we work with a 50/50 distribution. If only light holes are part of the FCA process the carrier lifetime would average out to $\tau_c \approx 0.2$ ns. Additionally, the effective carrier mass and carrier mobility cannot directly be measured in our experimental setup, thus we use literature values with limited precision. With Eq. (4.2) we find the carrier density created by the cw pump spot to be $\rho_c \simeq \tau_c P_{\rm pu}/\hbar\omega_{\rm pu} d\pi r^2$, where r is half the FWHM of the pump spot. This leads to the carrier density of $\rho_c \approx 1\times 10^{16}$ cm^{-3}, or equivalently, not more than $\sim$500 carriers in the PhCR at any time.

Constants and parameters used in the model

	symbol	value	source
refractive index	n	3.06	[47]
thermal conductivity of GaInP	$\kappa_{Ga_{0.51}In_{0.49}P}$	4.9 W/m.K	[48]
thermal conductivity of N_2	κ_{N_2}	0.024 W/m.K	[49]
specific heat of GaInP	C_{sp}	310 J/K.kg	[50]
density of GaInP	ρ	4810 kg/m^3	[51]
thickness of the PhC membrane	h	180 nm	
filling fraction	$\phi(x,y)$	0.714 (PhC membrane)	
		1.0 (waveguide, bulk)	
2D specific heat	$C_{2D}(\phi(x,y))$	$h\phi(x,y)\rho C_{sp}$	
thermo-optical coefficient	$\eta = dT/dn$	-2×10^{-4} K^{-1}	[46]
on-chip upper limit of pump power	P_{lim}	1.56 μW	experimentally measured
on-chip pump power	P_{pu}	$0.35 \times P_{lim}$	fit parameter
absorption fraction of probe	α_{PrA}	0.05	estimated value
absorption fraction of pump	β_{PuA}	1.0 (PhC membrane)	
		0.2 (waveguide)	fit parameter
electron effective mass	m_e^*	$0.088m_0$	[47]
light hole effective mass	m_{lh}^*	$0.12m_0$	[47]
heavy hole effective mass	m_{hh}^*	$0.7m_0$	[47]
electron mobility	μ_e	1000 cm^2/Vs	[47]
hole mobility	μ_h	40 cm^2/Vs	[47]
effective FCA cross section	σ_{FCA}	$\sigma_e + 1/2(\sigma_{lh} + \sigma_{hh})$	

Table 4.1: (Part I) Constants and parameters used to generate the theoretical mode profiles of Figs. 4.4(d,e,f), 4.6(b,d) and Fig. 4.7(d,e,f).

Constants and parameters used in the model

	symbol	value	source
Vertical line scan, Fig. 4.4:			
resonance wavelength	λ_0	1547.960 nm	experimentally measured
resonance linewidth	Γ	5 pm	experimentally measured
FWHM of the pump in (x,y)-direction		(534, 587) nm	experimentally measured
carrier lifetime	τ_c	0.4 ns	fit parameter
probe light energy	$E_{\mathrm{pr}} = \tau_{\mathrm{pr}} P_{\mathrm{pr}}$	0.2 fJ	fit parameter Fig. 4.4(d)
		1.6 fJ	fit parameter Fig. 4.4(e)
		3.6 fJ	fit parameter Fig. 4.4(f)
Horizontal line scan, Fig. 4.6:			
resonance wavelength	λ_0	1530.952 nm	experimentally measured
resonance linewidth	Γ	9 pm	experimentally measured
FWHM of the pump in (x,y)-direction		(615, 548) nm	experimentally measured
carrier lifetime	τ_c	0.4 ns	fit parameter
probe light energy	$E_{\mathrm{pr}} = \tau_{\mathrm{pr}} P_{\mathrm{pr}}$	0.1 fJ	fit parameter Fig. 4.6(b)
		2.1 fJ	fit parameter Fig. 4.6(d)
Vertical line scan, Fig. 4.7:			
resonance wavelength	λ_0	1536.106 nm	experimentally measured
resonance linewidth	γ	4 pm	experimentally measured
FWHM of the pump in (x,y)-direction		(615, 548) nm	experimentally measured
carrier lifetime	τ_c	0.4 ns	fit parameter
probe light energy	$E_{\mathrm{pr}} = \tau_{\mathrm{pr}} P_{\mathrm{pr}}$	0.3 fJ	fit parameter Fig. 4.7(d)
		1.7 fJ	fit parameter Fig. 4.7(e)
		6.6 fJ	fit parameter Fig. 4.7(f)

Table 4.2: (Part II) Constants and parameters used to generate the theoretical mode profiles of Figs. 4.4(d,e,f), 4.6(b,d) and Fig. 4.7(d,e,f).

4.8 Appendix C: Suppressed FCA response

At high optical probe energy the high energy branch of a bistable state can be susceptible to many disturbances that destabilize the branch. This is demonstrated in Fig. 4.7 where we show a resonance that is suppressed in its nonlinear behavior as we do not see states with large detuning when we have overlap between pump and mode, due to an instable high energy branch. Nevertheless, the isolines in the stable part of the high energy branch (at low and medium intracavity energy) still match the theory.

4.9 Appendix D: Resolution limit simulation

The most important limiting factor for the resolution is the size of the pump beam, determined by the pump light wavelength and NA of the focusing objective via the diffraction limit $\lambda/2\text{NA}$. The current setup has NA = 0.4 and $\lambda_{\text{pump}} = 405$ nm. Objectives that work for both the NIR and pump wavelength go up to NA = 0.95. In principle the imaging method could be performed with a shorter wavelength pump light to obtain higher resolution. The limited transmission spectrum for a corresponding objective might mean the NIR light must be detected via the PhC waveguide transmission signal instead.

To calculate the resolution limit achievable with our current 405 nm pump light we use a very tight but realistic pump focus of 213 nm that can be obtained with an objective of NA = 0.95. We then generate the mode profile for two sharp, adjacent Gaussian modes with FWHM = 100 nm and varying distance on the x-axis between them, using our TO model.

Fig. 4.8 shows the result of the simulation demonstrating that the resolution limit lies at 240 nm followings Sparrow's criterion. All constants and parameters are identical to the horizontal scan of Fig. 4.6 except for an adjusted pump FWHM of 213 nm in both the x and y direction (see Tables 4.1 and 4.2).

The simulation does not include carrier diffusion, which might become significant at the nanometer scale. This is highly dependent on the unknown carrier lifetime. We estimate the diffusion coefficient at $D_e = 26\ cm^2/s$ and $D_h = 1\ cm^2/s$ for the electrons and holes respectively, using the Hall mobility and Einstein relation. The diffusion length is $\sqrt{< r^2 >_i} = \sqrt{4D_i\tau_c}$ for each carrier type in the 2D slab. For a carrier lifetime of $\tau_c = \{10, 100, 400\}$ ps we have diffusion lengths of $\{321, 1016, 2033\}$ nm and $\{64, 203, 407\}$ nm for the electrons and holes respectively.

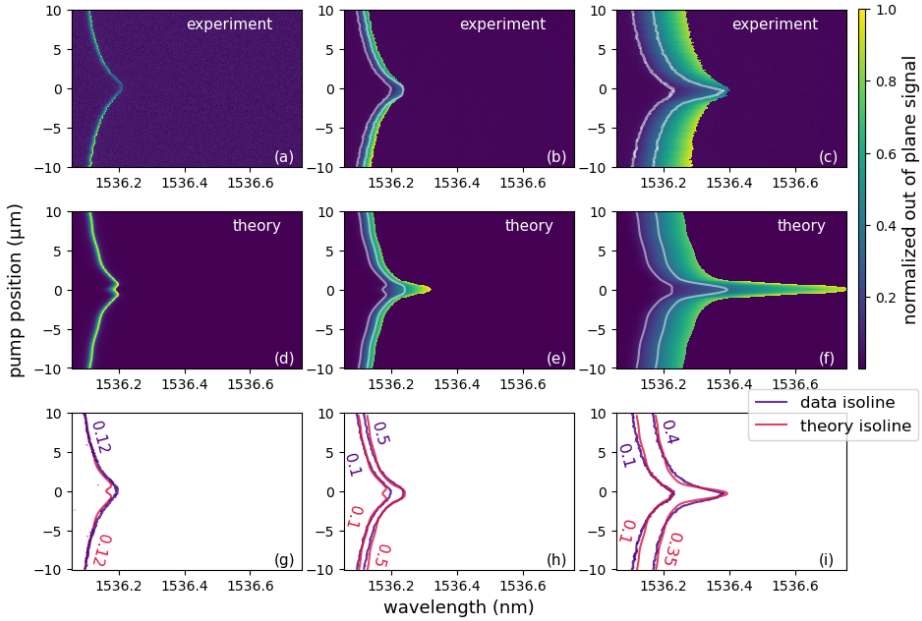

Figure 4.7: NPMS vertical cross section of the mode-gap cavity profile, experimentally measured at (a) low input power, (b) increasing input power and (c) high input power. The simulated NPMS mode profile in (d), (e) and (f) for increasing input power, generated with the input mode of Fig. 4.3. (g,h,i) The isolines of the profiles.

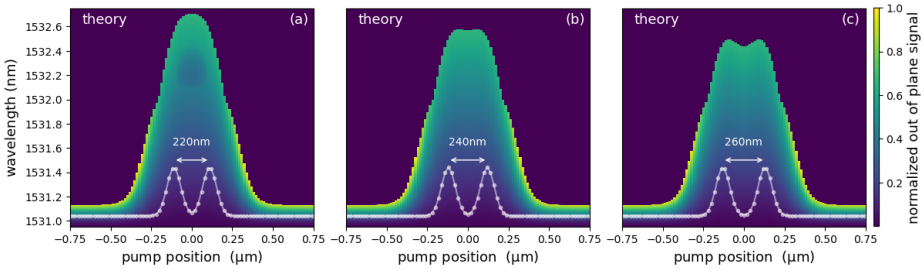

Figure 4.8: Simulation of the resolution limit using Sparrow's criterion. Increasing distance between Gaussian peaks: (a) 220, (b) 240, (c) 260 nm. Input modes are plotted in white. At (b) 240 nm the two peaks can still be resolved.

4.10 References

[1] P. Lodahl, S. Mahmoodian, and S. Stobbe, "Interfacing single photons and single quantum dots with photonic nanostructures," Reviews of Modern Physics **87**, 347 (2015).

[2] M. Ghulinyan and L. Pavesi, *Light Localisation and Lasing: Random and Pseudo-Random Photonic Structures* (Cambridge University Press, 2015).

[3] T. Baba, "Slow light in photonic crystals," Nature Photonics **2**, 465 (2008).

[4] S. Noda and T. Baba, *Roadmap on Photonic Crystals*, vol. 1 (Springer Science & Business Media, 2003).

[5] T. Asano and S. Noda, "Photonic crystal devices in silicon photonics," Pro. IEEE **106**, 2183–2195 (2018).

[6] L. P. Caballero, M. L. Povinelli, J. C. Ramirez, P. S. S. G. aes, and O. P. V. Neto, "Photonic crystal integrated logic gates and circuits," Optics Express **30**, 1976–1993 (2022).

[7] G. Moody, V. Sorger, P. Juodawlkis, W. Loh, C. Sorace-Agaskar, A. E. Jones, K. Balram, J. Matthews, A. Laing, M. Davanco *et al.*, "Roadmap on integrated quantum photonics," Journal of Physics: Photonics (2021).

[8] T. Wu, M. Gurioli, and P. Lalanne, "Nanoscale light confinement: the Q's and V's," ACS Photonics **8**, 1522–1538 (2021).

[9] C. Husko, A. De Rossi, S. Combrié, Q. V. Tran, F. Raineri, and C. W. Wong, "Ultrafast all-optical modulation in GaAs photonic crystal cavities," Applied Physics Letters **94**, 021111 (2009).

[10] K. Nozaki, S. Matsuo, T. Fujii, K. Takeda, A. Shinya, E. Kuramochi, and M. Notomi, "Femtofarad optoelectronic integration demonstrating energy-saving signal conversion and nonlinear functions," Nature Photonics **13**, 454–459 (2019).

[11] R. Bruck, K. Vynck, P. Lalanne, B. Mills, D. J. Thomson, G. Z. Mashanovich, G. T. Reed, and O. L. Muskens, "All-optical spatial light modulator for reconfigurable silicon photonic circuits," Optica **3**, 396–402 (2016).

[12] E. Kuramochi, K. Nozaki, A. Shinya, K. Takeda, T. Sato, S. Matsuo, H. Taniyama, H. Sumikura, and M. Notomi, "Large-scale integration of wavelength-addressable all-optical memories on a photonic crystal chip," Nature Photonics **8**, 474 – 481 (2014).

[13] G. Marty, S. Combrié, F. Raineri, and A. De Rossi, "Photonic crystal optical parametric oscillator," Nature Photonics **15**, 53–58 (2021).

[14] R. Faggiani, A. Baron, X. Zang, L. Lalouat, S. A. Schulz, B. O'regan, K. Vynck, B. Cluzel, F. De Fornel, T. F. Krauss *et al.*, "Lower bound for the spatial extent of localized modes in photonic-crystal waveguides with small random imperfections," Scientific Reports **6**, 1–9 (2016).

[15] N. Rotenberg and L. Kuipers, "Mapping nanoscale light fields," Nature Photonics **8**, 919–926 (2014).

[16] S. Mujumdar, A. F. Koenderink, T. Sünner, B. Buchler, M. Kamp, A. Forchel, and V. Sandoghdar, "Near-field imaging and frequency tuning of a high-Q photonic crystal membrane microcavity," Optics Express **15**, 17214–17220 (2007).

[17] J. Knight, N. Dubreuil, V. Sandoghdar, J. Hare, V. Lefevre-Seguin, J. Raimond, and S. Haroche, "Characterizing whispering-gallery modes in microspheres by direct observation of the optical standing-wave pattern in the near field," Optics Letters **21**, 698–700 (1996).

[18] M. Schnell, A. Garcia-Etxarri, J. Alkorta, J. Aizpurua, and R. Hillenbrand, "Phase-resolved mapping of the near-field vector and polarization state in nanoscale antenna gaps," Nano Letters **10**, 3524–3528 (2010).

[19] N. Caselli, T. Wu, G. Arregui, N. Granchi, F. Intonti, P. Lalanne, and M. Gurioli, "Near-field imaging of magnetic complex mode volume," ACS Photonics **8**, 1258–1263 (2021).

[20] B. Le Feber, N. Rotenberg, D. M. Beggs, and L. Kuipers, "Simultaneous measurement of nanoscale electric and magnetic optical fields," Nature Photonics **8**, 43–46 (2014).

[21] K. G. Cognée, W. Yan, F. L. China, D. Balestri, F. Intonti, M. Gurioli, A. F. Koenderink, and P. Lalanne, "Mapping complex mode volumes with cavity perturbation theory," Optica **6**, 269–273 (2019).

[22] F. B. Arango, F. Alpeggiani, D. Conteduca, A. Opheij, A. Chen, M. I. Abdelrahman, T. F. Krauss, A. Alù, F. Monticone, and L. Kuipers, "Cloaked near-field probe for non-invasive near-field optical microscopy," Optica **9**, 684–691 (2022).

[23] L. Lalouat, B. Cluzel, F. de Fornel, P. Velha, P. Lalanne, D. Peyrade, E. Picard, T. Charvolin, and E. Hadji, "Subwavelength imaging of light confinement in high-Q/small-V photonic crystal nanocavity," Applied Physics Letters **92**, 111111 (2008).

[24] B. J. Brenny, D. M. Beggs, R. E. van der Wel, L. Kuipers, and A. Polman, "Near-infrared spectroscopic cathodoluminescence imaging polarimetry on silicon photonic crystal waveguides," ACS Photonics **3**, 2112–2121 (2016).

[25] S. Choi, C. Ton-That, M. R. Phillips, and I. Aharonovich, "Observation of whispering gallery modes from hexagonal ZnO microdisks using cathodoluminescence spectroscopy," Applied Physics Letters **103**, 171102 (2013).

[26] M. Kuttge, F. J. García de Abajo, and A. Polman, "Ultrasmall mode volume plasmonic nanodisk resonators," Nano Letters **10**, 1537–1541 (2010).

[27] W. R. McGehee, T. Michels, V. Aksyuk, and J. J. McClelland, "Two-dimensional imaging and modification of nanophotonic resonator modes using a focused ion beam," Optica **4**, 1444–1450 (2017).

[28] R. Bruck, B. Mills, B. Troia, D. J. Thomson, F. Y. Gardes, Y. Hu, G. Z. Mashanovich, V. M. Passaro, G. T. Reed, and O. L. Muskens, "Device-level characterization of the flow of light in integrated photonic circuits using ultrafast photomodulation spectroscopy," Nature Photonics **9**, 54 (2015).

[29] J. Lian, S. Sokolov, E. Yüce, S. Combrié, A. De Rossi, and A. P. Mosk, "Measurement of the profiles of disorder-induced localized resonances in photonic crystal waveguides by local tuning," Optics Express **24**, 21939–21947 (2016).

[30] S. Sokolov, J. Lian, E. Yüce, S. Combrié, G. Lehoucq, A. De Rossi, and A. P. Mosk, "Local thermal resonance control of GaInP photonic crystal membrane cavities using ambient gas cooling," Applied Physics Letters **106**, 171113 (2015).

[31] J. Lian, S. Sokolov, E. Yüce, S. Combrié, A. D. Rossi, and A. P. Mosk, "Measurement of the profiles of disorder-induced localized resonances in photonic crystal waveguides by local tuning," Optics Express **24**, 21939–21947 (2016).

[32] E. F. Schubert, *Light-Emitting Diodes* (E. Fred Schubert, 2018).

[33] S. Combrié, Q. V. Tran, A. De Rossi, C. Husko, and P. Colman, "High quality GaInP nonlinear photonic crystals with minimized nonlinear absorption," Applied Physics Letters **95**, 221108 (2009).

[34] E. Kuramochi, M. Notomi, S. Mitsugi, A. Shinya, T. Tanabe, and T. Watanabe, "Ultrahigh-Q photonic crystal nanocavities realized by the local width modulation of a line defect," Applied Physics Letters **88**, 041112 (2006).

[35] S. Iadanza, M. Clementi, C. Hu, S. A. Schulz, D. Gerace, M. Galli, and L. O'Faolain, "Model of thermo-optic nonlinear dynamics of photonic crystal cavities," Physical Review B **102**, 245404 (2020).

[36] D. W. Hahn and M. N. Özisik, *Heat Conduction* (John Wiley & Sons, Incorporated, Somerset, United States, 2012).

[37] K. W. Park, C. Y. Park, S. Ravindran, S. J. Kang, H. Y. Hwang, Y. D. Jho, Y. R. Jo, B. J. Kim, and Y. T. Lee, "Enhancement of minority carrier lifetime of GaInP with lateral composition modulation structure grown by molecular beam epitaxy," Journal of Applied Physics **116**, 043516 (2014).

[38] J. Holzman, P. Strasser, R. Wuest, F. Robin, D. Erni, and H. Jackel, "Picosecond free-carrier recombination in indium phosphide photonic crystals," in "International Conference on Indium Phosphide and Related Materials, 2005," (IEEE, 2005), pp. 570–573.

[39] K. Kondo, M. Shinkawa, Y. Hamachi, Y. Saito, Y. Arita, and T. Baba, "Ultrafast slow-light tuning beyond the carrier lifetime using photonic crystal waveguides," Physical Review Letters **110**, 053902 (2013).

[40] P. Thiagarajan, J. Schmerge, C. S. Menoni, M. Marconi, O. E. Martinez, J. J. Rocca, M. Hafich, H. Lee, and G. Robinson, "Picosecond absorption dynamics of photoexcited ingap epitaxial films," Applied Physics Letters **59**, 90–92 (1991).

[41] S. Adachi, *Physical properties of III-V semiconductor compounds* (John Wiley & Sons, 1992).

[42] F. J. García de Abajo, "Optical excitations in electron microscopy," Reviews of Modern Physics **82**, 209 (2010).

[43] H. Fan, "Effects of free carriers on the optical properties," in "Semiconductors and Semimetals," , vol. 3 (Elsevier, 1967), pp. 405–419.

[44] B. Chen, R. Bruck, D. Traviss, A. Z. Khokhar, S. Reynolds, D. J. Thomson, G. Z. Mashanovich, G. T. Reed, and O. L. Muskens, "Hybrid photon–plasmon coupling and ultrafast control of nanoantennas on a silicon photonic chip," Nano Letters **18**, 610–617 (2018).

[45] S. S. Li, "Excess carrier phenomenon in semiconductors," in "Semiconductor physical electronics," (Springer, 2006), pp. 246–283.

[46] S. Sokolov, J. Lian, S. Combrié, A. D. Rossi, and A. P. Mosk, "Measurement of the linear thermo-optical coefficient of $Ga_{0.51}In_{0.49}P$ using photonic crystal nanocavities," Applied Optics **56**, 3219–3222 (2017).

[47] Y. A. Goldberg, *Gallium Indium Phosphide* $Ga_xIn_{1-x}P$ (World Scientific, 1999).

[48] S. Adachi, "Optical dispersion relations for GaP, GaAs, GaSb, InP, InAs, InSb, $Al_xGa_{1-x}As$, and In_{1-x} $Ga_xAs_yP_{1-y}$," Journal of Applied Physics **66**, 6030–6040 (1989).

[49] H. L. Anderson and American Institute of Physics, eds., *A Physicist's desk reference* (American Institute of Physics, New York, 1989).

[50] U. Piesbergen, "The mean atomic heats of the III-V semiconductors, AlSb, GaAs, InP, GaSb, InAs, InSb and the atomic heats of the element Germanium between 12 and 273 K," Zeitschrift für Naturforschung **18a**, 141–147 (1963).

[51] M. Levinshtein, S. Rumyantsev, and M. Shur, *Handbook Series on Semiconductor Parameters* (World Scientific, 1996).

5

Programmed all-optical switching in multistable photonic molecule with thermo-optical nonlinearity

Abstract

We demonstrate full control over the thermo-optical state of a multistable system of coupled nanoresonators on a photonic crystal (PhC) membrane, using a photomodulation principle. The phase space of the coupled PhC nanoresonators is mapped with an out-of-plane visible light pump that scans the surface and locally heats the membrane to modulate the refractive index. The most striking observation in this excitation response map is a change in the thermo-optical state of the system that remains after the pump is turned off. The excitation response map is then used to program all-optical multistable switching, where the system is excited using a microsecond pump pulse in a predetermined position. The excitation scheme walks the system through stable states of its phase space, with each step lowering or raising the internal energy of the coupled resonators, and with it, the associated output intensity of the chip. The experimental results are reproduced with a thermo-optical model with excellent agreement. We investigate the theoretical thermal distribution associated with specific energy branches of the system and find that the thermo-optical states correspond to characteristic configurations of two coupled cavities that are in a combination of hot and cold states.

5.1 Introduction

The demand for high speed and bandwidth in information transfer is tremendous and increasing. To meet this challenge, replacing electrical circuits with their optical counterparts as well as rethinking the architecture and design of networks and data centers is a must [1–8]. Development towards optical binary and multivalued computing [9–11] has stimulated research into optical devices with multistable all-optical switching capabilities. In this context, photonic crystal (PhC) membranes have attracted interest from the industry since one can design defect cavities on these platforms that have a high quality (Q) factor and small mode volume, making it easier to attain the optical nonlinearity needed for multistability [12]. Bistable nonlinear PhC resonators have long shown functionalities like all-optical switching [13–16] and all-optical memory [17,18], where low switching power, high contrast, high speed, small footprint and scalability are important aspects. Additionally, spatially overlapping coupled nonlinear modes in a PhC resonator have been demonstrated to show four wave mixing functionality [19], and PhC waveguides have exhibited slow light [20] and beam steering capabilities [21].

Resonators coupled in series form highly dispersive waveguides leading to low group velocities [22]. Coupled cavities in the shape of ring resonators, microdisks, microspheres and many other alternatives are studied for slow light applications [23] like optical buffers [24] and delay lines [25]. Amongst them, PhC nanocavities promise very low group velocities [26] which is useful for on-chip optical buffers [27,28]. In the nonlinear regime, one can take the optical bistability of a single resonator and increase the phase space to a multistable system by coupling them in series. Multistable coupled ring resonators have been studied extensively. In theoretical works they have been proposed for all-optical switches, optical memory and optical gates [29,30] and recently optical multistability has been experimentally observed in coupled ring resonators [31] and in a single microring resonator [32]. Tristability has been observed in several other optical systems such as optical fibers [33] and pillar microcavities [34]. Purposefully switching between three states has been shown for three-level atoms in a ring resonator [35,36].

In this chapter we demonstrate all-optical control of the state in a system of multistable coupled PhC nanocavities, thereby generating a multi-level 'photonic molecule' (PM) [37]. The term photonic molecule refers to a system of coupled optical resonators where the photon states resemble the electron states in the LCAO approximation in a molecule [38]. We increase the phase space by expanding the single nonlinear resonator to two coupled nonlinear resonators, providing a platform for on-chip active devices with multiple stable states [39–41]. The PhC can therefore function as a programmable multistable PM [42].

Here, we explore the phase space of the coupled nanoresonators system. We

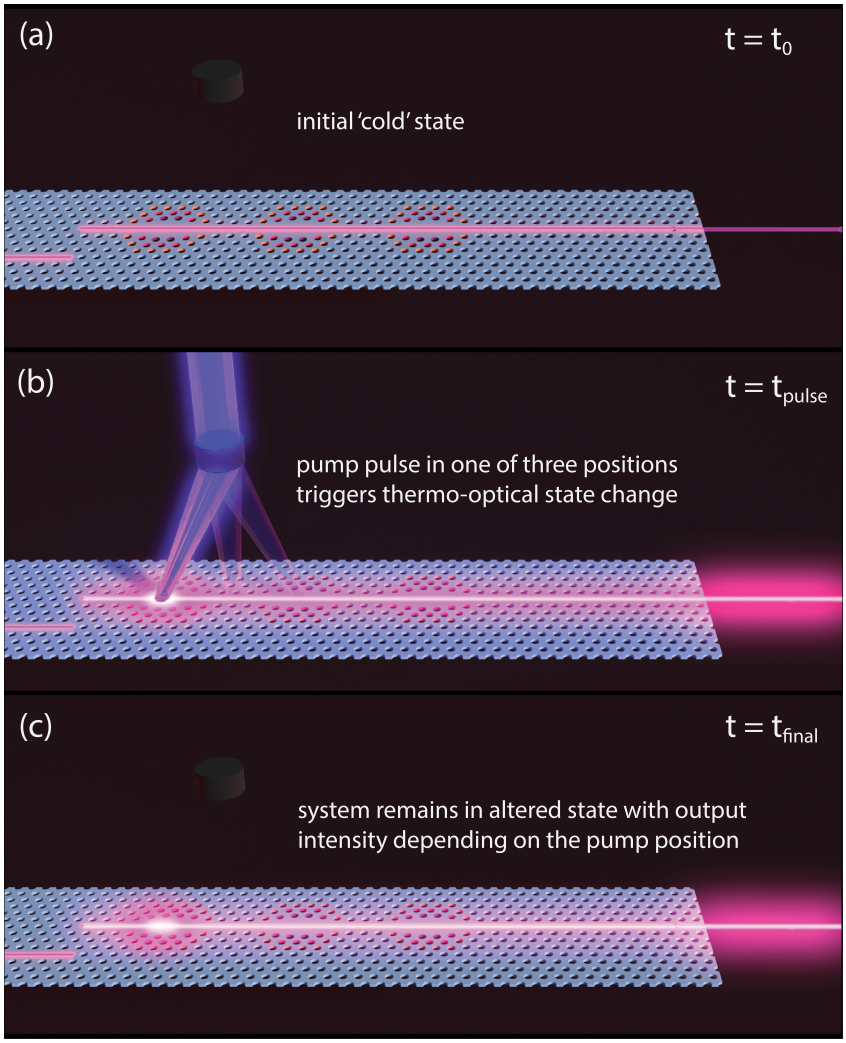

Figure 5.1: Optical multistability in coupled nanocavities. (a) We probe the coupled PhC nanocavities with in-plane input light. (b) An out-of-plane optical pump pulse at a specific position (one of three) triggers a thermo-optical state change. (c) After the pump is turned off, the thermo-optical configuration of the coupled resonators remains altered, corresponding to an altered intracavity energy and output intensity that depends on the pump position.

excite the state of the PM with a pulsed external pump beam. Optical mode manipulation of the PhC with a control beam like that has been proven useful for spectroscopy [43,44] and reconfigurable optical ports [45,46], and has been proposed for on-demand cavity formation [47]. In this case, we use it to all-optically write and store the optical state on-demand.

In Fig. 5.1 we illustrate the concept of the experiment. The output intensity of the PhC is determined by the thermo-optical configuration of the first two coupled cavities. Switching between states is achieved by spatial photomodulation with the pump pulse, addressing one or both cavities. Local heating by the pump pulse changes the refractive index and detunes the cavity resonances. This triggers a thermo-optical state change that stabilizes in the desired state. The PM remains in the altered state after the pump pulse is off.

5.2 Experimental Setup

In Fig. 5.2 we present the geometrical and spectral properties of our PhC. Fig. 5.2(a) shows a rendering of our PhC, a 180 nm-thin $Ga_{0.51}In_{0.49}P$ (InGaP) slab with a hexagonal air hole pattern. There are two access waveguides, one on either side of the slightly narrower barrier waveguide, for injection of input light and extraction of transmission light. Three mode-gap resonators are situated on the barrier waveguide in series, light reaches the resonators through evanescent coupling between injection waveguide and barrier waveguide. The mode-gap resonators consist of a subtle width-modulation of the barrier waveguide creating a local defect. Perpendicular to the PhC membrane we have a 405 nm pump beam that we can focus anywhere on the PhC surface to do spatial scans. We use it to scan over the barrier waveguide, as depicted in Fig. 5.2(b), while probing with the NIR input light.

Fig. 5.2(c) shows an NIR wavelength sweep (pump light is off) to find the 'cold' resonance wavelength of the cavities using low NIR power. We then increase the NIR power to induce optical nonlinearity, leading to the spectra shown in Fig. 5.2(d), where the output intensity depends on the sweep direction due to hysteresis. We note here that the resonance of the third cavity cannot be observed directly without using the pump, since the coupling between input waveguide and third cavity is negligible. The third cavity only becomes visible when it is coupled to the other resonances by the pump.

In Fig. 5.3(a) we show a mode map of the PhC. It shows the out-of-plane scattered light from the resonators while a CW pump of low power is scanning over the waveguide (see Fig. 5.2(b)) with the pump position on the horizontal axis and the wavelength of the NIR probe light on the vertical axis. The pump redshifts the cavity resonance due to the thermo-optic effect when there is overlap between the optical mode profile of the cavity and the thermal profile of the

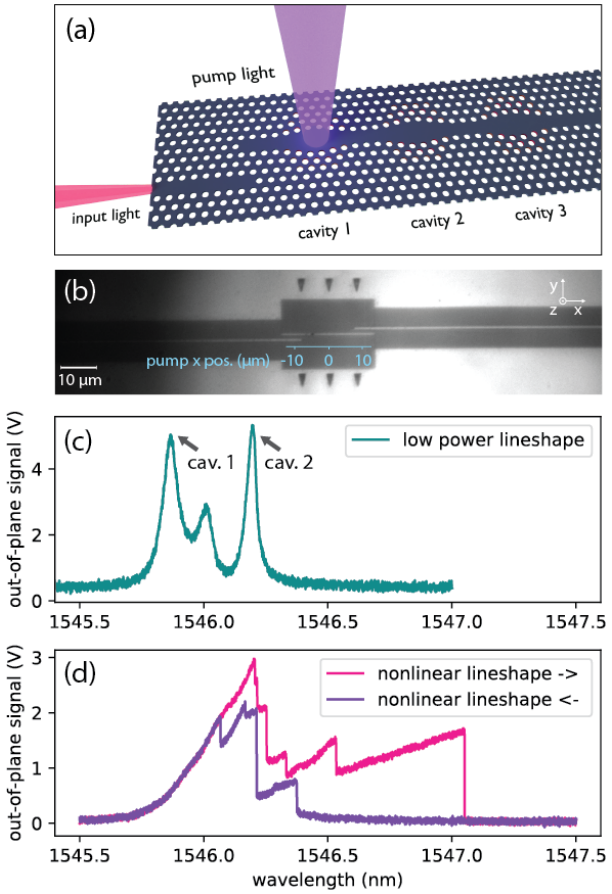

Figure 5.2: Details of the PhC and characterization of the resonators. (a) Rendering of the PhC with three cavities formed by waveguide width modulation. The air hole displacement is exaggerated for readability. NIR laser light enters via the injection waveguide and couples evanescently to the resonators. A visible-light pump beam, perpendicular to the PhC slab, is scanned over the surface. (b) CCD image of the PhC. (c) Wavelength scan at low NIR input power. (d) Forward and backward wavelength scans at high NIR input power.

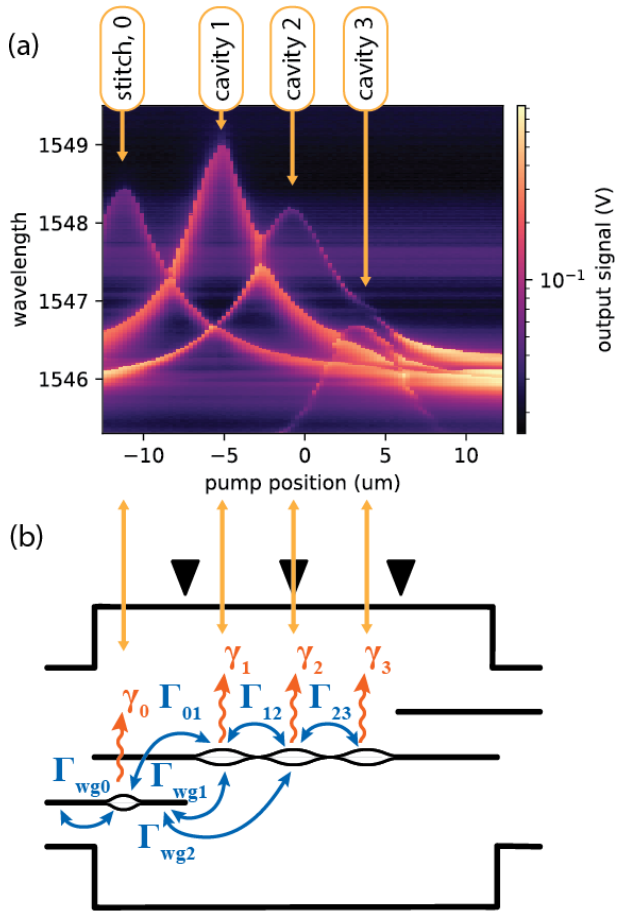

Figure 5.3: Details of the PhC and characterization of the resonators. (a) Mode map of PhC made with a line scan over the waveguide. On the x-axis we plot the pump position, on the y-axis the input wavelength, the color scale indicates the out-of-plane scattered light intensity normalized by its maximum. All cavities are labeled in correspondence with (b). (b) Schematic of the coupled cavities. Laser light enters via the waveguide on the left and couples directly to the stitch mode (0) and evanescently to the cavities (1, 2, 3) with the indicated coupling rates (Γ). Loss rates are indicated with γ.

pump spot, and an additional term due to free carrier absorption appears when the optical pump spot itself overlaps with the cavity (see Chapter 4). As a result a peak is observed in the mode map when the pump beam hits a cavity, a spectroscopy method that is enhanced by the high Q factor of the resonators. The details of this nonlinear mode mapping technique are described in Chapter 4.

With the mode map we determine the position and coupling between the cavities. The resonance-shift is largest when the pump overlaps with the cavity mode profile, while the avoided crossings indicate the coupling strengths. We identify four resonators, as an unintentional resonance arises from a stitch defect resulting from the electron-beam lithography process [48–50]. The third waveguide cavity becomes visible when the pump beam tunes it close to resonance with the central cavity. Clearly, there is strong coupling between adjacent cavities, as can be observed from the avoided crossing of their resonances.

Fig. 5.3(b) shows a schematic representation of the theoretical model depicting the PhC cavities and waveguides, including all coupling- and loss rates. All of these elements are implemented in a system of coupled-mode equations to find the spectral information. These optical equations are coupled with the thermal properties of the PhC through the heat equation and the spatial distribution of the optical mode profiles of the resonators. We treat the coupled-mode theory in detail in Appendix 5.5 and the connected heat equation in Chapter 1.5.

5.3 Results

Excitation Response Map

In Fig. 5.4 we present the pump scheme we use to generate the excitation response maps. We monitor the output signal while we bring the system into different states using a pump pulse. The pump scheme consists of four phases: we initialize at a specific input wavelength, then give a pump pulse at the pump position ($t = 0$), we keep monitoring the out-of-plane scattered intensity post-pump, after which we reset the system to its initial state by interrupting the input signal by dipping probe intensity to zero ($t = 8.5$ ms). For every phase we take the time-average of the output signal monitored via the out-of-plane scattered light.

In Fig. 5.5 we show the excitation response maps of the PhC. They are generated by plotting the time-averaged output signal, normalized to the maximum intensity, against pump position and input wavelength for each phase.

Fig. 5.5(a) shows the response map of the initial state. For each wavelength we average over 500 μs. The data for the initial state is taken before the arrival of the pump pulse, therefore we see each resonance at a fixed wavelength independent of pump position. These are the resonances in their 'cold' state.

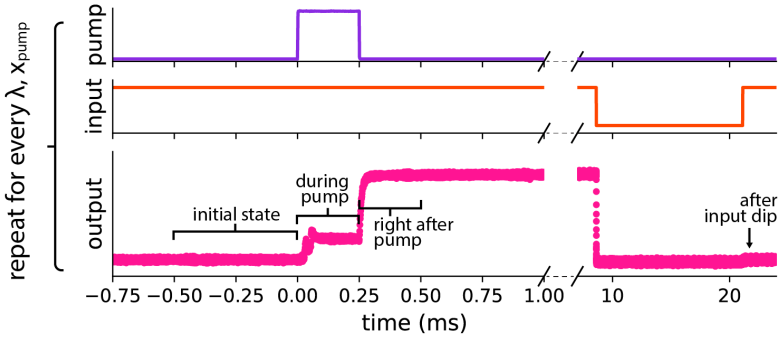

Figure 5.4: The pump pulse procedure consisting of: a 250 μs pump pulse at t=0 at a specific pump position, a waiting period, and then an interruption of the input signal. The resulting output signal is time averaged for each phase of the procedure as indicated: initial state, during pump, right after pump, after input interruption.

In Fig. 5.5(b) we show the excitation response map of the pumped state. We average the output signal over the entire pump duration of 250 μs. We observe a redshift whenever there is overlap between pump and optical mode profile of a resonance. As in the mode map of Fig. 5.3(a), this map shows the position of the three cavities and the stitch mode due to the pump induced redshift of the resonances, as well as the avoided crossings between resonances indicating the coupling strengths. Difference between Fig. 5.3(a) and Fig. 5.5(b) is an increased NIR input power for the latter.

In Fig. 5.5(c) we show the excitation response map of the post-pump state. Right after the pump pulse ($t = 250$ μs) we average the signal for 250 μs. Importantly, the post-pump state does not return to the initial state after the pump is switched off. Depending on pump position the coupled cavities end up in high-, mid-, or low-intensity states which are stable for times much larger than the typical thermal response time of 7-10 μs (see Chapter 3). The contours of the different intensity areas match the optical mode profiles of Fig. 5.5(b). We recognize the excited states of the left and center cavity with their own intensity areas, and a very intense overlapping area where the two cavities meet in an excited state of hybridized cavities. For this excited hybridized state, we observe horizontal ribbons of intensity variations in the direction of the pump line scan. The measurement is setup such that for each parked wavelength the pump takes a line scan over the waveguide in consecutive steps. The meta-stability indicates high sensitivity to any disturbance like input intensity variations, nearby dark

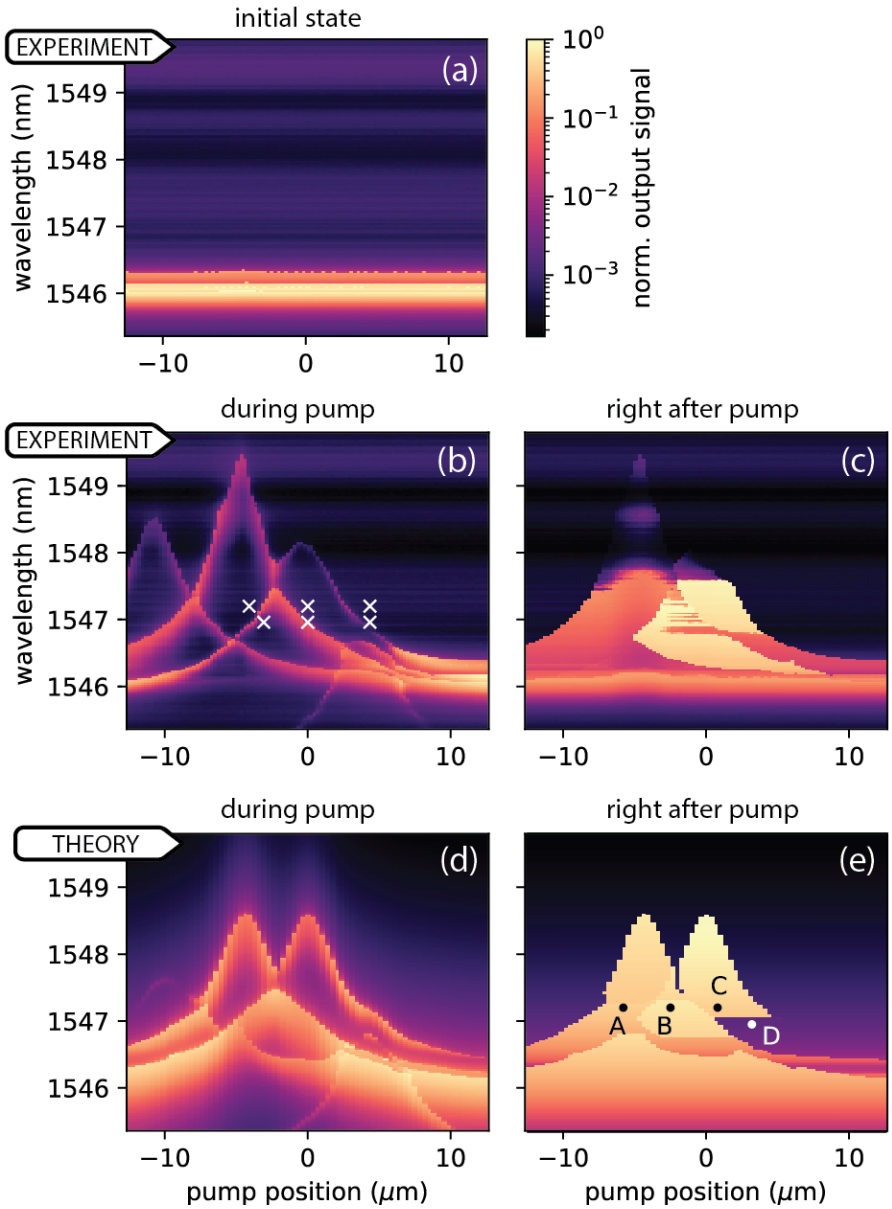

Figure 5.5: Excitation response maps. ... full caption on next page

Figure 5.5: Figure on previous page
... Excitation response maps demonstrating multistability, with on the x-axis the pump position (x_{pump}), on the y-axis the input wavelength (λ_p), and the color map indicating the out-of-plane scattered light normalized to the maximum intensity for each map. The maps result from the pump procedure measurements at certain λ_p and x_{pump} depicted in Fig. 5.4. Every (λ_p, x_{pump}) pixel is the time-average of the out-of-plane intensity at the corresponding pump scheme phase: (a) the initial state before the pump pulse, (b) the state during the pump pulse and (c) the state right after the pump pulse. In (f) and (g) the theoretically generated pumped- and post pump- excitation response map respectively. White $\times$ indicates pump pulse position in switch experiment. Letters A, B, C, D indicate the states for which we render the temperature profiles.

modes, interference fringes in the background and temperature fluctuations.

As a control measurement, we plot the reset map in Appendix 5.7, for which we average 250 μs right after the input interruption, together with the initial state. It reproduces the initial state, demonstrating that the pump procedure has not affected the PhC permanently, for instance through oxidation.

In Fig. 5.5(d,e) we plot the theoretical excitation response maps of the pumped (d) and post-pump (e) phase generated with our TO model (see Appendix 5.5 Eqns. (5.1) and (5.2)). The precise shape of the excitation response map, for both the theoretical and experimental case, is highly dependent on several parameters such as the input power in the waveguide, the effective pump power, and the coupling strengths between the input waveguide and the cavities. We have chosen values for these parameters where good agreement with the data is observed. The coupling strengths we use ($\lambda_{ij} = \{125, 250, 27.3\}$ pm) are consistent with the avoided crossings as measured in the mode map (Fig. 5.3(a)). The input and pump power used are on the expected order of magnitude for the effective power reaching the resonators. We refer to Appendix 5.6 for a table of the parameters we use in the theoretical maps.

For the theoretical intensity during the pump, in Fig. 5.5(d), we see a pump induced redshift of the resonances revealing the optical mode profiles of the cavities and the stitch mode, as well as the avoided crossings for coupled resonators. In Fig. 5.5(e), the theoretical post-pump response map, we observe an altered state that remains after the pump is turned off with several areas of different output intensity. Contours of these areas are determined by the optical mode profiles as observed in (d), with an highly intense area where the two cavities overlap. The shapes of these areas as well as the positions relative to the bare resonances match the experimental results very well. We remark that the high-intensity peaks of the left and central cavity remain stable far into redshifted resonances

for the model, unlike the experimental observation where these highly detuned states are highly sensitive to drift and/or disturbances. Lastly, we note that we observe a larger pump detune for the first cavity than for the other cavities, we explain this by the increased local absorption as can be seen in Fig. 5.2(b) as a small dark spot on top of the first cavity, possibly caused by prolonged exposure to localized probe and/or pump light. Yet, the qualitative similarity between the model and the experimental results show that our model captures the essential physics.

Since the model captures the essential physics we can use it to investigate quantities that were not directly measured. The multistability of the coupled resonators is based on thermo-optical nonlinearity, therefore we take a look at the thermal profiles associated with the different optical states.

In Fig. 5.6 we show the temperature profiles of the different states that were observed for the indicated locations A, B, C, D, on the post-pump excitation response map in Fig. 5.5(e). We see that the different output intensities correspond to different temperature distributions. We observe a thermal profile with a hot left and hot center cavity that is either symmetrically distributed over the two cavities (Fig. 5.6(a)), has its thermal weight on the left cavity (Fig. 5.6(b)), has its thermal weight on the center cavity (Fig. 5.6(c)), or a thermal profile where all cavities are cold (Fig. 5.6(d)). In Fig. 5.6(e) we plot the horizontal cross sections of the thermal profiles (note that the cross section of D is multiplied by 10 for readability). It confirms that the states A, B and C are hybridized states of the left and center cavity, where higher intracavity energy correspond to higher temperature. Indeed, the four different output intensities are associated with four different configurations of the two hybridized cavities with three distinct 'on' states and an 'off' state.

The temperature profiles support the hypothesis that the observed multistability of the PM involves the thermo-optical state of only two coupled cavities, and that switching between states can be done by local thermal tuning of either cavity or the coupling between them, changing the thermal profile of the state and thus the optical output.

Programmed Switching Between Multiple Stable States

We use the information of Fig. 5.5 to estimate the input wavelength and pump positions needed to switch between three stable intensity levels of the coupled cavity system. Fig. 5.7(a) shows a histogram of the data of Fig. 5.5(d) where all output intensity states are binned, regardless of pump position, and plotted against wavelength. We observe up to five branches of stable states between 1546.03 and 1547.73 nm, indicating a wide region of optical multistability. We select two wavelengths for which we can reach at least three different intensity

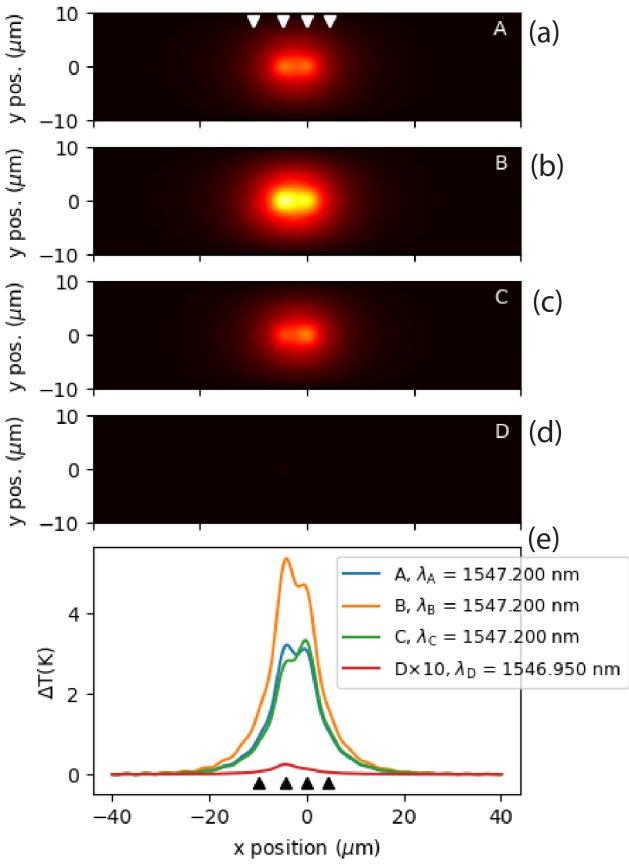

Figure 5.6: Temperature profiles inside the different intensity areas as indicated in the theoretical excitation response map of Fig. 5.5(g) with A, B, C and D. The horizontal cross section of the profiles over the center line ($y = 0$) is plotted in the bottom panel, where the cross section of D is multiplied by 10 for readability. Triangles indicate the x-position of each cavity, marking from left to right the stitch, first, center and right cavity.

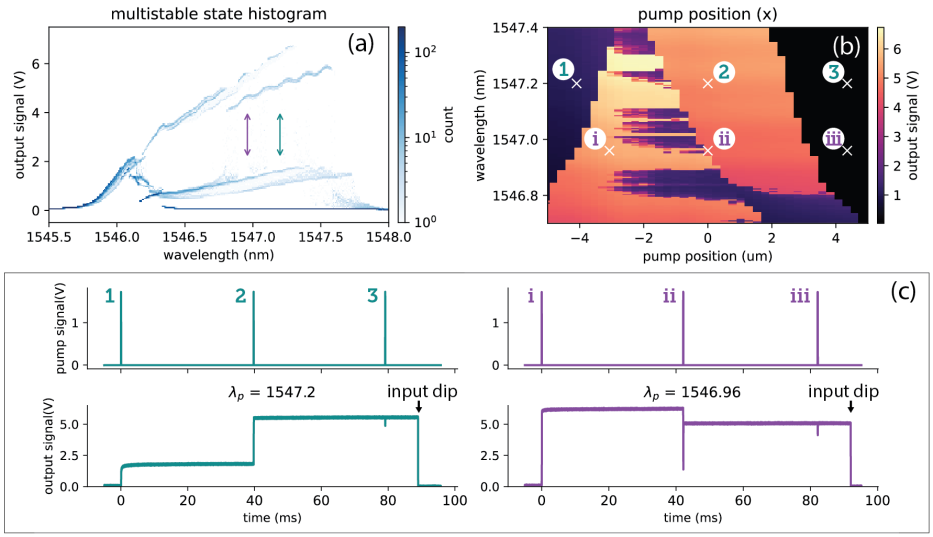

Figure 5.7: All-optical switch between multiple stable states: we switch the system of coupled cavities between three stable intensity areas by use of optical pump pulse in specific positions. (a) A histogram of the data of Fig. 5.5(d) showing up to five branches of stable states between between 1546.03 and 1547.73 nm. For all pump positions of Fig. 5.5(d) the output intensities where binned and plotted against wavelength. We indicate two wavelengths selected for multistable switching: $\lambda_p = 1546.96$ (purple arrow) and $\lambda_p = 1547.20$ (green arrow). (b) A zoom selection of Fig. 5.5(d) indicating the three pump positions (white $\times$) we use to make the multistable switch at each wavelength: pump pulse positions 1, 2 and 3 (green) for $\lambda_p = 1547.20$ and pump pulse positions i, ii and iii (purple) for $\lambda_p = 1546.96$. (c) Switch signal: the output signal and pump signal are plotted for $\lambda_p = 1547.20$ (left) and $\lambda_p = 1546.96$ (right).

branches: $\lambda_p = 1547.20$ and $\lambda_p = 1546.96$. Fig. 5.7(b) shows a zoom selection of Fig. 5.5(d) where for each λ_p we indicate three pump positions inside different intensity areas. The same pump positions are marked in Fig. 5.5(b). The pulses are placed on top of cavity one (1), two (2, ii) or three (3, iii), or placed inside the overlapping area between cavity one and two (i). We have reported before that the thermo-optical time constant of the coupled cavity system is on the order of a few microseconds (see Chapter 3), therefore we use a 50 μs pump pulse to give the system enough time to reach thermal equilibrium during the pulse.

Fig. 5.7(c) shows the response of the coupled cavities to the pump pulses. We initialize in the dark state at the wavelength $\lambda_p = 1547.20$ nm and then pump the first cavity, the resulting output signal jumps to a mid-intensity stable state. The second pump pulse on top of the second cavity brings the signal to a high-intensity state. The third pump is observed in a short dip in the output signal, but it does not cool the system down to its initial dark state, thus we return to the initial state right after the input light has been interrupted. Possibly, cooling of the coupled modes by thermo-optical tuning with the pump is less effective because detuning the resonances does lower the intracavity energy, but at the same time the pump beam locally heats the PhC.

We then park the input light wavelength at $\lambda_p = 1546.96$ nm to demonstrate a pump series that shoots the system from a higher to a lower intensity state, *i.e.*, to demonstrate it is possible to pump-switch to a cooler state. We set the first pump positions inside the highest intensity area, between the two cavities, to shoot the system into the upper intensity branch with the first pump pulse. The second pulse brings the system into a slightly lower intensity (the same branch we saw for $\lambda_p = 1547.20$ nm with the pump on top of the second cavity). Like before, the third pulse is observed as a dip in the signal but does not push the system to a steady dark state, and lastly, the input interruption resets the system. This experiment shows that we can move through the state space of our multistable nonlinear system and address specific states, lowering or raising the internal energy.

5.4 Conclusion

We demonstrate programmed all-optical switching in a PhC coupled nanoresonators system, jumping between steady states of the optically multistable PM by spatial photomodulation. A pump pulse excites the PM by thermal detuning the resonance of the addressed resonator(s), leading to thermo-optical locking of the coupled-modes in a particular thermo-optical configuration and corresponding intensity branch. In this way we explore the phase space of the system. We step through different states with higher or lower internal energy, programming the optical output of the system. Results were qualitatively reproduced with

a thermo-optical model, and confirm the thermal configurations of two coupled cavities in this optically multistable system.

The multistable all-optical switch may finds its way to tunable filters, optical ternary or quarternary logic gates [7], and applications that convert spatial information into intensity modulation like sensors, free-space optics, or PhC spatial light modulators [51].

5.5 Appendix A: Theoretical model

We express the coupled resonators in a system of differential equations using coupled mode theory as follows. The time evolution of the amplitude $A_i(t)$ for each resonator i is expressed in the matrix equation as $d\mathbf{A}/dt = \mathbf{MA} + F\mathbf{S}$, where $\mathbf{M}$ is the coupling matrix, $\mathbf{A}$ is the amplitude vector, $\mathbf{S}$ is the input array that represents the optical drive via the waveguide, and the prefactor F is the driving amplitude determined by the input power. All coupling rates, loss terms and driving forces depicted in Fig 5.3(b) are taken into account, such that

$$\mathbf{M} = -\begin{bmatrix} i\omega_0 + \gamma_0' & i\Gamma_{01} + \sqrt{\Gamma_{\mathrm{wg}0}\Gamma_{\mathrm{wg}1}} & \sqrt{\Gamma_{\mathrm{wg}0}\Gamma_{\mathrm{wg}2}} & 0 \\ i\Gamma_{01} + \sqrt{\Gamma_{\mathrm{wg}0}\Gamma_{\mathrm{wg}1}} & i\omega_1 + \gamma_1' & i\Gamma_{12} + \sqrt{\Gamma_{\mathrm{wg}1}\Gamma_{\mathrm{wg}2}} & 0 \\ \sqrt{\Gamma_{\mathrm{wg}0}\Gamma_{\mathrm{wg}2}} & i\Gamma_{12} + \sqrt{\Gamma_{\mathrm{wg}1}\Gamma_{\mathrm{wg}2}} & i\omega_2 + \gamma_2' & i\Gamma_{23} \\ 0 & 0 & i\Gamma_{23} & i\omega_3 + \gamma_3' \end{bmatrix}, \tag{5.1}$$

$$\mathbf{S} = \begin{bmatrix} \sqrt{2\Gamma_{\mathrm{wg}0}} \\ \sqrt{2\Gamma_{\mathrm{wg}1}} \\ \sqrt{2\Gamma_{\mathrm{wg}2}} \\ 0 \end{bmatrix} \tag{5.2}$$

where ω_i is the frequency and γ_i' the total loss rate of cavity i. Γ_{ij} is the coupling rate between cavities i and j, and $\Gamma_{\mathrm{wg}i}$ the coupling rate between the input waveguide and cavity i. The intrinsic loss rate γ_i is included in the experimentally measured loss rate γ_i' such that $\gamma_i' = \gamma_i + \Gamma_{ij}$ for all adjacent resonators j. We then solve the matrix equation for $d\mathbf{A}/dt = -i\omega\mathbf{A}$ with ω the driving frequency.

The coupled-mode equations are related to the temperature profiles of the cavities by the thermo-optic effect. Therefore we find solutions for the system by relating the coupled-mode equations to the heat equations of the PhC as we described previously in Chapters 3 and 4. The optical mode profile for each resonator is taken from FDTD calculation for the mode-gap resonator as designed. The same mode profile was used to simulate the presence of a stitch mode.

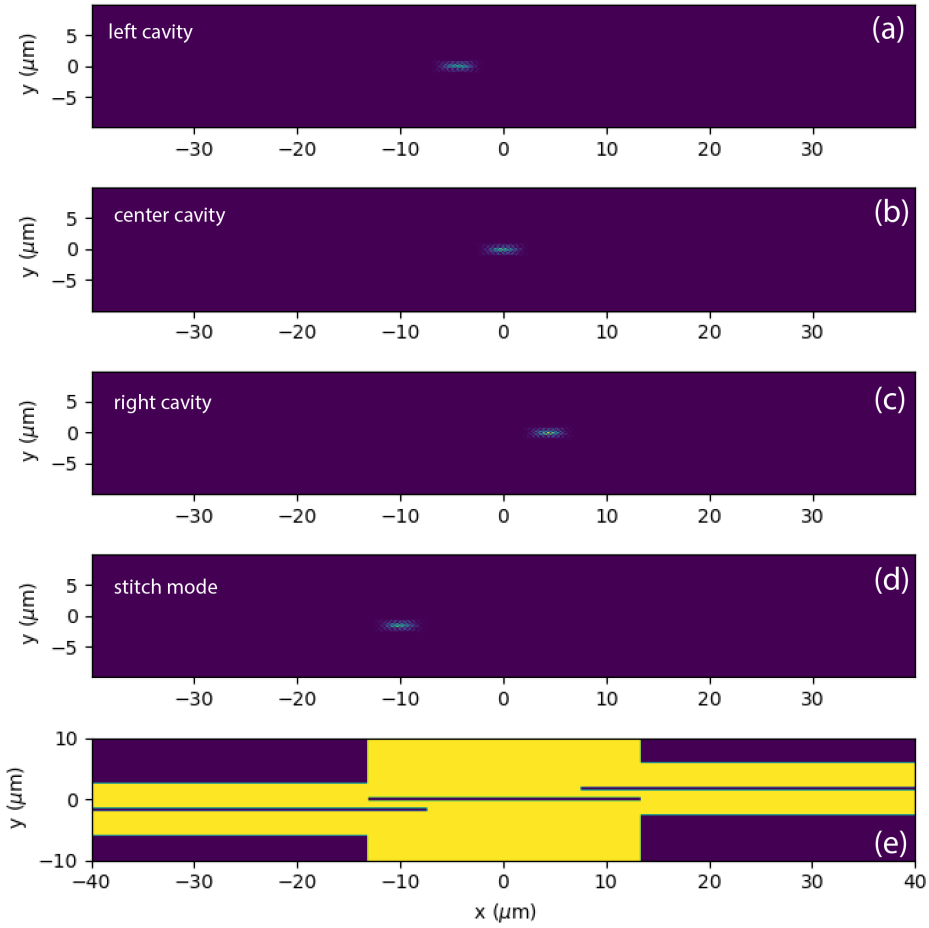

Figure 5.8: (a-d) FDTD calculated mode profile for the resonators that we use as input for our TO model. (e) Fill fraction mask used in the model to simulate the 2D specific heat.

5.6 Appendix B: Simulation Parameters

Tables 5.1 and 5.2 shows the parameters and constants we use to generate the theoretical excitation response maps of Fig. 5.5(f,g) and thermal profiles of Fig. 5.6. We determine the effective loss rate γ_i' by the fitted the linewidth $\Delta\lambda_i$ of the resonance lineshape and using $\gamma_i' = \Delta\omega_i/2$. In that same way, the coupling Γ_{ij} between cavities i, j is taken from the avoided crossing $\Delta\lambda_{ij}$ using $\Gamma_{ij} = \Delta\omega_{ij}/2$.

Table 5.1: (Part.I) Constants and parameters used to generate the theoretical excitation response maps of Fig. 5.5(f,g) and thermal profiles of Fig. 5.6.

Constants and parameters used in the model

	symbol	value	source
refractive index	n	3.06	[52]
thermal conductivity of GaInP	$\kappa_{Ga_{0.51}In_{0.49}P}$	4.9 W/m.K	[53]
thermal conductivity of N_2	κ_{N_2}	0.024 W/m.K	[54]
specific heat of GaInP	C_{sp}	310 J/K.kg	[55]
density of GaInP	ρ	4810 kg/m^3	[56]
thickness of the PhC membrane	h	180 nm	
filling fraction	$\phi(x,y)$	0.714 (PhC membrane)	
		1.0 (waveguide, bulk)	
2D specific heat	$C_{2D}(\phi(x,y))$	$h\phi(x,y)\rho C_{sp}$	
thermo-optical coefficient	$\eta = dT/dn$	-2×10^{-4} K^{-1}	[57]
NIR input power	F^2	169 μW	fit parameter
absorption fraction of NIR input light	α_{PrA}	0.05	estimated value
VIS pump power		17.5 μW	fit parameter
FWHM of the pump in (x,y)-direction		(588, 567) nm	experimentally measured
absorption fraction of pump	β_{PuA}	1.0 (PhC membrane)	
		0.2 (waveguide)	fit parameter
carrier lifetime	τ_c	0.4 ns	Chapter 4

Table 5.2: (Part.II) Constants and parameters used to generate the theoretical excitation response maps of Fig. 5.5(f,g) and thermal profiles of Fig. 5.6.

Constants and parameters used in the model

	symbol	value	source
resonance wavelength stitch mode	λ_0	1546.010 nm	fit parameter
resonance linewidth stitch mode	$\Delta\lambda_0$	85 pm	fit parameter
resonance wavelength cavity 1	λ_1	1545.967 nm	experimentally measured
resonance linewidth cavity 1	$\Delta\lambda_1$	85 pm	experimentally measured
resonance wavelength cavity 2	λ_2	1546.090 nm	experimentally measured
r esonance linewidth cavity 2	$\Delta\lambda_2$	52 pm	experimentally measured
resonance wavelength cavity 3	λ_3	1544.800 nm	fit parameter
resonance linewidth cavity 3	$\Delta\lambda_3$	85 pm	fit parameter
coupling between stitch mode and cavity 1	λ_{01}	125 pm	fit parameter
coupling between cavity 1 and 2	λ_{12}	250 pm	fit parameter
coupling between cavity 2 and 3	λ_{23}	27.3 pm	fit parameter
coupling between waveguide and stitch mode	λ_{wg0}	0.78 pm	fit parameter
coupling between waveguide and cavity 1	λ_{wg1}	39 pm	fit parameter
coupling between waveguide and cavity 2	λ_{wg2}	19.5 pm	fit parameter

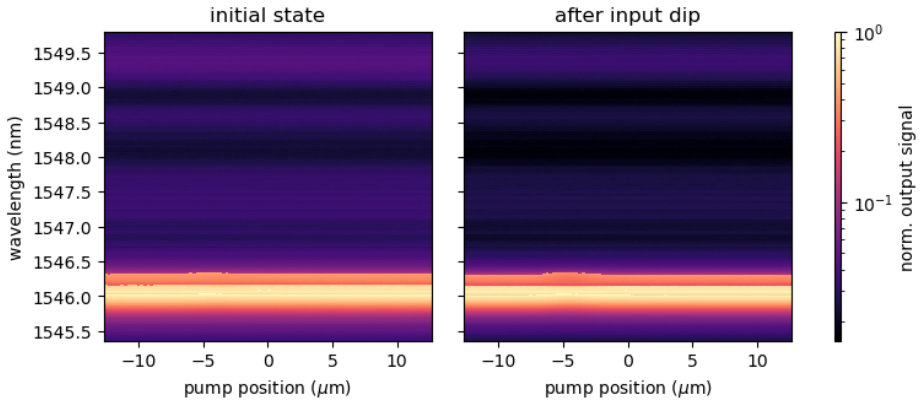

Figure 5.9: Excitation response maps for the initial state (left) and post reset state (right). On the x-axis we plot pump position. On the y-axis we plot input wavelength. The colormap is the out-of-plane scattered light normalized to the maximum signal of each map. The initial state is measured before the excitation pump is turned on. The reset state is measured after an iterruption of the NIR input power.

5.7 Appendix C: Response Map After Reset

In Fig. 5.8 we plot the initial response map, before optical pump excitation, next to the excitation response map after the reset by the NIR input interruption (see Fig. 5.4). It demonstrates that the excitation has not permanently changed or damaged the PhC.

5.8 References

[1] C. Kachris, K. Bergman, and I. Tomkos, *Optical interconnects for future data center networks* (Springer Science & Business Media, 2012).

[2] C. Qiu, H. Xiao, L. Wang, and Y. Tian, "Recent advances in integrated optical directed logic operations for high performance optical computing: a review," Frontiers of Optoelectronics **15**, 1–17 (2022).

[3] J. J. Singh, D. Dhawan, and N. Gupta, "All-optical photonic crystal logic gates for optical computing: an extensive review," Optical Engineering **59**, 110901 (2020).

[4] S. Xiang, Y. Han, Z. Song, X. Guo, Y. Zhang, Z. Ren, S. Wang, Y. Ma, W. Zou, B. Ma *et al.*, "A review: Photonics devices, architectures, and algorithms for optical neural computing," Journal of Semiconductors **42**, 023105 (2021).

[5] C. Li, X. Zhang, J. Li, T. Fang, and X. Dong, "The challenges of modern computing and new opportunities for optics," PhotoniX **2**, 1–31 (2021).

[6] A. Biberman and K. Bergman, "Optical interconnection networks for high-performance computing systems," Reports on Progress in Physics **75**, 046402 (2012).

[7] S. B. Jo, J. Kang, and J. H. Cho, "Recent advances on multivalued logic gates: a materials perspective," Advanced Science **8**, 2004216 (2021).

[8] B. Mukherjee, "WDM optical communication networks: progress and challenges," IEEE Journal on Selected Areas in Communications **18**, 1810–1824 (2000).

[9] H. Wang, S. Ouyang, Y. Shen, and X. Chen, "Ternary optical computer: An overview and recent developments," in "2021 12th International Symposium on Parallel Architectures, Algorithms and Programming (PAAP)," (IEEE, 2021), pp. 82–87.

[10] C. Taraphdar, T. Chattopadhyay, and J. N. Roy, "Designing of an all-optical scheme for single input ternary logical operations," Optik **122**, 33–36 (2011).

[11] T. Chattopadhyay and J. N. Roy, "All-optical quaternary computing and information processing: a promising path," Journal of Optics **42**, 228–238 (2013).

[12] T. Alexoudi, G. T. Kanellos, and N. Pleros, "Optical RAM and integrated optical memories: a survey," Light: Science & Applications **9**, 1–16 (2020).

[13] K. Nozaki, T. Tanabe, A. Shinya, S. Matsuo, T. Sato, H. Taniyama, and M. Notomi, "Sub-femtojoule all-optical switching using a photonic-crystal nanocavity," Nature Photonics **4**, 477–483 (2010).

[14] A. M. Morsy, R. Biswas, and M. L. Povinelli, "High temperature, experimental thermal memory based on optical resonances in photonic crystal slabs," APL Photonics **4**, 010804 (2019).

[15] Q. Saudan, D. A. Bekele, G. Dong, Y. Yu, K. Yvind, J. Mørk, and M. Galili, "Crosstalk-free all-optical switching enabled by Fano resonance in a multimode photonic crystal nanocavity," Optics Express **30**, 7457–7466 (2022).

[16] M. Notomi, A. Shinya, S. Mitsugi, G. Kira, E. Kuramochi, and T. Tanabe, "Optical bistable switching action of Si high-Q photonic-crystal nanocavities," Optics Express **13**, 2678–2687 (2005).

[17] E. Kuramochi, K. Nozaki, A. Shinya, K. Takeda, T. Sato, S. Matsuo, H. Taniyama, H. Sumikura, and M. Notomi, "Large-scale integration of wavelength-addressable all-optical memories on a photonic crystal chip," Nature Photonics **8**, 474 – 481 (2014).

[18] K. Nozaki, A. Shinya, S. Matsuo, Y. Suzaki, T. Segawa, T. Sato, Y. Kawaguchi, R. Takahashi, and M. Notomi, "Ultralow-power all-optical RAM based on nanocavities," Nature Photonics **6**, 248–252 (2012).

[19] G. Marty, S. Combrié, F. Raineri, and A. De Rossi, "Photonic crystal optical parametric oscillator," Nature Photonics **15**, 53–58 (2021).

[20] H. Gersen, T. J. Karle, R. J. P. Engelen, W. Bogaerts, J. P. Korterik, N. F. van Hulst, T. F. Krauss, and L. Kuipers, "Real-space observation of ultraslow light in photonic crystal waveguides," Physics Review Letters **94**, 073903 (2005).

[21] D. Vercruysse, N. V. Sapra, K. Y. Yang, and J. Vuckovic, "Inverse-designed photonic crystal circuits for optical beam steering," ACS Photonics **8**, 3085–3093 (2021).

[22] A. Yariv, Y. Xu, R. K. Lee, and A. Scherer, "Coupled-resonator optical waveguide: a proposal and analysis," Optics Letters **24**, 711–713 (1999).

[23] F. Morichetti, C. Ferrari, A. Canciamilla, and A. Melloni, "The first decade of coupled resonator optical waveguides: bringing slow light to applications," Laser Photonics Review **6**, 74–96 (2012).

[24] F. Xia, L. Sekaric, and Y. Vlasov, "Ultracompact optical buffers on a silicon chip," Nature Photonics **1**, 65–71 (2007).

[25] J. K. Poon, J. Scheuer, Y. Xu, and A. Yariv, "Designing coupled-resonator optical waveguide delay lines," JOSA B **21**, 1665–1673 (2004).

[26] M. Notomi, E. Kuramochi, and T. Tanabe, "Large-scale arrays of ultrahigh-Q coupled nanocavities," Nature Photonics **2**, 741 – 747 (2008).

[27] M. Nakadai, T. Asano, and S. Noda, "Electrically controlled on-demand photon transfer between high-q photonic crystal nanocavities on a silicon chip," Nature Photonics **16**, 113–118 (2022).

[28] H. Takesue, N. Matsuda, E. Kuramochi, W. J. Munro, and M. Notomi, "An on-chip coupled resonator optical waveguide single-photon buffer," Nature Communications **4**, 1–7 (2013).

[29] S. Zhang, J. Li, R. Yu, W. Wang, and Y. Wu, "Optical multistability and Fano line-shape control via mode coupling in whispering-gallery-mode microresonator optomechanics," Scientific Reports **7**, 1–12 (2017).

[30] Y. Dumeige and P. Féron, "Dispersive tristability in microring resonators," Physical Review E **72**, 066609 (2005).

[31] L. Jin, L. Di Lauro, A. Pasquazi, M. Peccianti, D. J. Moss, R. Morandotti, B. E. Little, and S. T. Chu, "Optical multi-stability in a nonlinear high-order microring resonator filter," APL Photonics **5**, 056106 (2020).

[32] D. Gray, R. Hamerly, M. Namdari, M.-T. Cătuneanu, K. Jamshidi, N. Bogdanowicz, and H. Mabuchi, "Thermo-optic multistability and relaxation in silicon microring resonators with lateral diodes," Physical Review Applied **14**, 024073 (2020).

[33] I. A. Temnykh, N. F. Baril, Z. Liu, J. V. Badding, and V. Gopalan, "Optical multistability in a silicon-core silica-cladding fiber," Optics express **18**, 5305–5313 (2010).

[34] S. Rodriguez, A. Amo, I. Sagnes, L. Le Gratiet, E. Galopin, A. Lemaître, and J. Bloch, "Interaction-induced hopping phase in driven-dissipative coupled photonic microcavities," Nature Communications **7**, 1–6 (2016).

[35] J. Sheng, U. Khadka, and M. Xiao, "Realization of all-optical multistate switching in an atomic coherent medium," Physical Review Letters **109**, 223906 (2012).

[36] Y.-N. Li, Y.-Y. Chen, R.-G. Wan, and H.-W. Yan, "Dynamical switching and memory via incoherent pump assisted optical bistability," Physics Letters A **383**, 2248–2254 (2019).

[37] S. V. Boriskina, "Photonic molecules and spectral engineering," Photonic microresonator research and applications pp. 393–421 (2010).

[38] D. J. Griffiths and D. F. Schroeter, *Introduction to quantum mechanics* (Cambridge university press, 2018).

[39] K. Liao, X. Hu, T. Gan, Q. Liu, Z. Wu, C. Fan, X. Feng, C. Lu, Y.-c. Liu, and Q. Gong, "Photonic molecule quantum optics," Advances in Optics and Photonics **12**, 60–134 (2020).

[40] M. Bayer, T. Gutbrod, J. Reithmaier, A. Forchel, T. Reinecke, P. Knipp, A. Dremin, and V. Kulakovskii, "Optical modes in photonic molecules," Physical Review Letters **81**, 2582 (1998).

[41] S. Haddadi, A. Yacomotti, I. Sagnes, F. Raineri, G. Beaudoin, L. Le Gratiet, and J. Levenson, "Photonic crystal coupled cavities with increased beaming and free space coupling efficiency," Applied Physics Letters **102**, 011107 (2013).

[42] M. Zhang, C. Wang, Y. Hu, A. Shams-Ansari, T. Ren, S. Fan, and M. Lončar, "Electronically programmable photonic molecule," Nature Photonics **13**, 36–40 (2019).

[43] R. Bruck, B. Mills, B. Troia, D. J. Thomson, F. Y. Gardes, Y. Hu, G. Z. Mashanovich, V. M. Passaro, G. T. Reed, and O. L. Muskens, "Device-level characterization of the flow of light in integrated photonic circuits using ultrafast photomodulation spectroscopy," Nature Photonics **9**, 54 (2015).

[44] "Chapter 4," (this thesis).

[45] K. Vynck, N. J. Dinsdale, B. Chen, R. Bruck, A. Z. Khokhar, S. A. Reynolds, L. Crudgington, D. J. Thomson, G. T. Reed, P. Lalanne *et al.*, "Ultrafast perturbation maps as a quantitative tool for testing of multi-port photonic devices," Nature Communications **9**, 1–10 (2018).

[46] R. Bruck, K. Vynck, P. Lalanne, B. Mills, D. J. Thomson, G. Z. Mashanovich, G. T. Reed, and O. L. Muskens, "All-optical spatial light modulator for reconfigurable silicon photonic circuits," Optica **3**, 396–402 (2016).

[47] M. Notomi and H. Taniyama, "On-demand ultrahigh-Q cavity formation and photon pinning via dynamic waveguide tuning," Optics Express **16**, 18657–18666 (2008).

[48] T. Asano, B.-S. Song, Y. Akahane, and S. Noda, "Ultrahigh-Q nanocavities in two-dimensional photonic crystal slabs," IEEE Journal of Selected Topics in Quantum Electronics **12**, 1123–1134 (2006).

[49] R. M. de Ridder, C. Bostan, F. J. van Soest, and V. Gadgil, "Alignment issues in photonic crystal device fabrication," in "Proceedings of 2004 6th International Conference on Transparent Optical Networks (IEEE Cat. No. 04EX804)," , vol. 1 (IEEE, 2004), vol. 1, pp. 260–265.

[50] C. Moormann, J. Bolten, and H. Kurz, "Spatial phase-locked combination lithography for photonic crystal devices," Microelectronic Engineering **73**, 417–422 (2004).

[51] C. L. Panuski, I. Christen, M. Minkov, C. J. Brabec, S. Trajtenberg-Mills, A. D. Griffiths, J. J. McKendry, G. L. Leake, D. J. Coleman, C. Tran, J. St Louis, J. Mucci, C. Horvath, J. N. Westwood-Bachman, S. F. Preble, M. D. Dawson, M. J. Strain, M. L. Fanto, and D. R. Englund, "A full degree-of-freedom spatiotemporal light modulator," Nature Photonics **16**, 834–842 (2022).

[52] Y. A. Goldberg, *Gallium Indium Phosphide* $Ga_xIn_{1-x}P$ (World Scientific, 1999).

[53] S. Adachi, "Optical dispersion relations for GaP, GaAs, GaSb, InP, InAs, InSb, $Al_xGa_{1-x}As$, and In_{1-x} $Ga_xAs_yP_{1-y}$," Journal of Applied Physics **66**, 6030–6040 (1989).

[54] H. L. Anderson and American Institute of Physics, eds., *A Physicist's desk reference* (American Institute of Physics, New York, 1989).

[55] U. Piesbergen, "The mean atomic heats of the III-V semiconductors, AlSb, GaAs, InP, GaSb, InAs, InSb and the atomic heats of the element Germanium between 12 and 273 K," Zeitschrift für Naturforschung **18a**, 141–147 (1963).

[56] M. Levinshtein, S. Rumyantsev, and M. Shur, *Handbook Series on Semiconductor Parameters* (World Scientific, 1996).

[57] S. Sokolov, J. Lian, S. Combrié, A. D. Rossi, and A. P. Mosk, "Measurement of the linear thermo-optical coefficient of $Ga_{0.51}In_{0.49}P$ using photonic crystal nanocavities," Appl. Optics **56**, 3219–3222 (2017).

6

Conclusions

In conclusion, we have investigated the optical nonlinear behavior of photonic crystal nanoresonators with a specific interest in the optical multistability that arises when the resonators are coupled. Resonances corresponding to high-Q cavities have a thermo-optical nonlinear response to incoming light at low input power. This leads to optical bistability in single resonators, and multistability in coupled cavity configurations. This means that the system can stabilize in several optical states, with different corresponding intracavity energy, for the same input wavelength.

We give an introduction to photonic crystals in **Chapter 1** and treat the experimental apparatus in **Chapter 2**. We then continue with the research chapters. Firstly, we determine the thermo-optical response time of the system. Secondly, we measure the spatial mode profile of the addressed resonance, such that one can identify the modes of each cavity. Lastly, we demonstrate full control of the thermo-optical state over a multistable coupled resonator system.

Thermo-optical Timescale

In **Chapter 3** we measure the switching transient and determine the thermo-optical timescale of the bistable system for different resonances.

We perform input power scans and observe a thermo-optical hysteresis loop with a remarkable overshoot: a high intensity peak that then decays into a stable state. We further investigate the overshoot and take time-resolved measurements by step-modulating the input power, in this way recording the relaxation time of the overshoot. We do this for two different modes, a localized mode (the fundamental mode of the cavity) and a broad delocalized mode. We discover that the thermo-optical timescale is related to the size and shape of the mode profile, with a longer relaxation time for the larger mode.

We reproduce our results with our thermo-optical model. The model takes into account in-plane heat dissipation, and cooling via the gas layer between the membrane and the substrate. Due to the low thermal conductivity of InGaP, over 99.9% of the cooling happens through the gas layer. On the short timescale, in-plane diffusion is faster than diffusion via the air, this explains how the volume-to-surface ratio of a mode determines its thermo-optical relaxation time. We find excellent agreement between theory and experiment with a 90%-10% decay time of $\tau_{90-10} = 10.1 \pm 1.8\,\mu$s for the delocalized mode and $\tau_{90-10} = 7.7 \pm 2.2\,\mu$s for the fundamental cavity mode.

Notably, the decay time is not a fit parameter in the model. The theoretical decay time is determined by the experimentally measured mode profile that we feed into the model. This confirms that, indeed, it is the mode profile that determines the thermo-optical decay time of the resonance.

Mapping the Mode Profile

In **Chapter 4** we use the optical nonlinearity in the material to measure the spatial mode profile with enhanced resolution: a nonlinear mode mapping technique.

We do this with an out-of-plane visible light pump beam that scans the surface of the photonic crystal and probes the mode profile. For each pump position we measure the photonic crystal response for a range of near-infrared input wavelengths. The method is based on a photomodulation principle, where the optical pump modulates the local refractive index. Local heating by the pump beam redshifts the cavity resonance, therefore the imaging technique is limited by thermal diffusion, at least in the linear regime.

We observe a resolution enhancement in the nonlinear regime (high input power for the near-infrared probe light) and hypothesize that the enhancement is caused by free carrier absorption, hot carriers generated by the pump that have absorbed probe light. We formulate a thermo-optical model with all relevant thermo-optical sources in the photonic crystal, including free carrier absorption. The model the couples the optical resonance condition to the heat equation of the material.

To validate the model, we perform a line scan of a resonance with a known mode profile: the fundamental mode of the cavity. We repeat the line scan at increasing input power to demonstrate resolution enhancement in the nonlinear regime (at high input power rather than low input power). The experimental nonlinear mode map is beautifully matched with the theoretical mode map, confirming the adequacy of the model.

Secondly, we perform a line scan over a higher order mode of the cavity, both in the linear and nonlinear regime. The fringes associated with the higher order mode are only observed in the nonlinear regime, confirming the resolution enhancement for the nonlinear mode mapping technique. We achieve a very nice reproduction of the experimental results with the thermo-optical model, and proof that to resolve the separate peaks of the higher order mode, the only thing needed is increased input light.

Our thermo-optical model explains that the carrier plasma generated by the pump has a spot size comparable to the optical spot of the pump beam due to the short lifetime of the carriers. The resolution is therefore determined by the optical pump profile rather than the much broader thermal pump profile, which means we go beyond the thermal resolution limit. With this enhanced resolution we are able to measure the fringes of the higher order mode profile that is not observable in the low probe power (linear) regime.

This makes for a non-invasive, far-field imaging method. Moreover, the resolution enhancement happens at surprisingly low carrier density, thus the pumping

requirements are convenient at constant wave non-damaging power.

Walking Through the Multistable Phase Space

In **Chapter 5** we focus on coupled cavities in the nonlinear regime. We have three mode-gap cavities situated on the waveguide that form a system of coupled nanoresonators. We probe them in the nonlinear regime, and map the multistability of the system by doing a spatial excitation scan over the waveguide for a range of input wavelengths.

Excitation happens through a local pump pulse with the out-of-plane visible light beam. We measure the photonic crystal response before, during and right after the pump pulse. We reset the system by dipping the input power to zero after each pump procedure. This is repeated for a grid of pump positions and input wavelengths, constructing the excitation response map over the length of the waveguide. We observe the mode profiles of the three mode-gap cavities, confirm that they are coupled with the observation of an avoided crossing of the resonances, and conform that they are in the nonlinear regime since their lineshape is asymmetrical. Most strikingly, we observe a thermo-optical state change that remains after the pump has turned off.

With the excitation response map we find multiple stable states at the same wavelength and determine the precise excitation spot needed to walk through the phase space of the coupled modes, with each step lowering or raising the intracavity energy. We demonstrate this by a programmed all-optical multistable switching experiment, jumping between stable thermo-optical states with a microsecond pump pulse in a specific pump position, bringing the coupled resonator system into the state with the expected associated output intensity.

We explain the observations by expanding on the thermo-optical model of Chapter 4 with coupled mode theory. We use it to reproduce the excitation response map, with very good correspondence between experiment and model. We look at the thermal distribution associated with specific stable states. We discover that each optical state branch corresponds to a certain thermal profile. More concretely, the excitation response map shows areas of thermo-optical configurations of two hybridized cavities, tying together bright and dim resonances to three different warm ‘on’ states and one cold ‘off’ state, where high output intensity corresponds to high temperature.

Outlook

In future research it is interesting to look at modulated excitation in combination with lock-in amplified detection. Additionally, decreasing the pump spot size increases the mode map resolution. This, possibly in combination with a shorter

wavelength pump source, has the prospect of resolving standing waves nodes inside the photonic crystal. Coupling more cavities is a logical next step, as it further increases the phase space, and will bring slow light applications within reach. Another idea expanding on this research can include the long standing goal of transient cavities, these are proposed cavities that are formed on-demand at desired position by shooting with a pump beam at an empty waveguide.

7

Samenvatting

Nanofotonica en Fotonische Geïntegreerde Schakelingen

In de nanofotonica zijn we geïnteresseerd in het gedrag van licht op nanometerschaal. We proberen dit gedrag te begrijpen en te manipuleren zodat we het kunnen inzetten voor verschillende doeleindes. Fotonische kristallen zijn hier een voorbeeld van. Het zijn materialen die ontworpen zijn om lichtbundels te kunnen richten, reflecteren, opsluiten, versterken en vertragen. Zo zijn er golfgeleiders, structuren die de inkomende elektromagnetische golf insluiten en over een baan laat voortbewegen, en bestaan er resonatoren, trilholtes die grote vermogens aan licht lokaliseren op een klein volume van het medium: ideaal voor het bestuderen van de interactie tussen licht en materie.

Membranen van halfgeleider materiaal worden gebruikt voor het fabriceren van tweedimensionale fotonische kristallen. Deze kunnen worden gebruikt in optische chips, *photonic integrated circuits* of *pic's*, de optische tegenhanger van de elektronische geïntegreerde schakeling die je in elke computer of telefoon vindt. Dit soort geïntegreerde fotonica heeft in eerste instantie toepassing in de optische netwerken van de telecomindustrie, evenals in datacentra en optische (kwantum)computatie. In de telecomindustrie gebeurt lange-afstand data transfer altijd optisch via het glasvezel netwerk, terwijl de digitale signaalverwerking nog met de beproefde elektronische componenten gebeurt. De conversie van optisch naar elektrisch en weer terug is inefficiënt, het kost tijd en energie. Het zoveel mogelijk overstappen naar optische elementen is daarom interessant. Temeer omdat het wereldwijde dataverkeer in 2018 al 3% van het totale elektriciteitsverbruik besloeg, en dit zonder efficiëntie verbeteringen naar verwachting exponentieel toeneemt tot 31% van het mondiale elektriciteitsverbruik in 2030[1].

In de kwantumcomputatie worden fotonische kristallen bijvoorbeeld gebruikt om on-chip trilholtes te fabriceren die als enkel-foton lichtbron kunnen fungeren. Maar de mogelijkheden voor deze materialen op het gebied van (bio)sensoren, medische apparatuur, beeldvormingstechnieken, lidar (laser radar), zonnecellen, optische neurale netwerken en fundamenteel onderzoek zijn nog lang niet uitgeput. Dit actieve veld vindt een bruisende fotonicasector in Nederland met interactie tussen universiteiten en de industrie.

Fotonische kristallen

De grip die fotonische kristallen bieden op de voortplanting van lichtgolven is gebaseerd op het principe van de fotonische bandkloof. Dit is een gebied van verboden lichtfrequenties. Voor licht van de bijbehorende golflengte is het ma-

[1]Economic and Financial Analysis Division van ING Bank N.V. (2019), Further efficiency gains vital to limit electricity use of data; IEA (2022), Data Centres and Data Transmission Networks

teriaal een perfecte spiegel, dit licht kan niet bestaan bestaan in de bandkloof. Dit wordt bereikt door het materiaal een periodieke brekingsindex[2] te geven. De roosterconstante, de afstand waarmee het brekingsindex patroon zich herhaalt, heeft de ordegrootte van de golflengte van het licht heeft. Voorbeelden hiervan bestaan in de vorm van een-, twee-, en drie-dimensionale fotonische kristallen.

Fotonische kristallen zijn (vanwege die capaciteit tot het opsluiten van licht) bijzonder geschikt voor het fabriceren van trilholtes met een hoge kwaliteitsfactor. Deze trilholtes kunnen gemakkelijk een hoge interne energie bereiken. Daarom is er vaak – afhankelijk van het materiaal – sprake van niet-lineaire optica. In dat geval heeft het materiaal een niet-lineaire reactie op de veldsterkte van het licht: de ingaande lichtintensiteit is niet lineair gerelateerd aan de uitgaande lichtintensiteit. Dit verschijnsel faciliteert actieve optische elementen, bijvoorbeeld on-chip lasers of optische transistors. In **Hoofdstuk 1** gaan we in op de natuurkundige fundamenten van fotonische kristallen, de niet-lineaire optica in het materiaal, en de toepassingen.

De niet-lineariteit in het materiaal kan leiden tot optische bistabiliteit in de trilholte. Hierbij zijn er twee stabiele toestanden mogelijk bij een enkele golflengte. Deze twee toestanden worden gebruikt voor optische schakelaars, een wissel tussen een output signaal van 0 (lage lichtintensiteit) en 1 (hoge lichtintensiteit). Door een reeks niet-lineaire resonatoren te koppelen wordt de faseruimte vergroot en kan er optische multistabiliteit worden bereikt.

In dit proefschrift onderzoeken wij een fotonisch kristal membraan met een reeks van drie resonatoren op een golfgeleider (zie Figuur 7.1). Het bestaat uit een hexagonaal kristalrooster van luchtkolommen in een dun membraan van indiumgalliumfosfide ($Ga_{0.51}In_{0.49}P$) geschikt voor infrarood licht rond 1550 nm. In **Hoofdstuk 2** bespreken we de experimentele opstelling waar we ons fotonisch kristal mee manipuleren en doormeten.

De reactietijd van het systeem

Eerder noemden we dat trilholtes met hoge kwaliteitsfactor tot niet-lineaire optica kunnen leiden. Ons fotonisch kristal is gemaakt van indiumgalliumfosfide, een materiaal dat inderdaad niet-linear reageert op hoge intensiteit inkomend licht. In een enkele trilholte leidt dit tot bistabiliteit: het systeem kan stabiliseren in twee verschillende toestanden, waarbij de ene toestand heel fel- en de andere heel zwak oplicht.

De niet-lineariteit van de nanoresonators is van thermo-optische aard. Dit betekent dat de temperatuur van het materiaal diens optische eigenschappen beïnvloedt, en tegelijkertijd dat de veldsterkte van het licht de temperatuur

[2]De brekingsindex van een materiaal geeft de verhouding van de snelheid van het licht in vacuüm ten opzicht van de snelheid van het licht in dat medium.

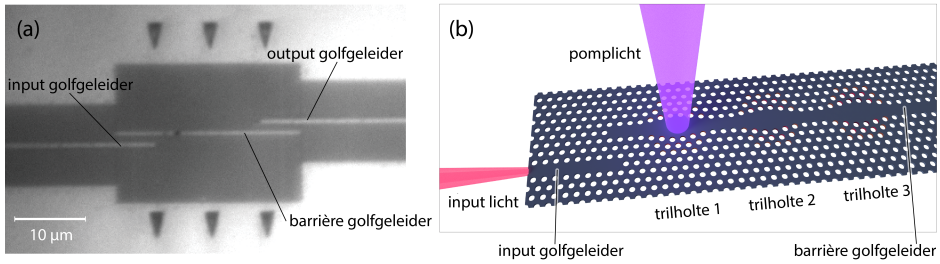

Figure 7.1: (a) Foto van het fotonisch kristal met input- en output golfgeleider en drie resonatoren op de barrière golfgeleider (de trilholtes zijn niet zichtbaar met het blote oog). (b) Schematische weergave van het fotonisch kristal ontwerp. Het bestaat uit een 180 nm dun membraan van indiumgalliumfosfide met daarin een hexagonaal patroon van luchtkolommen. De golfgeleider wordt gevormd door een rij aan luchtkolommen te verwijderen. De trilholtes worden gevormd door lokaal de golfgeleider te verbreden door de positie van de luchtkolommen iets te verschuiven van hun standaard positie. Het fotonisch kristal wordt doorgemeten aan de hand van infrarood input licht rondom 1550 nm, ingekoppeld via de input golfgeleider. Ruimtelijk wordt het fotonisch kristal gemanipuleerd met een optische excitatie bron, een blauwe pompbundel waarvan het focus overal op het oppervlak van het membraan kan worden geplaatst.

beïnvloedt. Deze interactie is precies het fundament van de niet-lineariteit. Van de thermo-optische bistabiliteit die hieruit volgt is het belangrijk te weten hoe snel het systeem kan schakelen tussen de twee thermo-optische toestanden.

In **Hoofdstuk 3** meten we de thermo-optische tijdschaal in ons fotonisch kristal. Hiervoor laten we het systeem verspringen van lage naar hoge energetische toestand door middel van stap-modulatie van het vermogen van het input licht (van laag vermogen naar hoog vermogen in één stap). De stap-modulatie brengt het thermo-optische systeem uit balans. We observeren op het moment van de sprong een piek in het signaal dat vervolgens uitdooft en opnieuw thermo-optisch evenwicht bereikt in de hoge energetische toestand (zie Figuur 7.2).

We doen dit voor verschillende optische modi. Een optische mode is een resonantie van één of een aantal gekoppelde trilholtes op een bepaalde golflengte met een bepaalde interne energie en bijbehorend ruimtelijk modeprofiel. Het modeprofiel beschrijft de veldsterkte van de mode in de ruimte, met andere woorden, de ruimtelijke vorm van de optische resonantie (waar in het materiaal het licht resoneert). We ontdekken hierbij dat het modeprofiel bepalend is voor de relaxatietijd. De mode met het modeprofiel dat bijna de volledige lengte van de golfgeleider beslaat heeft een langere relaxatietijd dan de gelokaliseerde, compacte mode van de trilholte.

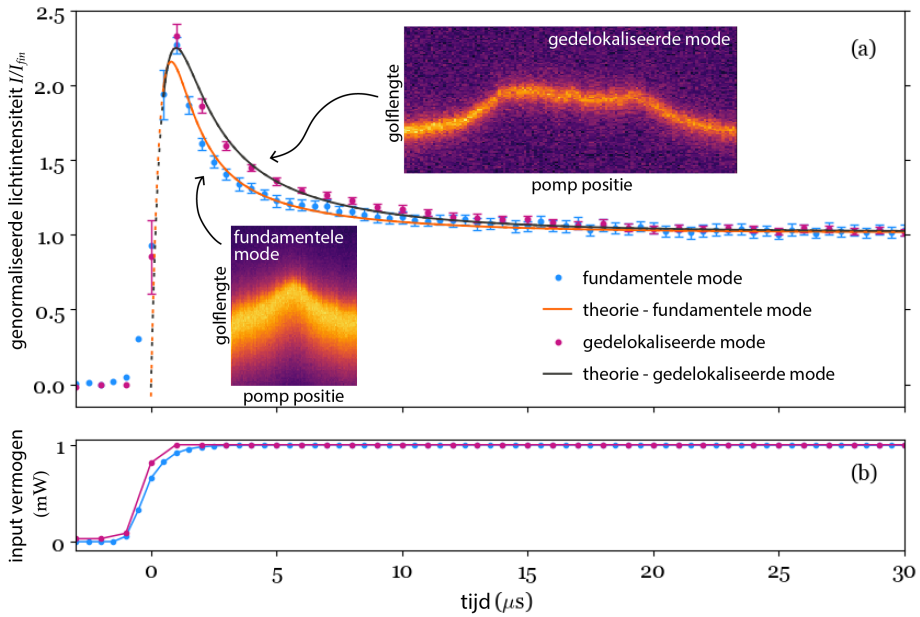

Figure 7.2: Thermo-optische relaxatie van de fundamentele mode van de middelste trilholte en een gedelokaliseerde mode in het fotonisch kristal. Het gemeten modeprofiel van elke mode is afgebeeld in de bijzet panelen. (a) De optische respons van de mode als functie van de tijd, naar aanleiding van de stap-modulatie van het input vermogen. (b) Het input vermogen als functie van diezelfde tijdsas.

We verklaren dit aan de hand van de oppervlakte-volume ratio van de mode. De compacte mode (dit is de fundamentele mode[3] van de trilholte) heeft een groter oppervlak ten opzichte van volume dan de uiteengespreide mode. Overal waar het modeprofiel aanwezig is warmt het elektromagnetische veld het materiaal op. Dit omdat een klein deel van het licht geabsorbeerd wordt door het indiumgalliumfosfide. Het membraan moet die warme ook weer kwijt. Het koelen gebeurt op korte tijdschaal binnen het vlak van het membraan: dissipatie vindt plaats door de oppervlakte strook die de mode omringt en zorgt zo voor het 'uitdijen' van het thermische profiel. Op iets langere tijdschaal koelt het thermische profiel vervolgens af via het oppervlak van het membraan, dat wil zeggen, via de dunne luchtlaag die tussen het membraan en het substraat daaronder ligt. Omdat het thermisch profiel van de compacte mode relatief sneller uitdijt en

[3]De fundamentele mode is de resonantie in een trilholte met de langst mogelijke golflengte.

daarna zijn warmte over een relatief groter oppervlak kan laten afkoelen heeft het een kortere relaxatietijd. Zo vinden we een uitdooftijd van 7.7 μs voor de fundamentele mode en 10.1 μs voor de uiteengespreide mode. De resultaten worden ondersteund met een theoretische model dat bevestigd dat de relaxatietijd inderdaad wordt bepaald door het modeprofiel.

Het ruimtelijke modeprofiel van de resonantie

Het spectrum[4] van het fotonisch kristal zit vol verschillende resonantie pieken. Daarom is het belangrijk om resonanties te kunnen identificeren aan de hand van het modeprofiel (zoals ook wordt gedaan in Hoofdstuk 3), bijvoorbeeld zodat je de fundamentele mode van een resonator kunt vinden en bestuderen. In **Hoofdstuk 4** demonstreren we een niet-lineaire verre-veld methode om het modeprofiel af te beelden. We doen dit met behulp van een externe, blauwe lichtbundel (405 nm pomplicht), dat loodrecht op het kristalmembraan staat en ruimtelijke scans maakt over het oppervlak. Met deze methode hebben we een non-invasieve, handzame afbeeldingstechniek tot onze beschikking omdat het wordt uitgevoerd bij lage vermogens van de pompbundel die niet schadelijk zijn voor het fotonisch kristal. Er is daarom geen noodzaak tot beperking van blootstelling aan de lichtbundel met behulp van femtoseconde pulsen.

Het belangrijkste resultaat is een verbeterde resolutie ten opzichte van lineaire verre-veld afbeeldingstechnieken én de natuurkundige verklaring hiervoor. In het lineaire regime (dat wil zeggen, bij laag vermogen input licht) wordt de resolutie bepaald door de afmeting van het thermische profiel van de pompbundel, immers, de techniek berust op het thermo-optische roodverschuiven van de resonanties door lokale verwarming met het pomplicht.

Het pomplicht werkt als lokale warmtebron omdat het wordt geabsorbeerd door het indiumgalliumfosfide. Daarbij wordt met de energie van het geabsorbeerde foton een elektron aangeslagen van valentieband naar conductieband. Hierna laat het aangeslagen elektron de energie weer vrij in de vorm van fononen, trillingen in het kristalrooster van het indiumgalliumfosfide. Op deze manier verspreid zich warmte door het materiaal, en wordt de breedte van het thermische profiel bepaald.

Echter, wanneer het aangeslagen elektron zich bevind in een sterk elektromagnetisch veld kan het nog een foton absorberen, dit keer een infrarood foton van het input licht. Dit creëert een plasma van 'hete' ladingsdragers dat een lokale warmtebron met hogere temperatuur verschaft. Omdat de elektronen niet lang leven zullen ze nog steeds in de buurt zijn van de plek waar ze werden aangeslagen

[4]Met het spectrum van het fotonisch kristal bedoelen we hier de uitslag of amplitude van het fotonisch kristal als resonator in reactie op de inkomende elektromagnetische golf als functie van de frequentie (of golflengte) van die golf.

op het moment dat ze opnieuw een infrarood foton absorberen. Daarom heeft deze warmtebron een afmeting die vergelijkbaar is met het *optische* profiel van de pompbundel. Dit optische profiel is bijna tien keer kleiner dan het thermische profiel van het pomplicht (0.5 micrometer versus 4 micrometer). Dit verklaart hoe de verbeterde resolutie voorbij de thermische limiet gaat.

We demonstreren de verbeterde resolutie aan de hand van een optische mode die twee dicht op elkaar gelegen pieken heeft in het modeprofiel. De fundamentele mode van een resonator zal een modeprofiel hebben met één centrale piek. De eerste hogere orde mode heeft twee pieken. Om de modi te kunnen onderscheiden heb je voldoende resolutie nodig. We laten zien dat die nauwkeurigheid te bereiken is door enkel en alleen het vermogen van het infrarood input licht te verhogen. Het hoge vermogen input licht brengt het systeem in het optisch niet-lineaire regime.

In het niet-lineaire regime gebeuren er twee dingen, ten eerste is er voldoende vermogen infrarood licht om een plasma hete ladingsdragers te genereren. Vergeet daarbij niet dat de veldsterkte is gegeven door het modeprofiel, en het plasma dus overlapt met het modeprofiel. Ten tweede zorgt de optische niet-lineariteit voor een zeer gevoelige balans in het fotonisch kristal. Om dit te begrijpen is het belangrijk te weten dat er naast de warmtebron van blauw pomplicht absorptie door het indiumgalliumfosfide, en de warmtebron van infrarood foton absorptie door vrije ladingsdragers, er een derde warmtebron aan te wijzen is: absorptie van een deel van het infrarood licht door het indiumgalliumfosfide. Je kunt het fotonisch kristal dus opwarmen door op, of in de buurt van, een intense resonantie infrarood licht in te sturen. Deze input licht absorptie veroorzaakt de bistabiliteit die we eerder noemden.

Eén van beide toestanden in het bistabiele gebied is de meeste intense, 'warme' toestand. Hierbij is het kristal opgewarmd door wat er in de geschiedenis van het fotonisch kristal gebeurd is (bijvoorbeeld omdat het input licht geleidelijk aan richting de resonantie toe verstemd is). De warmte zorgt ervoor dat de resonantie roodverschoven is, de resonantie is dus een bepaalde afstand verstemd van de 'koude' resonantie. De verstemde toestand wordt in stand gehouden door het input licht zelf, omdat het warmte genereert. Deze thermo-optische balans is zeer gevoelig, en is gerelateerd aan het modeprofiel, i.e., de ruimtelijke veldsterkte.

De verbeterde resolutie is dus te verklaren vanuit de extra warmte van hete plasma en de gevoelige thermo-optische balans van de verstemde resonanties. Beide effecten zijn evenredig met het modeprofiel, en verbeteren dus de gevoeligheid waarmee dit modeprofiel gemeten kan worden.

Experimenteel laten we dit zien door het modeprofiel van de eerste hogere orde mode te meten, zie Figuur 7.3(a). Eerst meten we in het lineaire regime, waar we een enkele, uitgesmeerde, brede piek observeren in het modeprofiel. Vervolgens meten we diezelfde mode in het niet-lineaire regime, waar we de twee

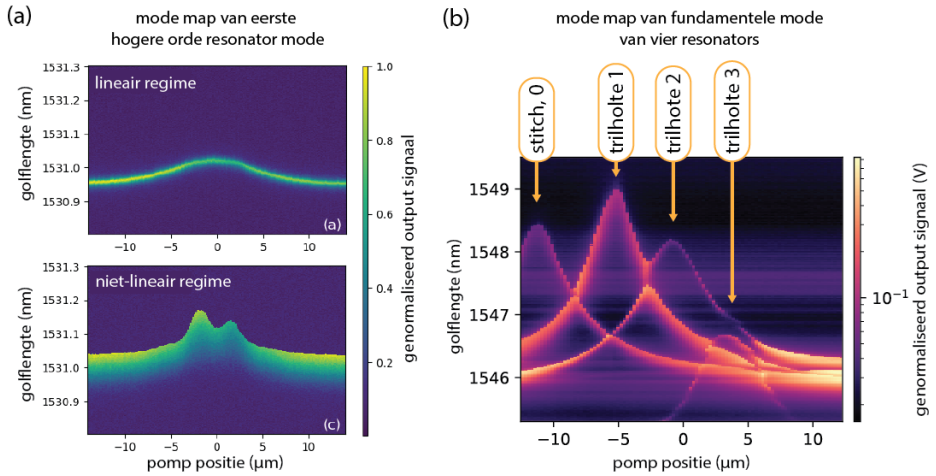

Figure 7.3: (a) Mode map van eerste hogere orde mode van de resonator in het lineare (bovenste paneel) en niet-lineaire regime (onderste paneel). Er is een duidelijke toename in resolutie waar te nemen, met in de niet-lineaire meting de twee onderscheidbare pieken die karakteristiek zijn voor de eerste hogere orde mode. (b) Mode map van de fundamentele mode van de drie trilholtes op de golfgeleider en één resonantie die een artefact is van het fabricatie proces. De laatste wordt 'stitch mode' genoemd omdat deze ontstaat op de naad van de stralingsvelden waarmee het ontwerp op het indiumgalliumfosfide wordt overgebracht.

onderscheidbare pieken observeren. Met ons theoretische model, dat alle drie de warmtebronnen in de berekening meeneemt, reproduceren we de experimentele resultaten en ondersteunen onze natuurkundige verklaring voor de observatie.

Exploratie van de faseruimte in multistabiel systeem

Tot nu toe hebben we gekeken naar niet-lineair gedrag in enkele resonatoren. In **Hoofdstuk 5** bestuderen we configuraties van twee *gekoppelde* niet-lineaire nanoresonatoren. De kennis over de thermo-optische tijdschaal, het spectrum, en het ruimtelijke modeprofiel gebruiken we nu om de faseruimte van de niet-lineaire gekoppelde resonatoren te onderzoeken.

De faseruimte weergeeft alle mogelijke toestanden die ons thermo-optische systeem van gekoppelde resonatoren kan hebben. Omdat we nu twee bistabiele resonators koppelen waaiert de faseruimte uit naar een multistabiel systeem. In dit experiment bewegen we in stappen door de multistabiele faseruimte heen.

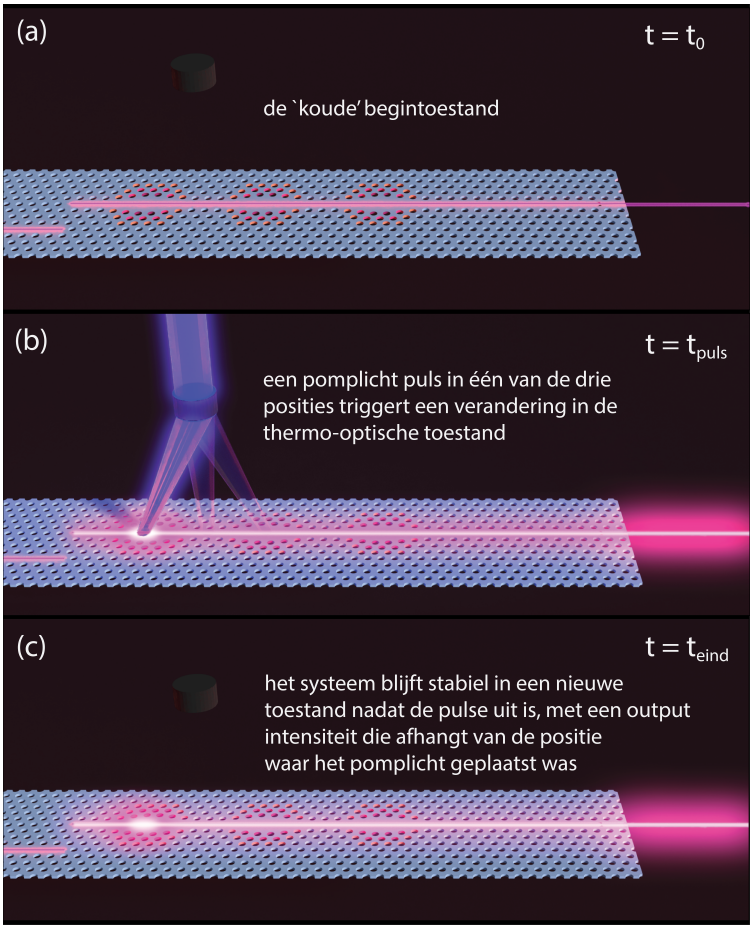

Figure 7.4: Optische multistabiliteit in gekoppelde, niet-lineaire resonators. (a) We sturen infrarood licht door het vlak van het fotonisch kirstal membraan over de golfgeleider (b) Met een blauwe lichtpomp, loodrecht op het membraan, geven we een korte puls op een specifieke plek. Dit triggert een toestandsverandering in het thermo-optische systeem. (c) Nadat de pomp weer uit is, is de thermo-optische configuratie van de gekoppelde resonators veranderd. Deze nieuwe toestand is stabiel. De interne energie in de gekoppelde trilholtes (en dus ook output) die gepaard gaat met deze nieuwe toestand wordt bepaald door de plek waar de pomp puls was geplaatst.

We springen van de ene stabiele toestand naar de andere met behulp van de pompbundel, waarmee we op specifieke plaatsen op het kristaloppervlak een korte lichtpuls geven om de gewenste toestand aan te slaan. Zie Figuur 7.4 voor een illustratieve weergave. Hiermee demonstreren we een programmeerbare, volledig optische, multistabiele schakelaar; waarbij we verschillende stabiele toestanden aandoen door de interne energie van de twee gekoppelde resonators te verlagen of te verhogen in thermo-optische configuraties van warme en koude trilholtes.

De toestand van het systeem hangt af van de input golflengte en de thermo-optische geschiedenis. Dat wil zeggen, de thermo-optische geschiedenis bepaalt de huidige temperatuurverdeling in het membraan, en daarmee de optische eigenschappen. Elke stabiele toestand is daarmee een balans tussen de optische mode met corresponderend modeprofiel en de warmteverdeling die daarbij hoort. Via die weg is het mogelijk stabiele toestanden te vinden die bijzonder fel zijn en zichzelf in stand houden via zelf-verwarming (zoals uitgelegd in de vorige sectie).

Om de faseruimte in beeld te brengen meten we een zogenaamde *excitatie respons map*, dat wil zeggen een kaart die weergeeft hoe het systeem reageert op positieafhankelijke excitatie (een pomp puls). We brengen hiervoor het systeem eerste in een koude toestand, om de thermo-optische geschiedenis te resetten, simpelweg door het input licht kort uit en weer aan te zetten. Daarna warmen we het systeem lokaal op met een pomplicht puls. Na de puls blijven we het systeem monitoren om te meten welke thermo-optische toestanden op deze manier te bereiken zijn.

De response map heeft twee assen: de golflengte van het infrarode input licht, en de pomp positie. De faseruimte is dus opgetrokken uit deze twee dimensies, en tegelijkertijd afhankelijk van de thermo-optische geschiedenis. Daarom heeft de respons map drie 'scenes': vóór de pomp puls, tijdens de pomp puls en gelijk na de pomp puls. We monitoren de respons van het fotonisch kristal via het lek-licht dat ontsnapt uit het membraan. Het fotonisch kristal sluit het licht nooit perfect op, daarom kunnen we dit lek-licht gebruiken om de toestand in het kristal te meten. We meten de respons van het fotonisch kristal voor een reeks van input golflengtes en pomp posities en brengen zo elke scene in kaart.

De response map *tijdens* de pomp puls vertelt ons waar de fundamentele modes van de resonators te vinden zijn (op welke golflengte en hun ruimtelijke positie) en hoe ze gekoppeld zijn aan elkaar, zie Figuur 7.3(b). Voor twee gekoppelde resonators kan er *hybridizatie* bestaan. De twee resonatoren zijn dan optisch aan elkaar verbonden en de spectrale resonantie lijnen zijn niet meer toe te schrijven aan de ene of andere trilholte op het moment van hybridizatie. Dit is te herkennen in het spectrum aan de hand van de *avoided crossing*, een fenomeen waarbij de spectrale lijnen van twee gekoppelde resonators elkaar nooit zullen doorkruizen. De grootte van de kloof tussen de resonanties op die *avoided crossing* is een maat voor de koppelsterkte tussen die twee resonanties.

Aan de experimenteel gemeten respons map tijdens de puls zien we dat de eerste twee trilholtes sterk gekoppeld zijn. En voor bepaalde thermo-optische condities vormen ze een gehybridiseerde resonantie. Alle hoog-energetische thermo-optische toestanden die we aanslaan in dit experiment zijn configuraties van deze twee gehybridiseerde resonators. Hier blijkt dat we de volgende intuïtieve vuistregel kunnen aanhouden: een optische felle mode is tevens een warme mode.

De response map vlak na de puls vertelt ons welke toestanden er te bereiken zijn door middel van positie-afhankelijke excitatie. We gebruiken deze informatie om drie pomp posities te kiezen in een pomp puls reeks, en daarmee te 'wandelen' door drie verschillende thermo-optische toestanden van de twee gekoppelde trilholtes. Dit is onze optische, programmeerbare, schakelaar. We ondersteunen het resultaat met een theoretisch model en reproduceren de excitatie respons maps. Omdat er geen experimentele methode is om de warmteverdeling in het membraan te meten gebruiken we hiervoor de theorie. We simuleren de thermische profielen die corresponderen met de diverse toestanden die we voorbij zien komen in de optische schakelaar.

In het resultaat zien we combinaties van twee warme of koude trilholtes, waarbij elke karakteristieke optische output (heel fel, gemiddeld fel, donker) een karakteristiek thermisch profiel heeft (twee heel hete trilholtes met het thermisch gewicht op links, twee gemiddeld hete trilholtes met het thermische gewicht op rechts of symmetrisch verdeeld, twee koude trilholtes). Dit bevestigt het beeld van twee gekoppelde resonators die samen in verschillende thermo-optische configuraties zitten.

Vooruitblik

Voor toekomstig onderzoek is het interessant om meer dan twee resonatoren te koppelen, en mogelijk zelfs 10 of 100 resonatoren te koppelen om toepassingen van traag licht te exploreren. Ook bestaat het idee om, waar en wanneer je wil, instantaan trilholtes in het leven te roepen door te 'schieten' met pomplicht op een lege golfgeleider. Tot slot zou de resolutie van de niet-lineaire afbeeldingstechniek van het modeprofiel verder verbeterd kunnen worden door het focus van de externe lichtbundel kleiner te maken. Mogelijk is het haalbaar om de buiken en knopen van staande lichtgolven af te beelden met een hoog-NA microscoop objectief en/of korte golflengte lichtbron. Een andere optie is het moduleren van de pomplichtbron in combinatie met hoge bandbreedte detectie voor hogere concentraties ladingdragers met kleinere ruimtelijke distributie.

8

Dankwoord

Als je het mij vraagt is de *Nanophotonics* groep van het Debye Instituut heel bijzonder. Bij deze mensen, op deze plek, heb ik mij meer dan zes jaar thuis gevoeld. Eerst een jaar als masterstudent, en na een tussenjaar (met een kantoorbaan als data scientist waar ik geheel níet op mijn plek was) nog ruim 5 jaar als PhD kandidaat. Terugkomen om onderzoek te doen is één van de beste beslissingen in mijn leven geweest.

Met heel veel plezier heb ik in het lab gestaan. Ik hou van dit werk. Het puzzelen, het bouwen, het priegelige uitlijnen, het 'temmen van het beest'. De creativiteit en de analytische aanpak die nodig is bij experimenteel onderzoek. Deze periode, met al de vrijheid en uitdagingen, heb ik als een unieke, mooie tijd ervaren. Het is een prachtige baan.

Maar de baan is niet de ziel van de plek. Het zijn de mensen. Hoe ze denken. Hoe ze elkaar benaderen. Hoe ze met elkaar grappen. Een buitenstaander zal waarschijnlijk vooral een stelletje NERDS zien. Well, they're not wrong. Maar ik kan je vertellen dat deze mensen behalve intelligent, en af en toe sociaal onhandig, vooral zachtaardig en goed bedoelend zijn. In deze groep heb ik weinig competitief gedrag of ellebogenwerk ervaren. Dat is bijzonder binnen de topsport van de academische wereld.

Ik heb hier fijne mensen leren kennen. Sommigen zijn inmiddels vrienden. Anderen warme collega's. Weer anderen de niet onbelangrijke, af en toe curieuze, entourage. Als je niet oplet kan de waarde van de mensen om je heen aan je aandacht ontglippen. Vooral de introverte mens, die graag onafhankelijk is, die zich teruggetrokken prettig voelt, vergeet soms hoe zeer je die ander nodig hebt. Tijdens de covid lockdowns werd ik hieraan herinnerd. Dat deze groep, jullie allemaal, mij heel dierbaar zijn. Dankjulliewel.

9

Resume

My resume will show you that I am a person with more than one vocation. Both music and the exact sciences have inspired me and brought me joy and fulfillment. Working towards research results or a musical album have many parallels. In both worlds I never get bored. Because we imagine, find a path, build, take a step back to assess, and try again. May it be with a song in the studio, or an experiment in the lab.

MASTER OF SCIENCE, EXPERIMENTAL PHYSICS
Utrecht University | Sept 2013 - May 2016

Master thesis: at the Nanophotonics group of the Debye Institute under supervision of dr. D. van Oosten. Achieving photon Bose-Einstein condensation in a dye-filled microcavity.

BACHELOR OF SCIENCE, PHYSICS AND ASTRONOMY
Utrecht University | Sept 2010 - Aug 2013

Bachelor thesis: at the Institute for Subatomic Physics under supervision of Dr. Marco van Leeuwen. Simulation and analysis of deformed peaks in data histograms yielded from the ALICE detector of CERNs LHC.

MASTER OF ARTS, COMPOSITION IN CONTEXT
HKU University of the Arts Utrecht | 2008 - 2009

BACHELOR OF MUSIC, COMPOSITION FOR MEDIA
HKU University of the Arts Utrecht | 2005 - 2009

ATHENEUM (VWO)
A. Roland Holst College | 1999 - 2005

10

Publication List

Mode mapping $Q > 5 \times 10^5$ photonic crystal nanocavities using free carrier absorption., K. Perrier, J. Baas, S. Greveling, G. Lehoucq, S. Combrié, A. de Rossi, S. Faez, A.P. Mosk. **Phys. Rev. Appl. 18 (3)**, 034044 (2022)

Thermo-optical dynamics of a nonlinear GaInP photonic crystal nanocavity depend on the optical mode profile. K. Perrier, S. Greveling, H. Wouters, S.R.K. Rodriguez, G. Lehoucq, S. Combrié, A. de Rossi, S. Faez, A.P. Mosk. **OSA Continuum 3 (7)**, 1879–1890 (2020)

Density distribution of a Bose-Einstein condensate of photons in a dye-filled microcavity. S. Greveling, K.L. Perrier, D. van Oosten. **Phys. Rev. A 98 (1)**, 013810 (2018)

The effective interaction strength in a Bose-Einstein condensate of photons in a dye-filled microcavity. S. Greveling, F. van der Laan, K.L. Perrier, D. van Oosten **arXiv preprint** (2017)

Acronyms

1D one-dimensional.

2D two-dimensional.

3D three-dimensional.

BOA power booster.

CCD charge-coupled device.

CCP-RIE capacitively coupled plasma reactive ion etching.

CIR circulator.

cw continuous wave.

DAQ data acquisition system.

EO electro-optical.

EOM electro-optical modulator.

FCA free carrier absorption.

FDTD finite-difference time-domain.

FSM free steering mirror.

FWHM full width at half maximum.

FWM four-wave mixing.

GaAs gallium arsenide.

HO mode higher-order mode.

InGaP indium gallium phosphide; $Ga_{0.51}In_{0.41}P$.

IR infrared.

MIBK sobutyl-ketone solution.

N_2 nitrogen.

NA numerical aperture.

ND neutral-density (filter).

NIR near infrared.

NPMS nonlinear photomodulation spectroscopy.

NSOM near-field scanning optical microscopy.

OPO optical parametric oscillator.

PC personal computer.

PD photodiode.

PhC photonic crystal.

PhCR photonic crystal resonator.

PM photonic molecule.

PMMA polymethyl-methacrylate.

PMS photomodulation spectroscopy.

Q-factor quality factor.

Si silicon.

SiN silicon nitride.

SiO_2 silicon dioxide / silica.

SLM spatial light modulator.

TE transverse electric (polarized light).

TM transverse magnetic (polarized light).

TO thermo-optical.

TTL transistor-transistor logic (trigger).

UV ultraviolet.

VIS visible (light).

WDM wavelength-division multiplexing.